University of Wollongong

Research Online

University of Wollongong Thesis Collection 2017+

University of Wollongong Thesis Collections

2021

Magnetorheological Variable Stiffness Robot Legs for Improved Locomotion Performance

Matthew Daniel Christie
University of Wollongong

Follow this and additional works at: https://ro.uow.edu.au/theses1

University of Wollongong

Copyright Warning

You may print or download ONE copy of this document for the purpose of your own research or study. The University does not authorise you to copy, communicate or otherwise make available electronically to any other person any copyright material contained on this site.

You are reminded of the following: This work is copyright. Apart from any use permitted under the Copyright Act 1968, no part of this work may be reproduced by any process, nor may any other exclusive right be exercised, without the permission of the author. Copyright owners are entitled to take legal action against persons who infringe their copyright. A reproduction of material that is protected by copyright may be a copyright infringement. A court may impose penalties and award damages in relation to offences and infringements relating to copyright material. Higher penalties may apply, and higher damages may be awarded, for offences and infringements involving the conversion of material into digital or electronic form.

Unless otherwise indicated, the views expressed in this thesis are those of the author and do not necessarily represent the views of the University of Wollongong.

Recommended Citation

Christie, Matthew Daniel, Magnetorheological Variable Stiffness Robot Legs for Improved Locomotion Performance, Doctor of Philosophy thesis, School of Mechanical, Materials, Mechatronic and Biomedical Engineering, University of Wollongong, 2021. https://ro.uow.edu.au/theses1/1090

Research Online is the open access institutional repository for the University of Wollongong. For further information contact the UOW Library: research-pubs@uow.edu.au

School of Mechanical, Materials, Mechatronic and Biomedical Engineering

Faculty of Engineering and Information Sciences

University of Wollongong

Magnetorheological Variable Stiffness Robot Legs for Improved Locomotion Performance

Matthew Daniel Christie

This thesis is presented as part of the requirements for the award of

Doctor of Philosophy in Engineering

June 2021

DECLARATION

I, Matthew Daniel Christie, declare that this thesis, submitted in partial fulfilment of the requirements for the award of Doctor of Philosophy, of the School of Mechanical, Materials, Mechatronic and Biomedical Engineering, Faculty of Engineering and Information Sciences, University of Wollongong, is wholly my own work unless otherwise referenced or acknowledged. Given this thesis is primarily formed though publication, I am the first author of any such publications which form major chapters in this thesis. The document has not been submitted for qualifications at any other academic institution.

Matthew Daniel Christie

June, 2021

ABSTRACT

In an increasingly automated world, interest in the field of robotics is surging, with an exciting branch of this area being legged robotics. These biologically inspired robots have leg-like limbs which enable locomotion, suited to challenging terrains which wheels struggle to conquer. While it has been quite some time since the idea of a legged machine was first made a reality, this technology has been modernised with compliant legs to improve locomotion performance. Recently, developments in biological science have uncovered that humans and animals alike control their leg stiffness, adapting to different locomotion conditions. Furthermore, as these studies highlighted potential to improve upon the existing compliant-legged robots, modern robot designs have seen implementation of variable stiffness into their legs. As this is quite a new concept, few works have been published which document such designs, and hence much potential exists for research in this area. As a promising technology which can achieve variable stiffness, magnetorheological (MR) smart materials may be ideal for use in robot legs. In particular, recent advances have enabled the use of MR fluid (MRF) to facilitate variable stiffness in a robust manner, in contrast to MR elastomer (MRE).

Developed in this thesis is what was at the time the first rotary MR damper variable stiffness mechanism. This is proposed by the author for use within a robot leg to enable rapid stiffness control during locomotion. Based its mechanics and actuation, the leg is termed the magnetorheological variable stiffness actuator leg mark-I (MRVSAL-I). The leg, with a C-shaped morphology suited to torque actuation is first characterised through linear compression testing, demonstrating a wide range of stiffness variation. This variation is in response to an increase in electric current supplied to the internal electromagnetic coils of the MR damper. A limited degrees-of-freedom (DOF) bipedal locomotion platform is designed and manufactured to study the locomotion performance resulting from the variable stiffness leg. It is established that optimal stiffness tuning of the leg could achieve reduced mechanical cost of transport (MCOT), thereby improving locomotion performance. Despite the advancements to locomotion demonstrated, some design issues with the leg required further optimisation and a new leg morphology.

To improve upon the imbalance caused by the former leg morphology and increase functional deflection range, a revised variable stiffness leg is designed and manufactured, the MRVSAL-II. Through force characterisation, the leg is shown to achieve adequate stiffness variation for further experimentation. The leg is also mathematically modelled,

with the hysteretic behaviour of the included MR damper captured well. To give indication of the improved stability the variable stiffness behaviour of the leg can offer, steps-to-fall analysis is conducted. Shown through the spring loaded inverted pendulum (SLIP) modelling within this analysis, the stability region of the model can be enhanced through careful selection of damper current and hence leg stiffness. For the design-stiffness range of the leg, generally the higher end of the stiffness range results in greater stability.

An important consideration for legged robot locomotion is the ability of the platform to mitigate variation to gait trajectory in response to encountered disturbances. In particular, coronal gradients can cause severe variation in roll angle during locomotion if not managed. Furthermore, such gradients may occur momentarily through increases or decreases in terrain elevation, i.e. obstacles or valleys, respectively, then they are asymmetric about the sagittal plane. To investigate the potential of variable stiffness in compensating for such disturbances, the previously employed bipedal locomotion platform is revised to facilitate roll-angle motion and suit the MRVSAL-II. Through numerous experiments featuring adaptive leg stiffness control, it is established that roll angle stability can be improved when compared with the performance of passively compliant legs.

Another meaningful area to pay attention to for legged robots is the way in which they manage impact landings and experience shock loads. High impact forces may not only cause immediate failure of robot legs and other hardware, but otherwise can accelerate mechanical fatigue, leading to greater maintenance requirements or unexpected failure. To study the capacity of MR variable stiffness to reduce impact loads in legged robots, the MRVSAL-II is employed in drop testing experiments, with a test rig designed and manufactured for this purpose. It is established that when compared to a low stiffness and low damping leg, the MR variable stiffness reduces the risk of large deflections and ground collisions which result in high impact loads. Furthermore, with greater energy dissipation, prolonged robot vibration is also mitigated. When compared to a high stiffness and high damping leg, MR variable stiffness also substantially reduces the shock loads experienced by the legged robot platform. By monitoring robot kinetic energy at the point of impact, a practical control algorithm is presented to control the MRVSAL-II leg stiffness to optimally reduce impact loads, also protecting against excessive deflection which leads to ground collisions.

ACKNOWLEDGEMENTS

First and foremost, I would like to express my sincere gratitude to Snr. Prof. Weihua Li, who has been my Primary Supervisor since my undergraduate study. Throughout this time, he has made great efforts to support my research at the University of Wollongong and sponsor my research abroad and conference participation. Beyond this, he has always made an effort to support my academic career progression, sharing his wisdom over coffee breaks and finding many opportunities for me with various roles and responsibilities. For this, I am thankful. Of equal importance to my research, I would not have been able to accomplish what I have without the direct support of my Co-Supervisor, Prof. Shuaishuai Sun. Identically, he has been a mentor of mine since my undergraduate study and has always encouraged me to explore new ideas to conduct meaningful work. Wherever there was a doubt, he was always able to reassure me and steer me onto the right track. Despite supervising me from a global distance at times, he somehow always found time to help, which I sincerely appreciate.

I would also like to thank Prof. Haiping Du and Prof. Donghong Ning, offering additional support throughout my research, sharing useful advice for my work. In addition, I was lucky to have conducted some of my work abroad as a visiting researcher at the University of Science and Technology of China, with supervision and support from Prof. Shiwu Zhang. I greatly appreciate the time he afforded me there, allowing me to freely work in his labs alongside his other students. In our lab, I was also lucky to work with many exceptional people, namely my lab-mate Lei Deng, and to them I would also like to say thanks for your support, thanks for being there for a chat, and thanks for being the small handful of people who understood the exact, sometimes trivial, struggles we experienced with our projects. Beyond the lab, a big thank you to all of the excellent University of Wollongong technical staff who have supported my work over the years.

Lastly, I would like to thank my family. To my father, Anthony Christie, you have always provided me with a place to call home and never expected much in return. This made it possible for me to study and not have to worry much about money. To my mother, Vicki Christie, thank you for always being there, from pre-school to primary-school to high-school, you always made an effort to support my education, for which I will always be grateful. Because of you, I not only have a Bachelor's degree, but now a PhD. To my partner, Val Sun, you have always been there during my PhD, supporting me through all of the individual milestones of my academic career so far. While at times you let me be busy with work, you also reminded me to have fun and enjoy life. Thank you for being my best company during this time.

~~~ In loving memory of my cat, Meow Meow, 2010-2021 ~~~

TABLE OF CONTENTS

DECLARATION i

ABSTRACT ii

ACKNOWLEDGEMENTS iv

TABLE OF CONTENTS v

LIST OF FIGURES ix

LIST OF TABLES xiii

LIST OF ABBREVIATIONS xiv

NOMENCLATURE xv

1 INTRODUCTION 1

1. 1 Research Background and Motivation 1

1. 2 Research Objectives 4

1. 3 Outline 4

2 LITERATURE REVIEW 6

2. 1 Introduction 6

2. 2 Overview of Legged Robot Locomotion 6

2.2.1 Biological Context 6

2.2.2 Legged Robot Designs and Uses 8

2.2.3 Measures of Performance for Locomotion 10

2.2.4 Dynamic Modelling Approaches 11

2. 3 From Passive to Variable Stiffness in Legged Locomotion 13

2.3.1 Passively Compliant Robot Legs 13

2.3.2 Variable Stiffness Robot Legs 14

2. 4 Magnetorheological Materials 17

2.4.1 Material Properties and Working Mechanism 17

2.4.2 System Dynamic Models for MR Fluid 19

2.4.3 Existing Uses and Applications of MR Fluid 20
2.4.4 Advantages and Limitations of MR Fluid in Legged Robotics 22
2. 5 Chapter Summary 22
3 A ROBOT LEG WITH HIGH STIFFNESS ADJUSTABILITY FOR ENHANCING LOCOMOTIVE PERFORMANCE 24
3. 1 Introduction 24
3. 2 Design and Working Mechanism of the MRVSAL-I 25
3.2.1 Leg Structure 25
3.2.2 Design of the Rotary MR Damper 28
3.2.3 Working Mechanism 30
3. 3 Leg Characterisation 33
3. 4 Locomotion Testing 36
3. 5 Chapter Summary 39
4 IMPROVED MAGNETORHEOLOGICAL-FLUID-BASED VARIABLE STIFFNESS FOR LEGGED LOCOMOTION AND SLIP STABILITY 40
4. 1 Introduction 40
4. 2 MRVSAL-II Design 41
4.2.1 Leg Morphology and Design 41
4.2.2 Magnetorheological Damper Modelling 44
4. 3 Leg Experimental Characterisation 45
4.3.1 Compression Testing Experimental Setup 45
4.3.2 Test Results and Analysis 46
4. 4 Leg Force Modelling 51
4. 5 Steps-to-Fall Stability Analysis 56
4.5.1 Continuous Running SLIP Model Setup 56
4.5.2 Locomotion Simulation Results 58
4. 6 Chapter Summary 62

5 REAL-TIME ADAPTIVE LEG-STIFFNESS FOR ROLL COMPENSATION VIA MAGNETORHEOLOGICAL CONTROL IN A LEGGED ROBOT 63

5. 1 Introduction 63

5. 2 Locomotion Experimental Setup 64

5.2.1 Test-Platform Design and Control 64

5.2.2 Stiffness Control Modes 66

5. 3 Obstacle and Valley Disturbance Mitigation 68

5. 4 Coronal Gradient Compensation 73

5. 5 Resonant Locomotion 76

5. 6 Chapter Summary 78

6 SHOCK ABSORPTION FOR LEGGED LOCOMOTION THROUGH MAGNETORHEOLOGICAL LEG-STIFFNESS CONTROL 79

6. 1 Introduction 79

6. 2 Experimental Setup 81

6. 3 Experimental Procedure 84

6. 4 Passive Control 84

6.4.1 Experimental Results 84

6. 5 Impact-Force Control 94

6.5.1 Controller Development 94

6.5.2 Experimental Results 96

6. 6 Chapter Summary 97

7 CONCLUSIONS AND FUTURE WORK 102

7. 1 Achieving Variable Stiffness with a Rotary MR Damper 102

7.1.1 Variable Stiffness Behaviour in Robot Legs 102

7.1.2 Robot Leg Design 103

7. 2 Locomotion of Legged Robots with MRF-Based Variable Stiffness 103

7.2.1 Resonant Running and Cost of Transport 103

7.2.2 Manoeuvring Disturbances Using Variable Stiffness 104

7.2.3 Impact Protection Through Leg Stiffness Control 104

7. 3 Recommendations for Future Work 105

7.3.1 Reduction in Energy Cost of MRF-Based Variable Stiffness 105

7.3.2 Investigation of Variable Stiffness Combined with Variable Damping in Robot Legs 105

7.3.3 Use of Alternative Smart Materials to Achieve Variable Stiffness in Robot Legs 105

7.3.4 Experimental Investigation of Unconstrained Locomotion with MRF-Based Variable Stiffness Robot Legs 106

PUBLICATIONS INCLUDED IN THIS WORK 107

Journal Articles 107

ADDITIONAL PUBLICATIONS DURING CANDIDATURE 107

Journal Articles 107

Conference proceedings 108

REFERENCES 109

LIST OF FIGURES

Figure 2-1 Examples of differing gaits amongst different species, including (a) walk or run, (b) hop, and (c) tripod; adapted from [33]. 7

Figure 2-2 Boston Dynamic's Spot, a modern quadruped legged robot [40]. 8

Figure 2-3 SLIP model (a) intrinsic parameters, and (b) dynamic behaviour [53]. 11

Figure 2-4 A passively compliant robot leg; adapted from [21]. 14

Figure 2-5 A variable stiffness robot leg; adapted from [49]. 15

Figure 2-6 A variable stiffness robot leg featuring an MRE joint [62]. 15

Figure 2-7 Alignment of iron particles in MRF used in shear mode due to magnetic field. 18

Figure 2-8 Common dynamic models for rotary MR dampers. 19

Figure 2-9 Variable stiffness and variable damping MR shock absorber [29]. 20

Figure 3-1 MRVSAL-I CAD model (a) side view, and (b) rear view (dims in mm). 25

Figure 3-2 R-SLIP static model parameters. 27

Figure 3-3 Compact rotary MR damper (dims in mm). 28

Figure 3-4 Magnetic field FEM analysis (a) mean flux through MRF, (b) joint model. 29

Figure 3-5 Variable stiffness rotary MR damper mechanism. 30

Figure 3-6 Force characterisation experimental setup. 33

Figure 3-7 Experimentally measured and model calculated leg force under varied current. 34

Figure 3-8 Relationship between current and effective stiffness. 35

Figure 3-9 Locomotion test rig CAD model (dims in mm). 36

Figure 3-10 Experimental setup for limited-DOF legged locomotion testing. 37

Figure 3-11 MCOT of bipedal test platform equipped with MRVSAL-I. 38

Figure 4-1 MRVSAL-II CAD model (a) rear-view, and (b) side-view. 41

Figure 4-2 Variable stiffness mechanism (a) CAD model sectional view, and (b) functional diagram. 42

Figure 4-3 Improved rotary MR damper mean MRF magnetic flux density. 44

Figure 4-4 Force characterisation results (exp. and sim.) under (a) variable damper current with 10 mm displacement and 5 mm/s speed, (b) variable damper current with 15 mm displacement and 5 mm/s speed..... 46

Figure 4-5 Effective leg stiffness for varied damper current. 47

Figure 4-6 Force characterisation results under variable displacement. 48

Figure 4-7 Force characterisation results under (a) variable loading speed with 10 mm displacement, (b) variable loading speed with 15 mm displacement..... 49

Figure 4-8 MRVSAL-II linkage geometric parameters. 54

Figure 4-9 MRVSAL-II lower leg segment free body diagram. 54

Figure 4-10 Simulated stable (steps ≥ 24) and unstable (steps < 24) SLIP locomotion. 57

Figure 4-11 Steps-to-fall analysis of SLIP model with characteristic leg spring of stiffness (a.1)-(g.1) $\mathrm{ke} = 2.51\ \mathrm{N/mm}$, (a.2)-(g.2) $\mathrm{ke} = 3.13\ \mathrm{N/mm}$, (a.3)-(g.3) $\mathrm{ke} = 4.14\ \mathrm{N/mm}$, and (a.4)-(g.4) $\mathrm{ke} = 4.61\ \mathrm{N/mm}$..... 58

Figure 4-12 Percentage of valid SLIP locomotion trials. 60

Figure 4-13 Percentage of stable SLIP locomotion trials. 61

Figure 5-1 Improved limited-DOF bipedal locomotion experimental setup. 64

Figure 5-2 Locomotion phases during unidirectional torque actuation. 65

Figure 5-3 Locomotion test scenarios with (a) one asymmetric obstacle, (b) one asymmetric valley, (c) multiple asymmetric obstacles, (d) 5° coronal gradient, (e) 10° coronal gradient, and (f) unobstructed flat terrain. 65

Figure 5-4 Adaptive stiffness control algorithm process flow diagram. 66

Figure 5-5 Asymmetric obstacle 2 rad/s leg speed (a) roll angle, and (b) right leg damper current. 67

Figure 5-6 Asymmetric obstacle (a) MCOT, (b) average horizontal velocity, (c) average leg torque, (d) vertical displacement range, (e) peak roll angle, and (f) RMS roll angle. 69

Figure 5-7 Asymmetric obstacle platform vertical position at 2 rad/s leg speed with control mode (a) 0 A passive, (b) 2 A passive, and (c) adaptive. 70

Figure 5-8 Asymmetric valley (a) MCOT, (b) average horizontal velocity, (c) average leg torque, (d) vertical displacement range, (e) peak roll angle, and (f) RMS roll angle. 71

Figure 5-9 Multiple asymmetric obstacles (a) MCOT, (b) average horizontal velocity, (c) average leg torque, (d) vertical displacement range, (e) peak roll angle, and (f) RMS roll angle..... 72

Figure 5-10 Coronal 5° gradient (a) MCOT, (b) average horizontal velocity, (c) average leg torque, (d) vertical displacement range, (e) peak roll angle, and (f) RMS roll angle. 74

Figure 5-11 Coronal 10° gradient (a) MCOT, (b) average horizontal velocity, (c) average leg torque, (d) vertical displacement range, (e) peak roll angle, and (f) RMS roll angle. 75

Figure 5-12 Unobstructed flat terrain (a) MCOT, (b) average horizontal velocity, (c) average leg torque, (d) and vertical displacement range. 77

Figure 6-1 Impact loading experimental setup (a) layout, and (b) control system. 81

Figure 6-2 Impact loading free body diagram at (a) moment of impact, and (b) during impact. 82

Figure 6-3 COM displacement for impact tests with a 2.65 kg total mass for drop heights of (a) 100 mm, (b) 200 mm, (c) 300 mm, (d) 400 mm, (e) 500 mm, and (f) 600 mm. 84

Figure 6-4 COM displacement for impact tests with a 4.60 kg total mass for drop heights of (a) 100 mm, (b) 200 mm, (c) 300 mm, (d) 400 mm, (e) 500 mm, and (f) 600 mm. 86

Figure 6-5 Settling time for impact tests with total masses of (a) 2.65 kg, and (b) 4.60 kg. 87

Figure 6-6 Leg impact force for impact tests with a 2.65 kg total mass for drop heights of (a) 100 mm, (b) 200 mm, (c) 300 mm, (d) 400 mm, (e) 500 mm, and (f) 600 mm. 89

Figure 6-7 Leg impact force for impact tests with a 4.60 kg total mass for drop heights of (a) 100 mm, (b) 200 mm, (c) 300 mm, (d) 400 mm, (e) 500 mm, and (f) 600 mm. 91

Figure 6-8 Peak impact force for impact tests with masses of (a) 2.65 kg, and (b) 4.60 kg.....92

Figure 6-9 Impact force controller (a) damper control signal, and (b) process flow diagram.....94

Figure 6-10 Controlled impact force for impact tests at all drop heights with total masses of (a) 2.65 kg, and (b) 4.60 kg.....97

Figure 6-11 Controller improvement in peak impact force for impact tests with total masses of (a) 2.65 kg, and (b) 4.60 kg. 98

Figure 6-12 Controlled COM displacement for impact tests at all drop heights with total masses of (a) 2.65 kg, and (b) 4.60 kg. 99

Figure 6-13 Controller improvement in settling time for impact tests with total masses of (a) 2.65 kg, and (b) 4.60 kg.....100

LIST OF TABLES

Table 2-1 Review of various legged robot platforms. 9

Table 2-2 Design and performance comparison of variable stiffness robot legs. 17

Table 2-3 Advantages and challenges faced by MRF for variable stiffness robot legs. 21

Table 3-1 MR damper geometric properties. 31

Table 3-2 MRVSAL-I force-model parameters. 34

Table 3-3 Calculated effective stiffness values of the MRVSAL-I. 35

Table 4-1 Calculated effective stiffness values of the MRVSAL-II. 48

Table 4-2 MRVSAL-II geometric parameters. 50

LIST OF ABBREVIATIONS

ABS	Acrylonitrile Butadiene Styrene
CAD	Computer aided design
COM	Centre of mass
COT	Cost of transport
DAQ	Data acquisition
DC	Direct current
DOF	Degrees of freedom
FDM	Fusion deposition modelling
FEM	Finite element method
LO	Lift-off
MAX	Maximum
MCOT	Mechanical cost of transport
MIN	Minimum
MR	Magnetorheological
MRE	Magnetorheological elastomer
MRF	Magnetorheological fluid
MRVSAL	Magnetorheological-fluid-based variable stiffness actuator leg
RMS	Root mean square
R-SLIP	Rolling-contact spring loaded inverted pendulum
SEA	Series elastic actuator
SLIP	Spring loaded inverted pendulum
STF	Shear thickening fluid
TD	Touchdown
VIA	Variable impedance actuator
VSA	Variable stiffness actuator

NOMENCLATURE

α	SLIP model parameter: touchdown angle [rad]
b	MRVSAL-II geometric parameter: foot thickness [m]
B	General magnetic flux density [T]
B_i	Magnetic flux density within inner rotary MR damper gap [T]
B_o	Magnetic flux density within outer rotary MR damper gap [T]
β	SLIP model parameter: landing angle [rad]
c_0	General MRF viscous damping coefficient [N·m·s/rad]
c_n	Herschel-Bulkley MRF rotary viscous damping coefficient [N·m·s/rad]
c_{MR}	Rotary MR damper viscous damping coefficient [N·m·s/rad]
c_{body}	MRVSAL-II body-contributed viscous damping coefficient [N·m·s/rad]
COT	Cost of transport
d_{COMy}	Vertical displacement of robot centre of mass [m]
d_{drop}	Drop height of robot for drop tests [m]
E_{Ky}	Vertical component of robot kinetic energy [J]
E_P	Robot gravitational potential energy [J]
f_s	Locomotion stride frequency [Hz]
F_C	MRVSAL-II cable force [N]
F_l	MRVSAL-I leg force [N]
F_{LC1}	Drop test system load cell 1 force [N]
F_{LC2}	Drop test system load cell 2 force [N]
F_{Px}	MRVSAL-II horizontal reaction force at point *P* [N]
F_{Py}	MRVSAL-II vertical reaction force at point *P* [N]
F'_{Py}	MRVSAL-II apparent contact force at point *P* [N]
F_{Ry}	Impact force during drop tests [N]
$F_{Ry,max}$	Peak impact force during drop tests [N]
$F_{\Delta,max}$	MRVSAL-II force at corresponding maximum deflection [N]
$F_{\Delta,min}$	MRVSAL-II force at corresponding minimum deflection [N]
g	Gravitational acceleration, 9.81 [m/s^2]
γ	MRVSAL-I geometric parameter: joint position angle [rad]
γ_0	MRVSAL-I geometric parameter: initial joint position angle [rad]

H	General magnetic field strength [kA/m]
H_i	Magnetic field strength within inner rotary MR damper gap [kA/m]
H_o	Magnetic field strength within outer rotary MR damper gap [kA/m]
I	Electric current supplied to coil windings of rotary MR damper [A]
k	SLIP model parameter: linear spring stiffness [N/m]
k_{actual}	MRVSAL-II linkage structure stiffness [N/m]
k_{biped}	Parallel leg stiffness of bipedal robot platform [N/m]
k_e	Effective vertical leg stiffness [N/m]
$k_{leg,L}$	Biped left leg effective vertical stiffness [N/m]
$k_{leg,R}$	Biped right leg effective vertical stiffness [N/m]
k_{rigid}	MRVSAL-II effective stiffness for a completely rigid structure [N/m]
k_{soft}	Variable stiffness mechanism softer torsional spring stiffness [N·m/rad]
k_{stiff}	Variable stiffness mechanism stiffer torsional spring stiffness [N·m/rad]
k_t	MRVSAL-I joint effective torsional stiffness [N·m/rad]
l_0	SLIP model parameter: leg-spring free length [m]
l_a	MRVSAL-I geometric parameter: contact-point to joint length [m]
l_A	MRVSAL-II geometric parameter: position of point A [m]
l_b	MRVSAL-I geometric parameter: compressed linear spring length [m]
l_{AP}	MRVSAL-II geometric parameter: distance from point A to point P [m]
l_C	MRVSAL-II geometric parameter: position of point A [m]
l_{CD}	MRVSAL-II geometric parameter: distance from point C to point D [m]
l_D	MRVSAL-II geometric parameter: position of point D [m]
l_j	MRVSAL-I geometric parameter: hip to joint length [m]
l_P	MRVSAL-II geometric parameter: position of point P [m]
λ	MRVSAL-I geometric parameter: reciprocal moment arm [m^{-1}]
m	SLIP model parameter: locomotor point mass [kg]
m_{biped}	Bipedal robot platform total mass [kg]
m_{total}	Total effective robot platform mass [kg]
$MCOT$	Mechanical cost of transport
n	Herschel-Bulkley flow behaviour index
μ_k	Kinetic friction coefficient

μ_r	Magnetic relative permeability
ω_{fligh}	Biped flight phase leg-speed [rad/s]
ω_{leg}	Biped leg rotational speed [rad/s]
ω_n	Natural frequency [rad/s]
ω_{stanc}	Biped stance phase leg-speed [rad/s]
P_{avg}	Average power consumption during locomotion [W]
ϕ	Bipedal locomotion platform roll angle [rad]
ψ	General rotary MR damper angular deflection [rad]
$\dot{\psi}$	General rotary MR damper angular velocity [rad/s]
ψ_0	Rotary MR damper variable stiffness mechanism input deflection [rad]
ψ_1	Rotary MR damper variable stiffness mechanism rotor deflection [rad]
ψ_2	Rotary MR damper variable stiffness mechanism output deflection [rad]
r	MRVSAL-I geometric parameter: C-shaped leg radius [m]
r_A	MRVSAL-II geometric parameter: foot radius [m]
r_H	MRVSAL-II geometric parameter: damper housing pulley radius [m]
r_i	Rotary MR damper inner drum radius [m]
r_o	Rotary MR damper outer drum radius [m]
t_s	Settling time [s]
T_{leg}	Bipedal locomotion platform leg torque [N·m]
T_{MR}	Rotary MR damper torque [N·m]
T_{VS}	MRVSAL-I variable stiffness mechanism torque [N·m]
$T_{VS,in}$	MRVSAL-II variable stiffness mechanism input torque [N·m]
$T_{VS,out}$	MRVSAL-II variable stiffness mechanism output torque [N·m]
T_η	Viscous damping component of rotary MR damper torque [N·m]
T_τ	Coulomb friction component of rotary MR damper torque [N·m]
τ_{hig}	General high shear stress of MRF [Pa]
τ_{low}	General low shear stress of MRF [Pa]
τ_y	General shear yield stress of MRF [Pa]
$\tau_{y,i}$	Shear yield stress at inner rotary MR damper gap [Pa]
$\tau_{y,o}$	Shear yield stress at outer rotary MR damper gap [Pa]
θ_1	MRVSAL-II geometric parameter: angle 1 [rad]

θ_2	MRVSAL-II geometric parameter: angle 2 [rad]
θ_3	MRVSAL-II geometric parameter: angle 3 [rad]
θ_4	MRVSAL-II geometric parameter: angle 4 [rad]
v_{COMy}	Vertical velocity of robot centre of mass [m]
v_{TD}	SLIP model parameter: touchdown velocity [m/s]
v_{avg}	Locomotor average horizontal 'forwarding' velocity [m/s]
v_{impact}	Impact velocity of robot centre of mass [m]
w_i	Rotary MR damper inner drum active width [m]
w_o	Rotary MR damper outer drum active width [m]
x	Horizontal displacement or position [m]
$\dot{x}_{LO}$	SLIP model parameter: COM lift-off velocity [m/s]
$\ddot{x}$	Horizontal acceleration [m/s^2]
ξ	MRVSAL-I geometric parameter: position angle of joint [rad]
y	Vertical displacement or position [m]
y_{LO}	SLIP model parameter: COM lift-off vertical position [m]
y_{TD}	SLIP model parameter: COM touchdown vertical position [m]
$\ddot{y}$	Vertical acceleration [m/s^2]
$\dot{y}_{LO}$	SLIP model parameter: COM lift-off vertical velocity [m/s]
Δy_l	MRVSAL-I input vertical displacement [m]
Δy_P	MRVSAL-II input vertical displacement [m]
$\Delta y_{P,max}$	MRVSAL-II maximum input vertical displacement [m]
$\Delta y_{P,min}$	MRVSAL-II minimum input vertical displacement [m]
ζ	Damping ratio

1 INTRODUCTION

1. 1 Research Background and Motivation

The now booming field of legged robotics is one in which biological inspiration has played a major role. Legged animals use the ligaments and tendons of their limbs to convert gravitational potential and kinetic energy of their bodies into strain energy during leg compression, subsequently returning this in the later-half of each step, providing cyclic and stable locomotion [1]. In other words, animals and humans alike, make use of leg-like limbs which facilitate some level of compliance to not only behave as actuators, but also to act as springs which store and release energy. Similarly, for stable and energy efficient locomotion in legged robots, leg compliance is paramount. Hence, several designs of legged robots with passive compliance in their legs have been developed over the years, with exemplars of high notoriety including: Raibert's hoppers [2], SCOUT [3], RHex [4], Whegs [5], and Tekken [6].

Regarding some of the specialised uses for legged robots, these include navigation through terrains where it is either impractical or possibly hazardous for manned-missions, and wheeled robots are otherwise ill-suited to. Such scenarios in which these cases may exist could be: disaster relief efforts, bomb disposal, other military or law-enforcement-based activities, and exploration of extra-terrestrial environments [7]. Now, with great progress made in this field, and developments such as legged robots conquering stair cases [7] and wetted granular material [8], links to studies on humans and animals have been identified, which have made way for a new focus: controllable leg stiffness [9-11].

The analogy of a locomoting legged body to a simple spring-mass system has widely been used in modern robotics, dating as far back as 1989, when first proposed by Blickhan [12]. In accordance with fundamental system-dynamic theory, we can then consider animals and legged robots of all sizes to behave as spring-mass systems [13], where both their effective leg stiffness and the stiffness of the terrain upon which they run would be acting in series [11]. Consequently for the locomotor, their desired or optimal stride frequency would then depend on both their body mass and this effective series stiffness. This suggests optimal tuning and modulation of leg stiffness to suit a given or changing terrain could lead to resonant, energy efficient locomotion, as varied leg stiffness maintains a stable gait pattern [14]. Such behaviour has been evidenced through multiple biological studies [9-11, 15], wherein animals and humans showed that upon transitions to surfaces of different stiffnesses, leg stiffness was adjusted upon the first step to compensate. Furthermore, it has been found that humans and other biological species modulate leg stiffness in preparation of encounters with obstacles or valleys [16, 17].

This may then lead one to wonder, w*hy not design legged robots to do the same thing?* Unsurprisingly, this has in fact already been done, and not even limited to the field legged robotics. Actually, the concept of having an elastic element in series with an actuator, i.e. a series elastic actuator (SEA), has widely been researched in many fields, including industrial applications, such as in robot arms purposed for manufacture [18]. As it has been established here the practicality and usefulness of variable stiffness in robot legs, this idea has not gone unnoticed in the broader scope of which SEAs covers. As such, the topic of variable stiffness actuators (VSAs) in general has now become a heated research area [18-20]. That being said, for legged robotics, as this concept is quite new and relatively niche, few works have been published on the topic of variable stiffness in robotic legged locomotion, highlighting great potential for research in this area.

Regarding some of the existing publications discussing design of variable stiffness robot legs, some of note are: EduBot's variable stiffness C-shaped legs developed by Galloway et al. [21], the linear mechanism for varying stiffness via transmission angle (L-MESTRAN) from Vu et al. [22], and the differential cable-driven leg, which achieves variable stiffness through spring-pretensioning, developed by Hurst et al. [23]. While the mechanism of each design may differ, these examples

provide limbs which facilitate stiffness control in legged robots. Not limited to these cases but also in general, detailed investigation into the benefits of variable stiffness in legged robots is lacking from the few works published in this area. Such gaps left in literature have inspired this work to focus on just that: fabrication of novel variable stiffness legs and performing detailed investigation into the theorised benefits offered by stiffness control.

As for the need of variable stiffness legs to conduct this research, a key innovation of this work is employing magnetorheological (MR) materials, MR fluid (MRF) specifically, to achieve variable stiffness in robot legs. This smart material is essentially composed of a host fluid containing ferromagnetic micro-particles which under the application of a magnetic field will align to form chains; on a macro-scale, the observed behaviour of the fluid is an increase in viscosity. When employed in a device such as a fluid damper, electric-current-dependant damping can be realised using a solenoid, which has led to common use in control of dynamic systems such as vehicle suspension [24], and improving structural stability through tuned mass damper design [25-27]. While MRF also has very recently been used in adaptive robot leg design [28], to achieve variable stiffness with this material is new and quite promising [29-31]. In such a design, if the damping is controlled, the effective stiffness of the device will be controlled as a predominant behaviour. A key drawback of existing variable stiffness robot leg designs, is the stiffness tuning time requirement, which may be in the order of seconds [21], therefore preventing dynamic stiffness control, i.e. instant adjustment whilst running. Owing to the favourable characteristics of MRF, namely a rapid response time and simplicity of control [32], it may be key in improving performance in robot locomotion. Potential areas of improvement include: energy efficiency or a lower cost of transport, locomotion stability, and disturbance rejection capability.

1. 2 Research Objectives

To clarify the main goals proposed for this work, they are listed in chronological order below:

- Design, fabricate, and optimise variable stiffness legs using MR technology.
- Characterise legs through modelling and experimental load testing.
- Design, fabricate, and commission a constrained bipedal locomotion platform for simplified locomotion experiments.
- Experimentally evaluate ability of variable stiffness legs to improve locomotion performance and manage disturbances, including: obstacles, valleys, and sloped-surface encounters.
- Design and fabricate a drop-testing system to experimentally investigate ability of variable stiffness legs to mitigate impacts.
- Conduct impact-loading drop test experiments of variable stiffness robot legs to evaluate performance.

1. 3 Outline

Following the introduction, this thesis is structured into the following chapters in the outlined order:

Chapter 2 presents a critical literature review on legged locomotion from its biological context to a survey of existing legged robots, including performance measures and basic modelling approaches. This review is then targeted towards leg compliance and variable stiffness in legged robots. The field of magnetorheological materials is lastly introduced, with material behaviour and existing applications studied.

Chapter 3 details the development of the first iteration of a magnetorheological-fluid-based variable stiffness robot leg (MRVSAL-I). Included within is experimental compression testing, force modelling, and rudimentary locomotion studies using bipedal constrained locomotion platform.

Chapter 4 proposes an improved second iteration of a magnetorheological-fluid-based variable stiffness robot leg (MRVSAL-II) for further experimental studies. Following experimental compression testing and modelling efforts on the leg, steps-to-fall stability analysis is conducted to verify the efficacy of the designed stiffness range.

Chapter 5 details development of an improved bipedal robot platform with fewer kinematic constraints to facilitate disturbance-based locomotion trials. Making use of the MRVSAL-II, experiments are conducted to investigate interactions with obstacles, valleys, and coronal gradients, and study the performance of adaptive leg stiffness control.

Chapter 6 studies the MRVSAL-II in a drop-testing system fabricated to facilitated impact loading experiments. By means of experimentally analysing the impact loading performance of the leg under different conditions, an impact-buffering control regime is established for legged robots fitted with these legs.

Chapter 7 summarises and concludes the main findings of this thesis, outlining and briefly discussing potential directions for future research in this field.

2 LITERATURE REVIEW

2. 1 Introduction

This chapter is a critical review of literature capturing the essence of legged robot locomotion, also highlighting the gaps left in existing literature within the scope of variable stiffness in legged locomotion. Analysed in this review are three major research areas: legged locomotion in robots, compliant and variable stiffness robot leg designs, and lastly a review of the behaviour and existing applications of magnetorheological fluid.

2. 2 Overview of Legged Robot Locomotion

2.2.1 Biological Context

So, what is legged locomotion and why do we want robots to do this, anyway? In nature, countless living species have come to possess leg-like limbs through the process of evolution. Such limbs facilitate terrestrial land-based, and in some cases water-based, movement from point A to point B: this is legged locomotion. While this is an easy concept to grasp, as we humans are similarly legged locomotors, what may not be as obvious is how this changes from species to species, or even within the same individual. The way this legged locomotion is achieved in terms of the repetitious patterns of steps taken is referred to as a ‘gait’ or ‘gait pattern’. With a set of characteristic gaits being common to most locomotors, these differ along with parameters such as number of legs, body mass, and body shape [1]. As a visual representation of this, in **Figure 2-1** are the sequence of steps forming a single gait

cycle or ‘stride’ in: (a) walking or running for a biped, (b) hopping for a biped, which is similar to ‘pronking’ for a quadruped, and (c) a ‘tripod gait’ commonly found in sprawl-type hexapods.

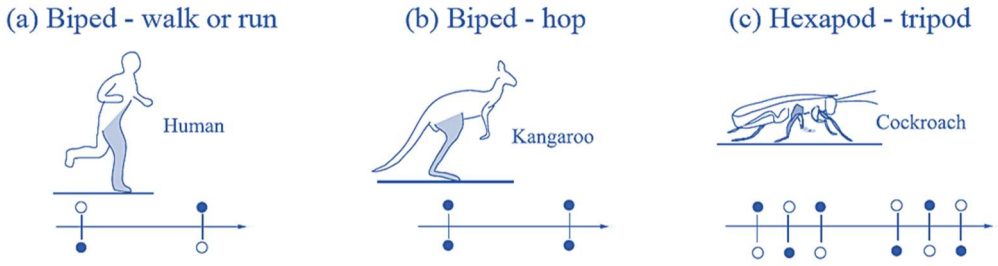

Figure 2-1 Examples of differing gaits amongst different species, including (a) walk or run, (b) hop, and (c) tripod; adapted from [33].

Another question that may now be raised is, *if a given species possess the ability to move with different gaits, how do they decide which to choose?* In short, specific speeds are known to exist at which comfortable and seamless transition between gaits will occur [13, 34], which also depends on the terrain upon which the locomotor runs [10]. Similar to how we humans experience discomfort if we walk too fast and would rather be running at that speed, this trait is common throughout nature and is considered an artefact of the minimisation of energy consumption during locomotion [12, 35, 36].

As another way of optimising energy consumption, aside from gait variation, it has been reported in numerous biological studies that leg stiffness variation plays a key role in energy efficient locomotion [9, 10, 37, 38]. To expand upon this idea, it is understood that legged locomotors behave much like simple spring-mass systems, where a body mass pivots about a surface through a virtual leg spring with an effective vertical stiffness [12]. This stiffness is formed between the locomotor’s body and the ground, also inclusive of the series ground stiffness formed while running on compliant surfaces [10, 11, 38]. Given the stiffness-dependant stride frequency of such a spring-mass system is a key parameter in legged locomotion [13], it is for this reason as to why leg stiffness modulation leads to essentially tuned resonant, energy efficient locomotion [21].

2.2.2 Legged Robot Designs and Uses

It should be no surprise that as seen in nature, legged machines could be designed similarly to take advantage of the extensive body of knowledge surrounding biological locomotors. And while much of the previously mentioned biological studies were published around the mid to late 1900s, design of basic walking mechanisms dates as far back as 1850 [2]. On this scale it is quite a recent development to see more-intelligent and computerised machines emerge, with more modern robots like Raibert's hoppers taking advantage of biological traits such as compliant legs, anchored in aforementioned spring-mass dynamic modelling approaches [2, 10]. Since Raibert's 1986 work in this area, many innovative and unique robot platforms have been developed with similar inspirations from nature, as included in **Table 2-1**, some examples of high notoriety being: SCOUT, the simple hip-motor actuated quadruped published in 1998 by Buehler et al.; RHex, a biologically inspired sprawl-postured hexapod, first presented in 2001 by Saranli et al. [4]; the 2008 published BigDog, a rugged combustion-engine driven quadruped, being a more recent work of Raibert et al. [39]; and Boston Dynamic's Spot, a quadruped which came as an evolution of BigDog in 2016 before becoming commercially available in 2019 [40], illustrated in **Figure 2-2**.

Figure 2-2 Boston Dynamic's Spot, a modern quadruped legged robot [40].

Table 2-1 Review of various legged robot platforms.

Robot Platform	No. of Legs	Gaits	Mass (kg)	Max. Speed (m/s)	Max. Speed (BL/s)	Special Features
'3D Pogo-hopper' [2]	1	Hop	-	2.2	-	• Early implementation of compliant legs to improve dynamic stability
ASIMO [41]	2	Walk, run	52	0.44	~2.22	• Humanoid design • Intelligent sensory recognition of human gestures
'Kangaroo hopper' [42]	2	Hop	5.4	-	-	• Tail to improve dynamic stability • C-shaped rolling contact legs to improve dynamic stability
SCOUT-1 [3]	4	Walk, pronk	1.2	1.5	7.89	• Simple 1 DOF per leg design, capable of both walking and pronking
Tekken [6]	4	Walk, trot	~15	1.1	3.93	• Autonomous gait transition to minimise energy cost
Mini-Whegs [43]	4	Diagonal	0.09	0.27	3	• Wheel-legs with compliant foot pads to improve mobility • Hopping lever mechanism to jump over obstacles
Rhex [4]	6	Tripod	7	0.55	1.04	• Passive dynamic stability • Improved dynamic stability and stair climbing with C-shaped legs
Edubot [21]	6	Tripod	~3.5	2.5	~5.83	• Passive dynamic stability • Equipped with variable stiffness legs
Sprawlita [44]	6	Tripod	0.27	0.7	4.5	• Passive dynamic stability • Unique compliant fixtured leg pistons to enable sprawling
Amphihex-I [8]	6	Tripod, paddle (swim)	14.2	0.55	0.65	• Passive dynamic stability • Convertible leg-fins to facilitate land and water-based travel
Spot [45]	4	Walk, stairs, amble, crawl, hop, jog	32.5	1.6	1.45	• Highly adaptable gaits • Self-righting ability • Highly integratable with OEM or third-party sensors or manipulators

Now, it has been established that legged robots are a relatively modern invention with many designs out there, however, this begs the question as to why: *what purpose do these wheel-less locomoting machines serve?* For this answer, what first must be made clear is the alternatives to legged robots, in particular: wheeled robots. The general consensus amongst literature now is that while wheels behave particularly well over prepared flat and solid surfaces, they are more limited when it comes to broken and unstable landscapes which cannot offer the continuous contact and support required by wheels [2, 39, 46]. To emphasise the magnitude of this issue, Raibert claims that "less than half of the Earth's landmass is accessible to wheeled and tracked vehicles" [39]. Beyond the terrestrial [2] and even inter-planetary exploration [7, 46] proposed in response to the limitations of wheeled robots, several specific applications have also been proposed or seen implementation, including: fire and rescue, bomb disposal, or other urban law enforcement activities in which common obstacles such as stairs need to be overcome [7], surveillance and inspection [3], and military operations [39].

2.2.3 Measures of Performance for Locomotion

Many novel legged locomotive robots have been designed and reported in recent years, which differ in many aspects beyond the use of leg-like limbs. A natural question one may wonder in response to this is, *how can they be compared?* It is common to see results published in literature for various identical locomotion experiments: on flat rigid ground [6, 21]; on various terrains such as challenging broken ground, grass, and small rocks [4, 6, 21, 39]; granular media such as wet or dry sand and dirt in some cases [8, 44, 47]; and over obstacles such as blocks and stairs [3, 7, 39]. However, these are in essence quite qualitative as they often don't provide a good means for comparison between different robot platforms, given tests may differ in how they are conducted, in part due to what purpose the platforms are designed to serve. With that said, average locomotion velocity, also referred to as average forwarding velocity v_{avg}, is a useful measure of performance [21].

To provide a more relevant benchmark for comparing robot platforms and similarly robot leg designs, the typical qualifying parameter is known as cost of transport (COT) or specific resistance [21, 48-50]. This cost function is a key

performance indicator for energy utilisation in locomotion, and is given by **Equation (2-1)**:

$$COT = \frac{P_{avg}}{m_{total} \cdot g \cdot v_{avg}}, \tag{2-1}$$

where P_{avg} is the average power consumed during locomotion, m_{total} is the total robot mass, and gravity g = 9.81 m/s^2. Given the numerator P_{avg} is the total input power and the denominator $m_{total} \cdot g \cdot v_{avg}$ is forwarding power, this function should be minimised for optimal performance. This is quite a versatile performance indicator as well, given it can be considered for robot platforms of all shapes and sizes, as well as leg designs mounted on test platforms [28] or rotating booms [48]. In some cases, mechanical cost of transport (MCOT) may otherwise be considered, eliminating consideration of additional electronic power consumption that is not directly involved in the locomotion [51].

2.2.4 Dynamic Modelling Approaches

In as early as 1989, a dynamic representation of legged locomotors was presented when Blickhan first proposed the spring loaded inverted pendulum (SLIP) model to mathematically describe such behaviour [12]. This model, illustrated in **Figure 2-3**, has been shown to accurately predict ground reaction forces and centre of mass (COM) motion for a variety of animals [52]. In comparison to a legged running body, m represents body mass, k represents effective vertical stiffness, and l_0 is the uncompressed length of the spring describing the leg. When in motion, the model characterises running in two distinct phases: a stance phase during ground contact, and a ballistic flight phase as the leg loses contact with the ground.

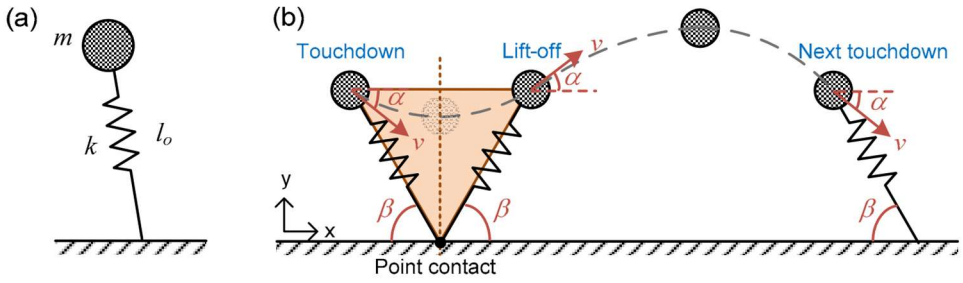

Figure 2-3 SLIP model (a) intrinsic parameters, and (b) dynamic behaviour [53].

From **Figure 2-3**, it can be seen that the model essentially describes a point mass which pivots about a contact point through a linear spring. After touchdown, this spring compresses and gains elastic potential energy as kinetic energy decreases. After the mass crosses the line of symmetry drawn about the contact point, the elastic potential then re-accelerates the body until the spring loses contact with the ground and there is lift-off, at which point the stance phase ends. Until the next touchdown, the body is then in flight phase, where the dynamics of the system differ as ballistic motion ensues [12].

Now, while the SLIP model has successfully been put to use in modelling legged robots of different shapes and sizes [54], not just biological creatures, many variants have been developed in recent years. Some examples of such include: the rolling-contact-SLIP (R-SLIP) model to characterise C-shaped legs [55]; active-SLIP (A-SLIP), which includes a linear actuator in series with a leg spring [54]; the torsional-damper-rolling-contact-SLIP (TDR-SLIP) model, incorporating parallel damping with the spring of the existing R-SLIP model [56]; and clock-torqued-SLIP (CT-SLIP), which maintains linear legs springs, however describes the behaviour of torque actuated robots such as RHex [33]. What should be made clear here is that while the base SLIP model can describe most legged dynamics reasonably well, if only for the sake of design, these models are essentially tailor made for different robot designs and leg geometries.

Regarding the usefulness of this dynamic modelling, beyond design assistance, it can offer useful ways to analyse robot stability. As many robot designs follow the concept of ‘template and anchor’, these simplified models, i.e. the templates, can be anchored to the dynamics of the robot platform [57]. That is, even for more complex geometry and more than one leg, the SLIP-like models behave much the same. This indicates that for stability and control, platform performance should mirror that of the models [55, 57]. Consequently, through simulation it is common to see what is called ‘steps-to-fall analysis’, which involves parameter variation and measurement of how many steps the simulated hopper can make before it enters a flight from which it cannot return to make another stride [55, 58]. Another approach that is quite common is ‘return-map analysis’ [55, 56, 59], in which one or more parameters are analysed following a single step to verify they do not deviate in a manner that would cause

instability. These ‘fixed points’ then indicate stability if after Jacobian transform they exist within the unit circle [55].

2. 3 From Passive to Variable Stiffness in Legged Locomotion

2.3.1 Passively Compliant Robot Legs

Alluded to in previous discussion, leg compliance was introduced to legged robots in attempt to mimic the biological flexibility in legs that humans and animals exhibit. If one first takes a moment to consider that without this compliance, legs would be purely rigid linkages connected to drive systems, it is easy to imagine compliant legs as springs placed in series with actuators. This concept in not unique to the field of legged robots, however, and falls under the topic of series elastic actuators (SEAs) [60]. While it may seem mundane, adding compliance in series with an actuator offers several benefits, one of which being simplifying force control problems to relatively simple position control problems. In addition to this, the low-pass-filter effect of springs added in series with an actuator can significantly reduce shock or impulse load transmissibility, this being a major benefit to legged locomotion for the sake of stability and energy efficiency. One drawback of this aspect however is that actuator motion must also succumb to filtering effects which could then increase energy consumption, leading to design trade-offs regarding stiffness [60]. Lastly, the energy storage capability of springs is a major benefit to legged locomotion as this is what results in high biological energy efficiency [14].

In response to the indicated benefits of biological modelling approaches to legged locomotion [12], this concept of series elasticity has been implemented in various legged robot platforms through leg design. Starting with Raibert’s compliant legged hoppers [2], several other platforms have seen adaptations of this, for example: the compliant four-bar and C-shaped legs of Rhex [7, 46], with an example illustrated in **Figure 2-4**; the rubber foot pads of improved Whegs designs [43]; the both compliant and damped legs of Tekken [6]; and the compliant fixtures of the actuating leg pistons of Sprawlita [44]. With this list of relatively strong performing legged robots having compliant legs, multiple of which represent improvements over previous rigid-legged iterations. This then begs the question, *what are the limitations?* As just mentioned, SEAs do offer improved energy efficiency, particularly in legged locomotion, however for efficient nature-like locomotion, leg stiffness should be

adaptive [9, 10, 37, 38]. It is for this reason, amongst the broader development of series elastic actuators, that has led to the now heated research area of variable stiffness actuators [61].

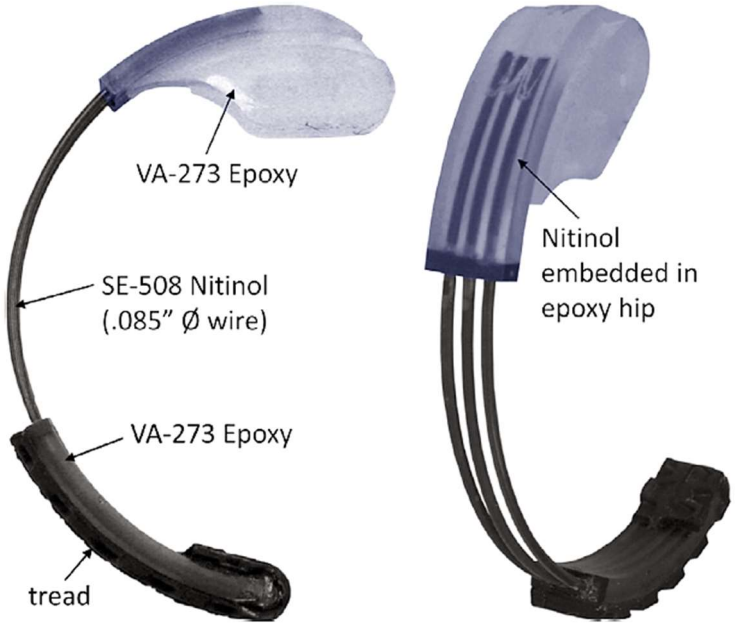

Figure 2-4 A passively compliant robot leg; adapted from [21].

2.3.2 Variable Stiffness Robot Legs

Variable stiffness actuators (VSAs), a subclass of variable impedance actuators (VIAs), are much the same as series elastic actuators, albeit with controllable stiffness. Similar to how SEAs consist of 'rigid' high-torque actuators such as servo motors with series spring elements, VSAs, such as variable stiffness robot legs, contain springs or spring mechanisms with tuneable stiffness through some means [19]. Considering the scope of such designs presented in literature, this may be achieved through one of three ways [61]: variation of spring preload, variation of transmission ratio across the spring, variation of the mechanical properties of the spring. Regarding the first option, variable stiffness is typically achieved in this mode using non-linear antagonistic springs, whereby adjusting preload will adjust spring stiffness. As for changing spring transmission ratio, this applies some mechanical transmission to increases or decreases spring displacement for a given input displacement, hence varying output stiffness. As for the third case, this can be achieved by altering the physical properties of the spring, e.g. length, or by variation of material properties, e.g. by applying and stimulating smart materials. An example of changing the physical properties is illustrated well in

Figure 2-5, whereby a geared slider shifts the pivot point and therefore varies the effective cantilever spring length in the C-shape structure [49]. Limited cases of smart materials being applied to legged robotics have been reported, with the use of MR elastomer by the author previously [62], shown in **Figure 2-6**, being a good example of this. The leg made use of the MR elastomer in a joint as a controllable torsional spring to provide variable leg stiffness.

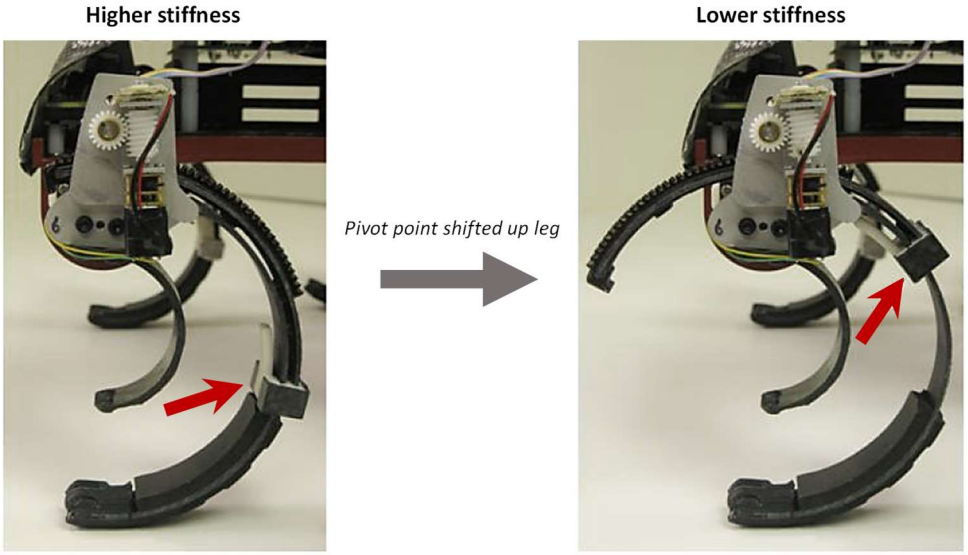

Figure 2-5 A variable stiffness robot leg; adapted from [49].

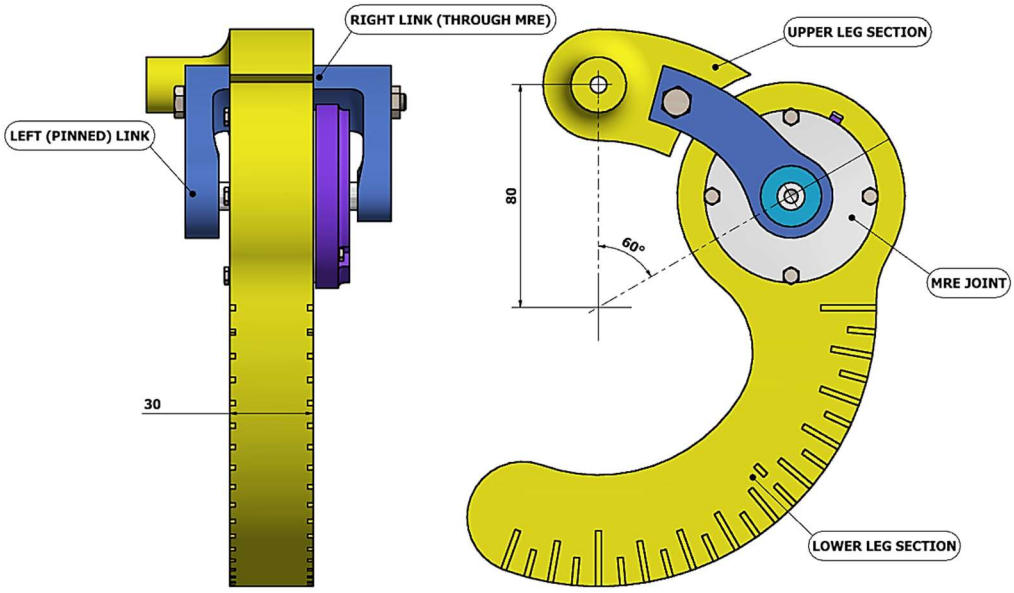

Figure 2-6 A variable stiffness robot leg featuring an MRE joint [62].

Of the various reported uses for VSAs, the following five categories capture the majority [61]: shock absorbing, stiffness variation under constant load, stiffness variation under constant position, cyclic movements, and explosive movements. For shock absorption, more-so in relation to dissipative VIAs, if a robot linkage was to experience a collision with a high inertia object, a rigid linkage could experience failure through compromised drive components. However, if the mechanism could go soft at the moment of collision, this could protect both the drive and the collided object, e.g. a person. As for using stiffness control to set constant load or position, these two differ in what parameter is fixed. For a constant load case, which may be desired for accurate fixing of force or torque as an end effector traces a contour, as the position traced out will change, varying stiffness can compensate to maintain constant loading. As for a fixed position, suppose an object collision occurs with the end effector of a VSA, to assist stability and minimise deflection, a stiff case would best facilitate this. On the other hand, if decoupling of the drive and output was desired, say in response to a disturbance, a soft case would be best suited. For cyclic or oscillatory motion, the energy storage in potential strain energy of springs can serve to minimise energy consumed in accelerating and decelerating end effectors. Where variable stiffness adds to this SEA concept is in the ability to tune the system resonance to match the current working scenario. Lastly, explosive movement may be realised by pre-loading elastic elements to increase end effector output velocity beyond what could be achieved through actuation alone [19, 61].

This leads us to the question, *to what extent has this concept seen implantation in legged robots?* As discussed, on the basis of biological locomotors which modulate their leg stiffness while running, it has been alluded to that this should similarly benefit legged robots [10]. More recently, few designs with such stiffness variation have been reported on. Such designs are included in **Table 2-2**, which are compared on the basis of design features, special traits, and experimental demonstration of the supposed biological benefits to locomotion. What becomes obvious here is that amongst the surveyed leg designs, there is limited contribution to the investigation of the supposed biological benefits owed to variable stiffness in legs. This leaves a large gap in the existing literature of this field to be filled.

Table 2-2 Design and performance comparison of variable stiffness robot legs.

Leg Design	Mass (kg)	Stiffness Range (N/mm)	VSA Type	Special Traits	Limitations	Biological Inspired Tests
C-shaped slider [21]	0.09	1.15 – 2.34	• Transmission variation	• Self-locking worm gear stiffness adjustment mechanism	• High tuning time for stiffness (order of seconds)	• Adjusting leg stiffness for different terrain materials
AMSAC [23]	4	3.00 – 18.6	• Spring preload variation	• Logarithmic gears to non-linearise springs to enable variable stiffness	• N/A	• N/A
L-MESTRAN [48]	1	~0 – ∞	• Transmission variation	• Self-locking worm gear stiffness adjustment mechanism	• High tuning time for stiffness (order of seconds) • Near infinite stiffness range	• N/A
Rotating Spiral Foot [63]	< 0.75	1.15 – 8.60	• Transmission variation	• Rapid tuning time • Imbedded deflection sensing in leg	• N/A	• Adapting stiffness in transitions across different ground stiffnesses
C-shaped leg with MRE joint [62]	0.91	0.43 – 0.63	• Mechanical spring property variation	• Stiffening and softening about base value • Rapid tuning time (millisecond scale)	• Small deflection level before yield of MRE	• N/A

2. 4 Magnetorheological Materials

2.4.1 Material Properties and Working Mechanism

Magnetorheological (MR) materials are a smart kind of material which exhibit altered rheological properties when in proximity with a magnetic field. This behaviour occurs rapidly, in the order of milliseconds [64]. Since the discovery of the MR effect by Rabinow in 1948 [65], there have developed two main classes: MR fluids (MRFs), and MR elastomers (MREs). With a similar MR working principle, the behaviour of the materials differs based on the operation in the post-yield and pre-yield regimes, respectively [66, 67]. It is for this reason that MRF is typically well-suited to variable damping applications, and MRE sees more use where variable stiffness is desired. That being said, however, some innovative designs exist which utilise MRF to facilitate

stiffness variation rather than mere damping variation [29, 30, 32], discussed further in **Section 2.4.3**.

Common to the different classes of MR materials is the suspension of micro-scale ferromagnetic particles in a non-magnetic host material, wherein some additives may be present for a variety of purposes. The magnetisable particles used for this typically range in size from 3 to 5 microns [68], and are often carbonyl iron particles [69]. When a magnetic field is applied to the MR material, these iron particles tend to align to the magnetic field lines [68]. In doing so, the applied pressure or stress driving relative motion about the material will increase. This is illustrated for MRF loaded in shear mode in **Figure 2-7**. For MRE, studies have shown that to achieve the optimal MR effect, the volume fraction of these particles should be around 27% [70, 71], whereas MRF's usually range in volume fractions of about 25 to 50% [72, 73]. Where MRFs and MREs then differ is in the host material selected, i.e. fluid or elastomer. Conventional host matrix materials for MRE presented in literature will usually be based on synthetic rubber, typically silicone, or natural rubber (cis-polyisoprene) [74]. These have both been demonstrated to produce MRE with an appreciable MR effect [71, 75], in the order of about a 40% stiffness increase [75]. On the other hand, MRFs are usually hydrocarbon based and an increase in damping for a typical MR damper can easily reach 200% [27].

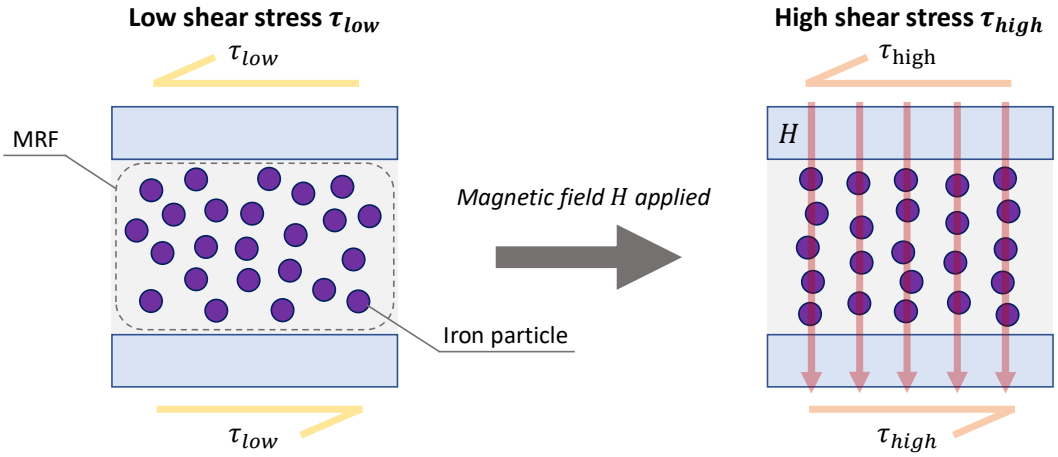

Figure 2-7 Alignment of iron particles in MRF used in shear mode due to magnetic field.

2.4.2 System Dynamic Models for MR Fluid

Now focusing on MRF, given it is the material that will be used in this thesis, whether employed in linear MR dampers or rotary MR dampers, its dynamic behaviour can be modelled similarly. Featured in **Figure 2-8** are three common models applied to MRF: Bingham plastic, Herschel-Bulkley, and Bouc-Wen. The first two listed are both quasi-static models, which means implementation will involve switching between discrete states which represent the pre- and post-yield states of the MRF. Starting with the simplest and most-widely applied in literature [76], the Bingham plastic model considers a field-dependent Coulomb friction component $T_\tau(H)$ and viscous damping component $c_0\dot{\psi}$. Where this model may become unsuitable is for exceptionally high shear-rate applications, given it does not account for shear thinning of the MRF at such shear-rates [77]. On the other hand, the Herschel-Bulkley model is similar to the Bingham plastic model, although it can account for either shear thickening or shear thinning [78]. That is, while this quasi-static model still includes a Coulomb friction component, the viscous damping $c_n\dot{\psi}$ is scaled by the flow behaviour index n. For shear thinning fluids, $n < 1$, unlike the case in this model if $n = 1$, which is effectively the Bingham plastic model. Lastly, the Bouc-Wen model may be used for dynamic modelling, which has seen frequent use in literature [76]. The model was developed as a means of capturing the hysteretic or 'memory-dependent' behaviour of MRF during cycled loading. This is, again, in contrast to the discrete states which are used to describe the MRF in both the Bingham plastic and Herschel-Bulkley models. However, due to its relative complexity and numerous parameters, the quasi-static models are often favoured, typically providing adequate modelling accuracy.

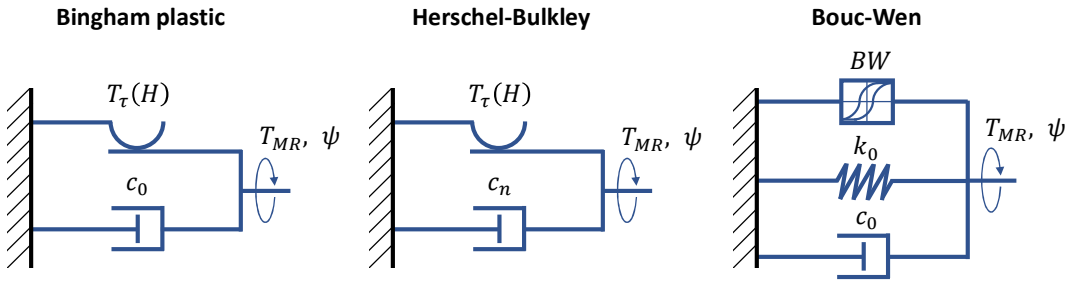

Figure 2-8 Common dynamic models for rotary MR dampers.

2.4.3 Existing Uses and Applications of MR Fluid

Regarding typical uses, MR materials have seen widespread use in the fields of noise suppression, dynamic control, and vibration attenuation [74, 79]. While active forcing elements or otherwise passive structures have more extensive and common use in these areas, there is a compromise between the versatility of active elements and the often more reliable, energy efficient passive alternatives. For this reason, semi-active systems which feature materials with controllable mechanical properties, such as MRF, may be suitable alternatives. This reasoning is often cited as an important consideration leading to the now common application of linear MR dampers and shock absorbers, often used in vehicle suspension [27, 29, 32]. Beyond linear dampers, rotary MR dampers are even more ubiquitous with extensive research conducted [76].

Of particular interest to this work, in 2014, Sun et al. first reported the idea of using MRF for variable stiffness, controlling an air spring with an MR valve [31]. In 2015, Sun et al. extended the concept, developing variable stiffness and variable damping linear shock absorbers using linear MR dampers [29, 32]. With one such device illustrated in **Figure 2-9**, the variable stiffness part of the device is formed by the mechanical springs and the outer damping cylinder. While spring 2 will always experience displacement with an external displacement applied to the absorber, spring 1 acts in parallel with the outer damper, moving with it. If the outer damper becomes locked, spring 1 is unable to compress and therefore can no longer contribute to the overall stiffness of the device. Since both springs act in series, device stiffness will be lower if the outer damper is not energised and will be higher if damping force is increased. When fully locked, the device stiffness will simply be that of spring 2.

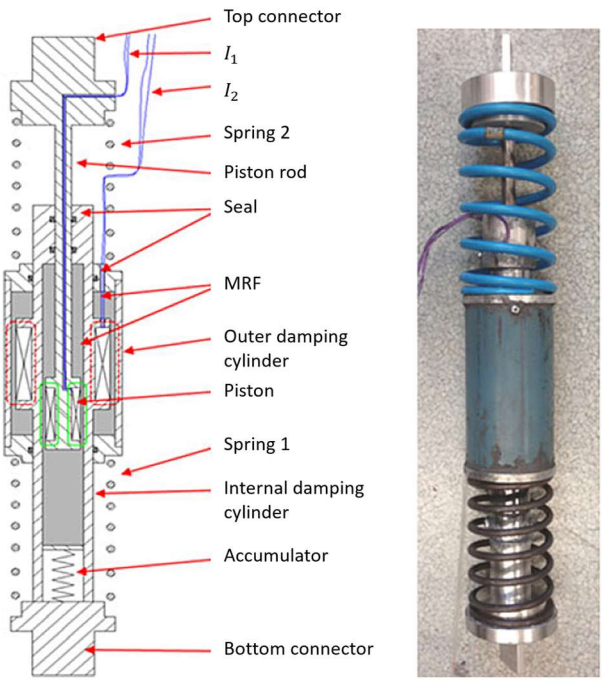

Figure 2-9 Variable stiffness and variable damping MR shock absorber [32].

Since the inception of this thesis, few researchers have investigated the potential for variable stiffness or a combination of variable stiffness and variable damping in a rotational sense rather than the linear arrangement of the shock absorber by Sun et al. in [29, 32]. Subsequent to the development of the MRVSAL-I presented in **Chapter 3**, which makes use of rotary-MR-damper-based variable stiffness, the author of this work employed an identical arrangement of a rotary MR damper in series with a torsional spring to produce a variable resonance pendulum tuned mass damper in [80]. Coupled through a planetary gearbox, the passive off-state stiffness of the device, however, was contributed by a pendulum mass, rather than a secondary relatively soft spring. The author also collaborated on the development of a direct rotational-analogy of the linear variable stiffness and variable damping shock absorber of Sun et al. in [32], contributing to the work of Deng et al. in [81]. Another work, this being by Dong et al. [82], aimed to achieve similar behaviour with an identical variable stiffness and variable damping joint. More recently, in 2021, Sun et al. developed a rotary variable stiffness device for vehicle seat suspension which employed a rotary MR damper with a gear reduction placed in series with a torsional spring in [83]. In this scenario, the gearbox served to increase damper torque to satisfy the design requirements. Given the limited number of publications based on this technology, there is sufficient room for this thesis to contribute to this body of knowledge.

Recently, MR materials have also made their debut in legged robotics, starting with a linear MRF shock absorber in the foot of a robot leg presented by Kostamo et al. in 2013 [84]. Since then, an MR-damper-based leg that is adaptively tuneable to suit different running conditions was presented by Jiang et al. in 2016 [28]. As mentioned in **Section 2.3.2**, a novel design placing an MRE spring into a C-shaped leg joint was presented by the author previously, in 2017, with a plus-or-minus stiffness variation of 48% [62]. What is still lacking in this area is the implementation of MRF-based variable stiffness. This exciting innovation side-steps the typically limited stiffness range and yielding-failure of MREs by using MRF to engage or disengage mechanical springs. In such an arrangement, what would normally be a current-controllable damping force or torque, then becomes a controllable stiffness by variably clutching mechanical springs.

2.4.4 Advantages and Limitations of MR Fluid in Legged Robotics

With reference to the idea of implementing MR fluid in legged robots to enable variable stiffness, it should be discussed what are some of the benefits that may be achieved, as well as some of the challenges that should be considered. **Table 2-3** includes such discussion, also outlining potential solutions to the challenges brought forward.

2. 5 Chapter Summary

By this stage, three major aspects should be clear:

(1) Legged robots behave much the same as their biological counterparts. This means the biological understanding that variable stiffness contributes to locomotive performance also can be applied to legged robots.

(2) In the field of legged robot locomotion, variable stiffness is quite a new idea with limited biologically inspired experimental work reported on. However, the outlook for this research is quite good, indicated by the few studies performed on variable stiffness leg designs in capturing the biological benefits of variable stiffness.

(3) Magnetorheological materials offer controllable mechanical properties via simple control of electromagnet coil current. For a compound structure utilising mechanical springs and a rotary MR damper, robust variable stiffness can be achieved by using MRF, overcoming the limitations of MRE. As such, this may now be applied in robot legs to improve locomotive performance.

Table 2-3 Advantages and challenges faced by MRF for variable stiffness robot legs.

Aspect	Advantages	Challenges	Potential Solutions to Challenges
Control	• Simple, via application of magnetic field using a solenoid	• Non-linear response; hysteretic behaviour	• Closed-loop control for hysteresis compensation [85]
Response time	• Rapid response, in the order of milliseconds [64]	• Low coil wire diameter can cause increased response time	• Balance wire gauge with number of coil-turns through optimisation
Magnetic circuit	• Provides flexibility in damper design, particularly geometry and coil placement	• Due to the requirement of a high permeability steel structure, MR devices are typically quite massive	• Optimisation [76] and mechanical amplification, e.g. via gears
Energy dissipation	• It has been shown that damping alone can improve locomotive performance [28], and as such some energy dissipation may be of benefit in running	• Current mechanisms using mechanical springs and MRF tend to have high damping between extremes of control range	• Minimise time spent between extremes of control range during locomotion
Stiffness range	• For a single spring place in series with an MR damper, a near infinite stiffness range can be realised	• Given zero stiffness is not often desired as the bottom extremity, a base stiffness can be set by a primary spring; however, this limits the effective range achievable to either the primary spring or the sum of the two (if in parallel)	• Optimise spring selection through design; develop damper to produce sufficient torque for given coupled spring stiffness
Energy consumption	• Legs still function with passive compliance when not powered	• Given MR dampers are controlled using electric current, setting a high stiffness value means using power	• Incorporate permanent magnets to set desired base stiffness to minimise use of coil [86]

3 A ROBOT LEG WITH HIGH STIFFNESS ADJUSTABILITY FOR ENHANCING LOCOMOTIVE PERFORMANCE

3. 1 Introduction

Much like in biological species [9, 10], an important feature of variable stiffness robot legs is the rate at which they can be tuned to reach a desired stiffness. While variable stiffness mechanisms have been implemented in robot leg designs before, designs like that of Galloway et al. [21] or Vu et al. [48] feature worm-gear driven mechanisms which incur long stiffness tuning times. As this prevents adaptive tuning, i.e. stiffness adjustment between or during steps, this may limit the performance of the design and the ability to reject disturbances such as obstacles or transitions in terrains. Amongst other aspects, this tuning time requirement shows exciting new prospects may exist for rapid-response MR materials in legged robot locomotion.

Typically, MRF is used in a post-yield regime in which constant yielding leads the MR effect to cause greater energy dissipation, i.e. increased damping [64, 87]. While designs utilising MRF for as a variable stiffness element in the (low-strain) pre-yield regime are possible [88, 89], this is typically less practical than using MRE which provides variable stiffness under higher strain amplitudes. This point notwithstanding,

both materials could enable rapid leg stiffness adjustment in the order of milliseconds [64] through innovative design, enabling semi-active control with minimal tuning time. With that being said, however, a practical issue in applying MRE to robot legs is the stroke limitation it possesses [55]. This tendency of the material to yield into failure readily limits the usefulness of it in this context. On the other hand, MRF has no such limitation, being that it is a fluid and can yield continuously without consequence.

This work utilises a variable stiffness MR damper mechanism similar to the linear shock absorber presented in [32], albeit with a rotary design. With a torque-actuated drive, this MRF-based variable stiffness actuator leg has been termed the MRVSAL-I. Like the author's previously designed MRE leg, this design also uses a literal R-SLIP [55] morphology, with the joint mechanism on the arc of the C-shaped leg near the hip, replacing the torsional spring of the model. Through control of the electromagnetic coils of the rotary MR damper in this dual-spring design, a secondary torsional spring is engaged, providing simple current control of leg stiffness. Following mathematical modelling of the leg, it is characterised through linear compression testing, followed by rudimentary locomotion experiments using a constrained bipedal robot platform.

3. 2 Design and Working Mechanism of the MRVSAL-I

3.2.1 Leg Structure

Illustrated in **Figure 3-1** is the R-SLIP-based design concept for the MRVSAL-I, suited to a torque-actuated robot platform. Apparent in this figure is the C-shaped leg structure, including the variable stiffness joint mechanism at a position 60° from the hip on the arc of the 60 mm leg radius, in a position theorised to provide optimal stability for such legs [53]. The upper leg segment is coupled to the lower through an always-active 'soft' spring of stiffness 1560 N·mm/rad, pre-tensioned by 90° rotation. A rotary MR damper housed in the lower leg segment has its output shaft linked to the upper leg segment through a thereby controllable 'stiff' secondary spring of stiffness 4060 N·mm/rad. In the extreme 'free-spinning' case for the MR damper, that is, when damping is low due to zero coil current, the leg will have a 'soft' single spring stiffness. At the other extreme under a large input current, the high damping torque will lock the damper and engaging the secondary spring, giving a stiffer parallel arrangement.

Other features include a locking clamp, constraining the MR damper assembly to the lower leg segment, also setting the zero-position of the upper leg segment. Additionally, a silicone rubber foot pad is used to improve ground friction as the leg segments shown are 3D printed in high density ABS plastic, made using an UP Box FDM 3D printer. To make the design more robust however, other non-metal parts of the assembly are printed in high density nylon, printed on the Markforged Mark Two FDM 3D printer. All inclusive, the leg has a total weight of 657 g.

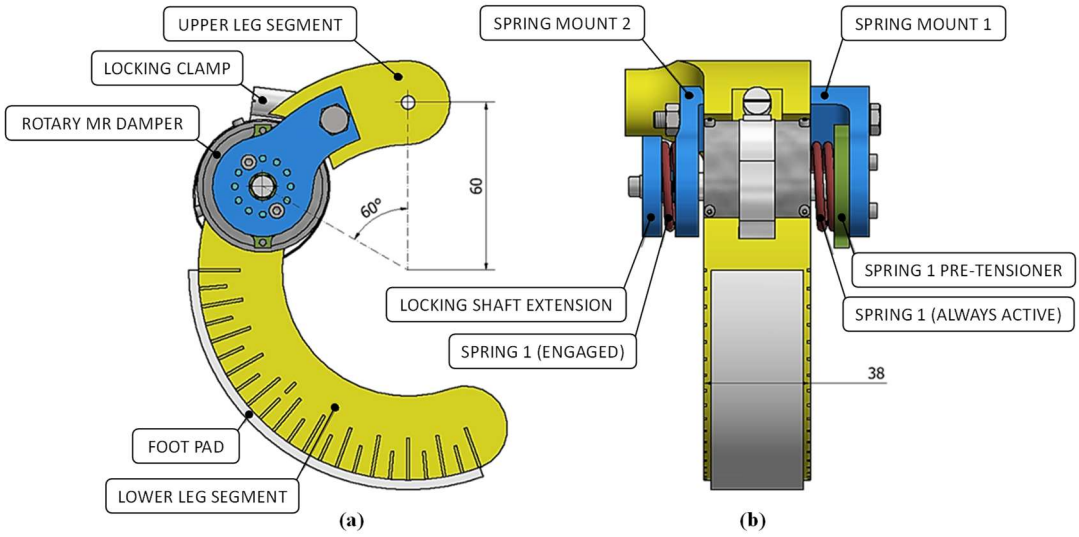

Figure 3-1 MRVSAL-I CAD model (a) side view, and (b) rear view (dims in mm).

Regarding some of the equations describing the static forces generated in the leg, the R-SLIP nature of the design allows the equations presented in [55] to be applied. With the parameters of the R-SLIP model outlined in **Figure 3-2**, taking guidance from [62], the following relationship can be used:

$$k_l = \frac{F_l}{(l_0 - l_b)} \quad \text{[N/m]}, \tag{3-1}$$

where k_l is vertical leg stiffness, F_l is the force exerted on the ground by the leg, hereafter referred to as the 'leg force', $l_0 = 2r$ is the free length of the virtual linear spring between the hip (loading point of the upper leg segment) and ground contact point, and l_b is the compressed spring length. To determine l_b for a given contact angle, it may be found using:

$$l_b = \sqrt{l_j^2 + l_a^2 - 2 l_j l_a \cos(\gamma)} \quad \text{[m]}, \tag{3-2}$$

where l_j is the length of the rigid link between the torsional joint and the hip, the chord drawn from the joint to the contact point l_a is given by:

$$l_a = \sqrt{l_0^2 - l_j^2} \quad [\text{m}], \tag{3-3}$$

and γ is the angle subtended by the hip and the contact point, given by:

$$\gamma = \gamma_0 - \psi_2 = \frac{\pi}{2} - \psi_2 \quad [\text{rad}]. \tag{3-4}$$

The initial angle formed γ_0 is equal to $\pi/2$ for a 0° contact angle, and ψ_2 is the joint deflection angle which loads the torsional joint.

More applicable to linear force testing, the deflection angle of the joint can also be described in terms of vertical leg displacement Δy_l:

$$\psi = \gamma_0 - \frac{\xi}{2} - \sin^{-1}\left(\frac{\Delta y_l}{l_a} + \sin\left(\gamma_0 - \frac{\xi}{2}\right)\right) \quad [\text{rad}], \tag{3-5}$$

where ξ is the position angle of the joint, spanning counter-clockwise from the hip.

As the key result of these formulae, the effective torsional stiffness of the joint can be transposed into a linear leg stiffness through:

$$k_l = \frac{l_b \cdot \left(\frac{\pi}{2} - \gamma\right)}{(l_0 - l_b) \cdot l_j l_a \sin(\gamma)} \times k_t \quad [\text{N/m}], \tag{3-6}$$

where k_t is the effective torsional stiffness of the joint.

From the result of **Equation (3-6)**, with platform parameters known, a leg stiffness range based on the mice-to-horse locomotion scaling work of Heglund et al. in [13] may be selected. As is now typical of similar design approaches, in this work a 10% leg compression level [55, 59] was considered. Based on the 5.9 kg bipedal torque actuated platform employed in this study, presented later in **Section 3.4**, and additional 1.3 kg dual-leg mass, a linear stiffness range of 0.5 N/mm to 2.0 N/mm was chosen to suit a 7.2 kg bipedal robot mass.

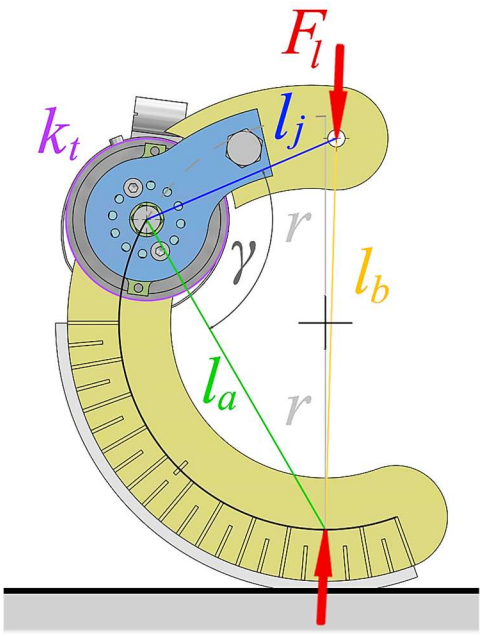

Figure 3-2 R-SLIP static model parameters.

3.2.2 Design of the Rotary MR Damper

Illustrated through the CAD model of **Figure 3-3** is the rotary MR damper which enables the control input to this leg and the consequent stiffness variation. With design parameters listed in **Table 3-1**, as shown, the damper is quite compact with a maximum diameter of 47 mm and a body length of 38 mm, with shaft extensions giving a maximum length of 64 mm. The high-density MRF (MRF-140CG, produced by LORD Corp.) in the joint surrounds a rotor adjacent to two electromagnetic solenoid coils wired in series. These coils of 0.5 mm diameter wire are 120 turns each provide magnetic flux through the magnetic circuit made of low carbon steel when current is supplied. The MRF in the 0.5 mm wide radial gaps inside and outside of the rotor drum is then subject to an increased yield stress and viscosity, increasing the braking torque between the aluminium shaft and outer body of the damper. Regarding the behaviour of the 'T-shaped' drum, this design essentially acts as a normal drum-type damper, however with a larger active area of MRF and less unnecessary geometry, reducing weight. Furthermore, this design trades the requirement of the large radial area needed in disc brakes for a more manageable increase in axial length of the damper, more suitable for compact robot legs. The total weight per damper is approximately 390 g, subject to subtle variation between prototypes.

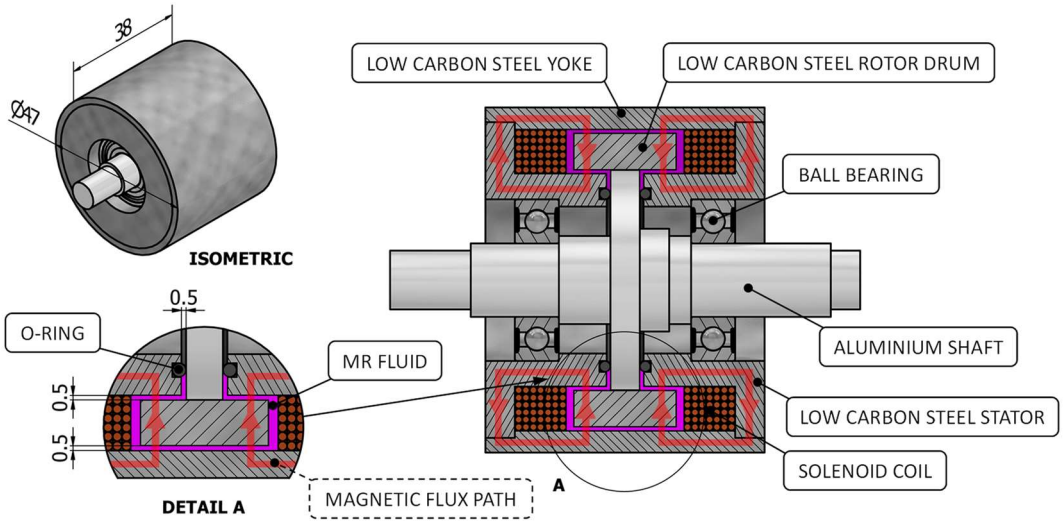

Figure 3-3 Compact rotary MR damper (dims in mm).

As for the considerations that went into the design of the damper, a 2D axisymmetric field study was developed in FEM software COMSOL Multiphysics ver. 5.1. Within this simulation, the MRF was defined by the B-H curve LORD Corp. provided in the material data sheet for MRF-140CG [90], and the steel of the magnetic circuit was set to possess a relative permeability μ_r of 300. This relative permeability is reasonable to use for the low level of current supplied, although the accuracy of the result could be improved with a B-H curve for a known grade of steel. All other materials as detailed in **Figure 3-3** were defined by the built-in properties of the software package. Through iteration, the geometry of the joint was revised to meet an optimal trade-off between weight and magnetic flux penetrating the MRF. Plotted in **Figure 3-4(a)** is the simulated mean flux through the inner and outer gaps of the damper under the application of a 0 to 1 A current range, with these regions highlighted in the model shown in **Figure 3-4(b)**. Within this result, it is seen that under a 1 A current, the maximum flux through the MRF achieved is 0.54 T in the inner gap, along with 0.28 T in the outer gap. Regarding the seemingly large deviation amongst these flux densities of the two gaps, this is primarily due to the inverse proportionality between flux density and sectional area, with the area increasing radially outwards.

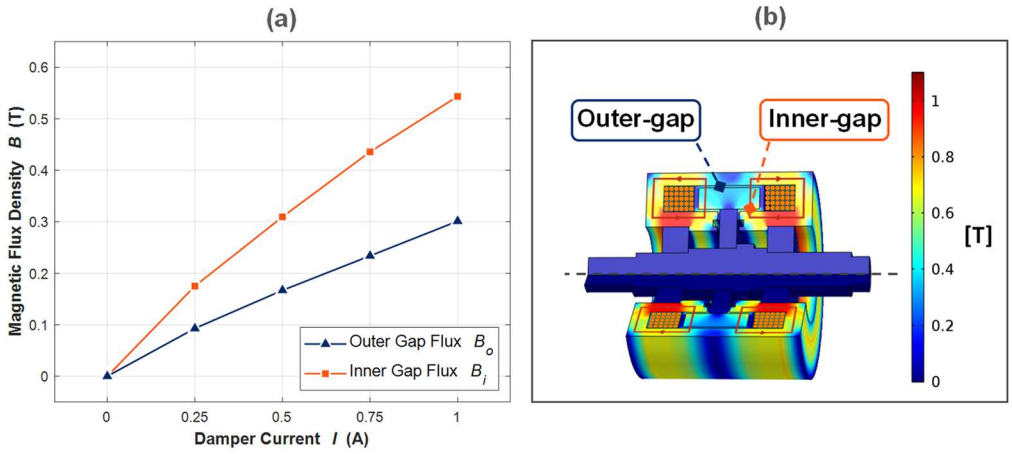

Figure 3-4 Magnetic field FEM analysis (a) mean flux through MRF, (b) joint model.

3.2.3 Working Mechanism

As previously mentioned, the leg design of this work utilises two springs, the softer of the two with a relatively low torsional stiffness of k_{soft} = 1560 N·mm/rad, and the other with a higher stiffness k_{stiff} = 4060 N·mm/rad. Described in the diagram of this mechanism, **Figure 3-5**, while the softer spring represented by k_{soft} always couples the upper and lower leg segments, the stiffer spring k_{stiff} acts through the MR damper, represented by the Bingham plastic model in the figure. It can be inferred that the relative angular displacement about the damper, i.e. $(\psi_2 - \psi_1)$, will govern whether the output torque T_{VS} is produced primarily by k_{soft}, or comes from the parallel arrangement with k_{stiff} and the MR damper in series. If it is assumed that off-state damper torque and other sources of energy loss in the mechanism are negligible, the result simplifies and two extremes may be considered: if no current is input to the MR damper, $\Delta\psi_1 = 0$, and the joint stiffness will be equal to k_{soft}; if a large current is supplied to the damper, causing the internal shaft to lock to the outer body, then $\Delta\psi_1 = \Delta\psi_2$ and the joint stiffness is the sum $(k_{soft} + k_{stiff})$.

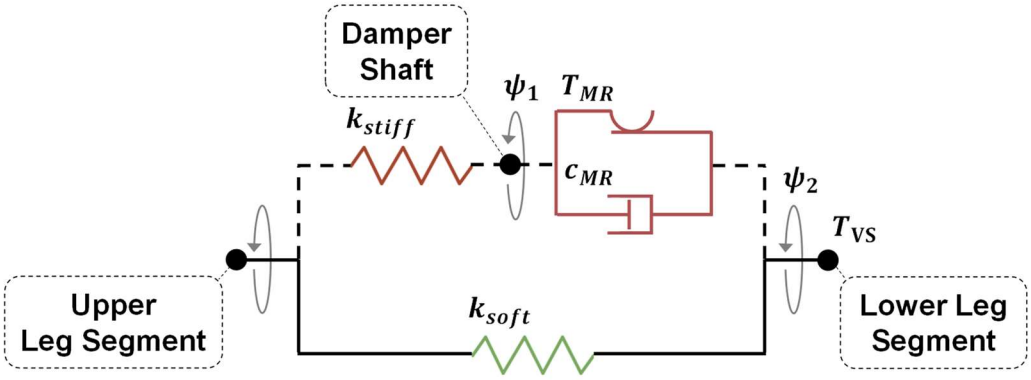

Figure 3-5 Variable stiffness rotary MR damper mechanism.

To formalise the behaviour of the mechanism, describing the leg force in terms of displacement and input current to the damper, a theoretical analysis on its force displacement relationship has been conducted in conjunction with modification of previously provided R-SLIP equations. From the FEM result provided in **Figure 3-4(a)**, the mean flux through the inner and outer gaps of the MR damper, B_i and B_o respectively, can be approximated by the following quadratic equations within a 0 A to 1 A input current I range, starting with the inner flux:

$$B_i(I) = -0.0691 \cdot I^2 + 0.5950 \cdot I \quad [\text{T}], \tag{3-7}$$

and then the outer flux:

$$B_o(I) = -0.0358 \cdot I^2 + 0.3116 \cdot I \quad [\text{T}]. \tag{3-8}$$

As provided by LORD Corp., the B-H and shear yield stress relationships for the MRF used (MRF-140CG) can be found in [90]. Through curve fitting, the magnetic field strength H can be described accurately in terms of the flux density B by the following cubic:

$$H(B) = 60.7433 \cdot B^3 + 105.8471 \cdot B^2 + 33.5748 \cdot B \ \ [\text{kA/m}]. \tag{3-9}$$

To then relate the magnetic field strength to the yield behaviour of the material, the shear yield stress τ_y can be expressed in terms of H with a quadratic fit:

$$\tau_y(H) = -1.3835 \cdot H^2 + 567.2490 \cdot H + 603.5291 \quad [\text{Pa}]. \tag{3-10}$$

Lastly, rotary MR damper design equations can be considered to convert this MRF yield stress into a static braking torque, modifying the drum-type brake equations provided in [76]. Considering a Bingham plastic model, the braking torque of the

damper is the sum of two components, a Coulomb friction (pre-yield induced) torque T_τ, and a viscous rate-dependent damping T_η, i.e. $T_{MR} = T_\tau + T_\eta$. Considering the angular velocity of the damper as zero, since we are interested in the pre-yield torque of the damper, we will also assume T_η to be relatively small in the post-yield state and may neglect the viscous-damping term. We may describe damper torque simply as the yield torque T_{MR} through the following:

$$T_{MR}(\tau_y) = 2\pi\left(\tau_{y,i}(H_i) \cdot w_i \cdot r_i^2 + \tau_{y,o}(H_o) \cdot w_o \cdot r_o^2\right) \quad [\mathrm{N \cdot m}], \quad (3\text{-}11)$$

where w and r are the axial lengths and radii, respectively, of the inner and outer drum areas of the rotary damper, listed in **Table 3-1** along with other design parameters. Also, note the two yield stresses of this equation are different; given the MRF flux is described by two equations, **Equation (3-7)** and **(3-8)**, two results must be obtained for **Equation (3-9)** and consequently **Equation (3-10)**. Then employing **Equation (3-7)** through to **(3-11)**, the yield torque of the MR damper can be estimated as a function of input current to the electromagnetic coils. It should also be noted that this torque model only considers unidirectional loading as the C-shaped nature of the leg results in ground contact only during the compression phase when locomoting. The leg is subsequently returned to its initial state in the aerial phase, aided by the 'always active' soft spring, during which the typical hysteretic behaviour of MRF occurs. Consequently, a simplified torque-displacement, and then force-displacement model for the leg can be established for the MRVSAL-I.

Table 3-1 Rotary MR damper design parameters.

Description	Variable (Unit)	Value
Maximum overall length	(mm)	64
Maximum overall diameter	(mm)	47
Total weight	(g)	390
Number of turns per coil	-	120
Coil wire diameter	(mm)	0.5
MRF gap thickness	(mm)	0.5
Inner rotor axial length	w_i (mm)	10
Outer rotor axial length	w_o (mm)	14
Inner rotor radius	r_i (mm)	15
Outer rotor radius	r_o (mm)	20

Now, with a means of determining the yield torque of the damper, conditions for its behaviour can be set based on whether the MRF has yielded or not, determining if the entire mechanism is in the stiff-state or soft-state. As it is the force relationship of the leg while locomoting we are interested in, the torque output T_{VS} of the mechanism described in **Figure 3-5** can be transposed into a leg force F_l using **Equation (3-1)** through **(3-6)**, giving the combined result:

$$F_l = \lambda \cdot T_{VS} \quad [\mathrm{N}], \tag{3-12}$$

where λ can be considered as the reciprocal of the moment arm through which the force rotates the joint mechanism housed in the leg. This can be determined from:

$$\lambda = \frac{\sqrt{l_j^2 + l_a^2 - 2 l_j l_a \cos(\gamma_0 - \psi_2)}}{l_j l_a \sin(\gamma_0 - \psi_2)} \quad [\mathrm{m}^{-1}], \tag{3-13}$$

again, recalling ψ_2 is the angular deflection of the mechanism which, as per **Equation (3-5)**, is a function of leg geometry and vertical displacement.

With a relationship describing the leg force in terms of vertical deflection and input current, the following conditions may be used:

IF: $k_{stiff} \cdot \psi_2 < T_{MR}$

$$\Delta\psi_1 = \Delta\psi_2, \tag{3-14}$$

and

$$F_l = \lambda \cdot T_{VS} = \lambda \cdot \left[\left(k_{soft} + k_{stiff}\right) \cdot \psi_2\right]. \tag{3-15}$$

ELSE IF: $k_{stiff} \cdot \psi_2 \geq T_{MR}$

$$\Delta\psi_1 = 0, \tag{3-16}$$

and

$$F_l = \lambda \cdot T_{VS} = \lambda \cdot \left[k_{soft} \cdot \psi_2\right]. \tag{3-17}$$

Following **Equation (3-14)** to **(3-17)**, the force displacement relationships under different currents can then be calculated, as illustrated as the model data in **Figure 3-7**.

3. 3 Leg Characterisation

The experimental test setup for the static force and stiffness characterisation of the leg prototype is shown in **Figure 3-6**. In this arrangement, rather than a robot

platform, the leg is coupled to the upper clamp of an MTS Landmark hydraulic test system (Load Frame Model: 370.02, MTS Systems Corp.), with the lower segment of the leg (rubber foot pad removed) free to slip on a low friction base plate affixed to a force transducer. In a similar fashion to the procedure followed in [62], through linear ramping of the servo-hydraulic actuator of the top clamp, the system supplied uniaxial loading to the vertically restrained leg set to a 0° initial contact angle. The time, force, and displacement data is simultaneously logged to a computer via the built-in data acquisition (DAQ) system. To provide current to the coils of the MR damper inside the leg, a DC power supply (CPX400A, Aim-TTi Ltd.) was used.

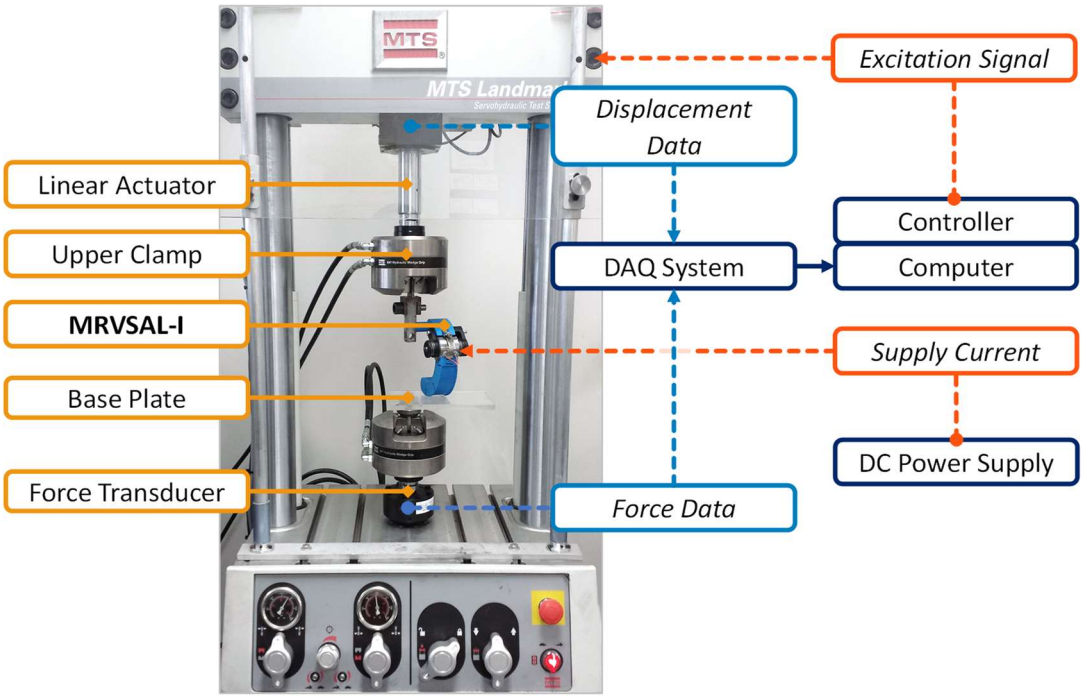

Figure 3-6 Force characterisation experimental setup.

Plotted in **Figure 3-7** is the experimental test result along with the theoretical calculation result, whereby the leg undergoes deflection with an 8 mm vertical displacement with currents varied from 0 to 1 A between tests. As can be seen, under zero input current, the leg possesses a constant soft stiffness across the displacement range tested, with a peak force of 4.05 N. As current is increased, shown in the 0.25 A and 0.50 A test runs the leg is stiffer at lower displacement levels, and at some point, i.e. the damper's yield point, the slope decreases, again giving the soft stiffness state. As the turning-point at which the damper yields gradually increases with joint input current, it can be seen in the 1.00 A curve that the damper no longer yields under a displacement level of 8 mm, giving a peak force of 14.1 N, representing an increase of

249% from 0 A. Providing validation for the theoretical calculation of the working mechanism, this behaviour is consistent with the description of the two stiffness states the leg provides, with conditions depending on the yield torque and angular displacement of the MR damper. Regarding the parameters used, some have already been incorporated into the equations of the model and are therefore implicit, however some others are included for reference in **Table 3-2**.

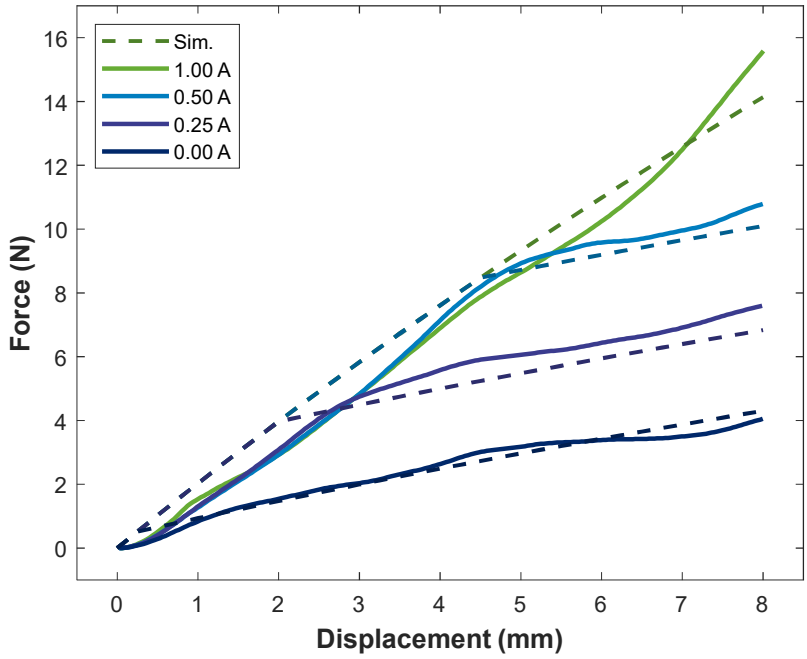

Figure 3-7 Experimentally measured and model calculated leg force under varied current.

Table 3-2 MRVSAL-I force-model parameters.

Parameter	Value
l_j	60 mm
l_a	103.9 mm
ξ	π/3 rad
γ_0	π/2 rad
k_{soft}	1560 N·mm/rad
k_{stiff}	4060 N·mm/rad

Focusing more specifically on the effective leg stiffness of the leg as tested, this is included in **Figure 3-8** for the 0 to 1 A range tested, with numerical values

provided in **Table 3-3**. As can be seen, the leg stiffness in the softest state under zero input current is 0.507 N/mm, consistent with the low-end of the design stiffness level (0.50 N/mm). At the maximum, 1 A current level, with subtle saturation evident, the stiffness increased to 1.81 N/mm, just shy of the 2.00 N/mm design target, which is reasonable. The result presented here represents a maximum stiffness increase of 257%, which should allow the leg to adequately alter the dynamic performance of a robot platform for a modest range of test conditions.

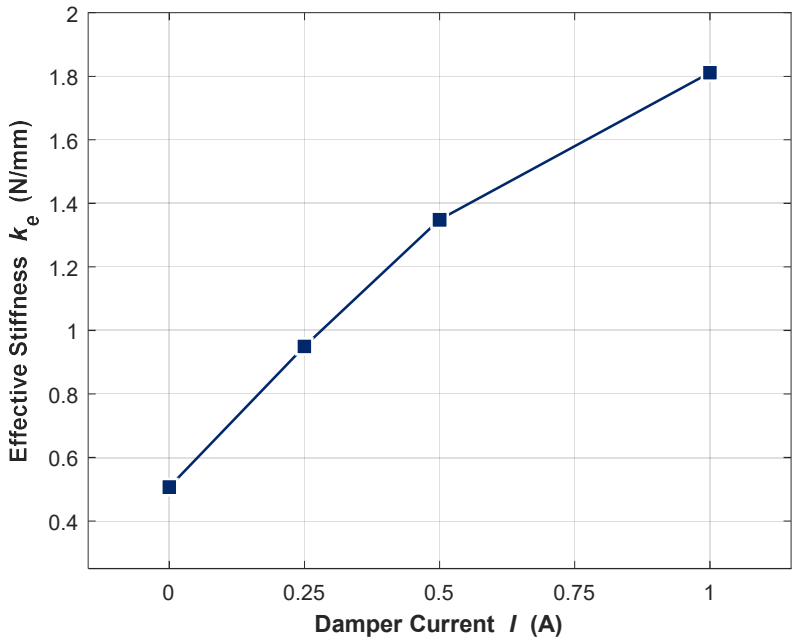

Figure 3-8 Relationship between current and effective stiffness.

Table 3-3 Calculated effective stiffness values of the MRVSAL-I.

Current (A)	Effective Stiffness (N/mm)
0.00	0.507
0.25	0.950
0.50	1.348
1.00	1.811

3. 4 Locomotion Testing

In order to characterise the dynamic performance of the variable stiffness leg, a test rig was fabricated to facilitate simple two-dimensional running. This hosts a bipedal test platform with limited degrees of freedom (DOF) that is constrained to

move only through the sagittal plane. This allows it to translate both horizontally and vertically, restricting lateral motion and all rotational degrees of freedom. The test rig, shown in the CAD model of **Figure 3-9**, has an aluminium extrusion frame, with a plywood base 20 mm thick, providing an adequately rigid structure. The 5.9 kg robot platform follows vertical and horizontal rails upon which a guide carriage is mounted to restrict rotation of the platform and house a laser used to measure vertical displacement (Keyence LB-11/LB-60; 80 mm to 120 mm range).

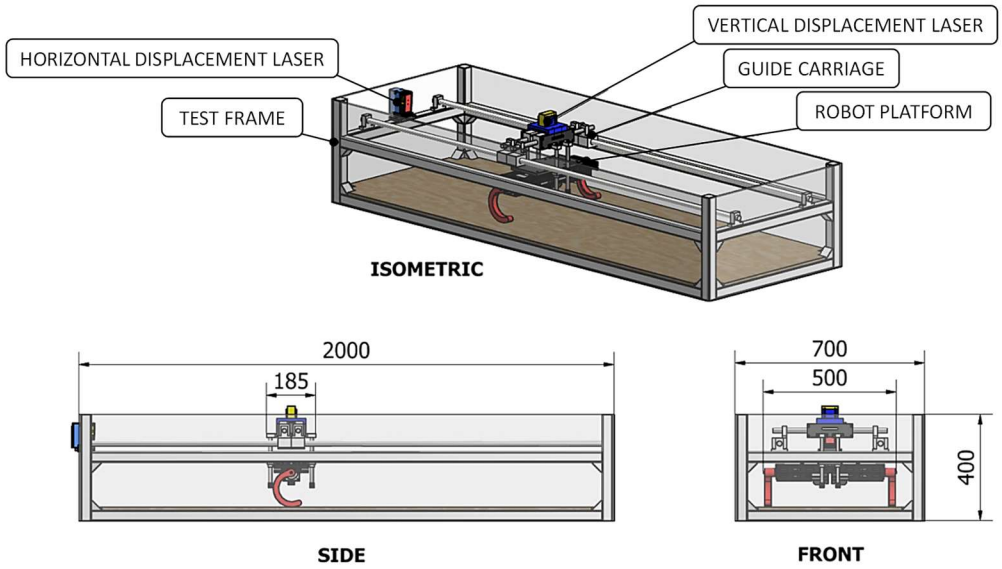

Figure 3-9 Locomotion test rig CAD model (dims in mm).

To measure horizontal (sagittal-axis) displacement and calculate average forwarding velocity v_{avg} of the robot platform, a SICK DT60-P211B laser with an effective range of 0.2 m to 5.3 m is equipped to the rig. To actuate the legs of the platform, two AC synchronous motors (Panasonic 1.3 N·m MSMJO42G1U, with MBDKT2510CA1 200 V driver) are coupled to 10:1 planetary reduction gearboxes, providing a maximum output torque of 13 N·m to the legs. These motors are also able to measure torque and can be used to determine average locomotive power consumption P_{avg}. The mechanical cost of transport (MCOT) can be considered to purely assess the contribution of stiffness modulation to locomotion cost, neglecting MR damper power [51]. This MCOT can be found using:

$$MCOT = \frac{P_{avg}}{m_{biped} \cdot g \cdot v_{avg}}, \tag{3-18}$$

where m_{biped} = 7.2 kg is the total platform and leg mass and g = 9.81 m/s^2 is gravity.

To energise the MRF joints of the leg, a DC power supply is used, with varied currents set between tests. Seen in the test setup shown in **Figure 3-10**, regarding the data acquisition and control, the system uses an NI myRIO-1900, programmed through NI LabVIEW, with a host computer to prepare tests and display live measurements.

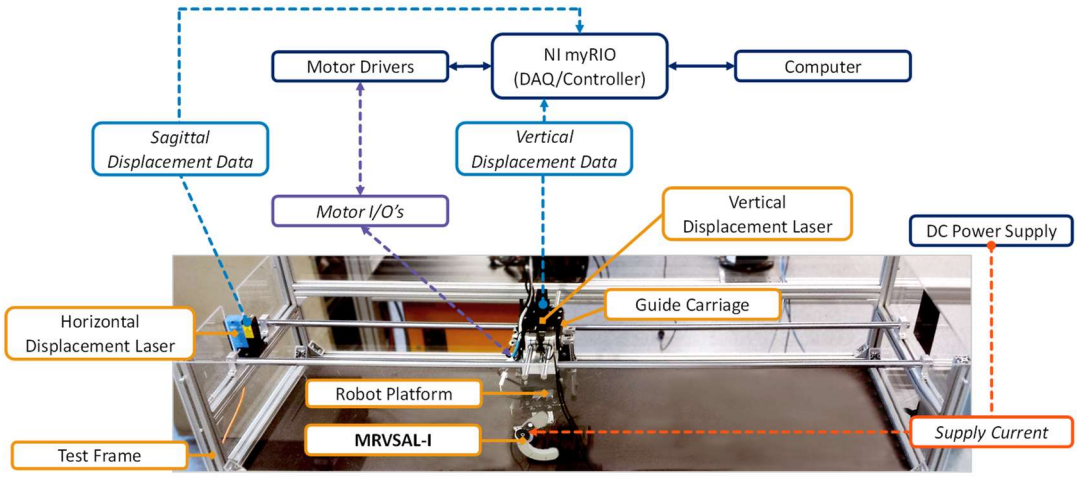

Figure 3-10 Experimental setup for limited-DOF legged locomotion testing.

In the tests carried out here, a gait pattern typical of hexapods is employed, wherein for a designated contact range (set to 90°) the legs will rotate at a set-speed while they contact the ground, after which it is assumed they have lost contact, so they will then rapidly rotate (at a rate of 45 rad/s) until they return to take another step [91]. Additionally, to improve stability, the legs walk with a 45° phase difference (half of the contact range). During these tests, the platform is set to run a 1 m length, with measurements taken in a from 0.4 m to 0.7 m, considered as a safe range away from starting or stopping disturbances. This was done over a range of contact speeds for the legs, i.e. the stance leg-speed, ranging from 0.5 rad/s to 15 rad/s. This yielded the plotted values of MCOT in **Figure 3-11** for the minimum possible stiffness of the legs (0 A input current), and the maximum stiffness (2 A input current, to ensure magnetic saturation). Each test was conducted numerous times to yield a more reliable result.

A key observation made here is that in the low-speed range, i.e. speeds lower than about 5 rad/s, the MCOT is generally reduced for a lower leg stiffness, illustrating improved energy efficiency under this condition. The largest change in this speed range occurs at 1.5 rad/s with a mean reduction of 23.5% from an MCOT of 6.09 to 4.66. Towards higher speeds which are above 8 rad/s, the trend is opposite, with a higher leg stiffness reducing the MCOT. The maximum reduction occurs at 10 rad/s

from an MCOT of 4.51 to 3.29, representing a 27.0% mean reduction. While this result is not necessarily indicative of the theorised resonant running, what it does show in line with theory is that modulating leg stiffness in legged robots can improve energy efficiency while locomoting. Although more adept control strategies may yield better results, even a simple series of conditions based on leg speed could give this platform improved gait performance, as evidenced by this result. Specifically, the MRVSAL-I could reduce stiffness when the running speed is less than about 5 rad/s and increase stiffness when the speed is greater than 5 rad/s. With this control method, the proposed design can achieve an overall lower MCOT than the passive stiffness modes.

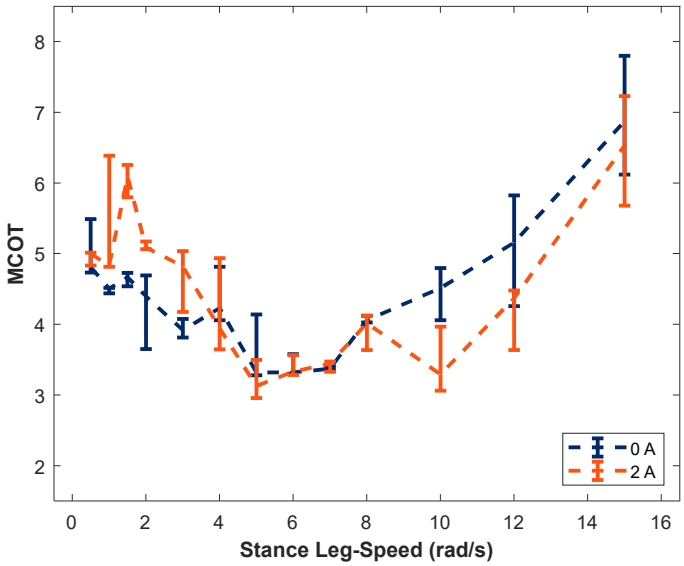

Figure 3-11 MCOT of bipedal test platform equipped with MRVSAL-I.

3. 5 Chapter Summary

This chapter presented a variable stiffness MRF-based variable stiffness actuator leg, the MRVSAL-I, inspired by biological studies and the impeccable performance of legged creatures. Following mathematical modelling, the leg was characterised through linear compression testing. It was shown to be capable of a maximum stiffness increase of 257%, with the result giving validation to the proposed force-displacement model describing the leg. Following this, a limited-DOF locomotion test rig featuring a bipedal robot platform was presented. When fit to the robot platform, the legs proved to be an effective solution to improve locomotive performance through reducing MCOT. With the locomotion results presented here showing promise, this gives reason to continue investigation into other aspects for the potential of MRF-based variable stiffness robot legs.

4 IMPROVED MAGNETORHEOLOGICAL-FLUID-BASED VARIABLE STIFFNESS FOR LEGGED LOCOMOTION AND SLIP STABILITY

4. 1 Introduction

Variable stiffness actuators often form part of a more-complex robotic linkage where it is important to possess dynamic balance [92]. Without a balanced COM of the robot, shaking forces and moments will cause vibration, noise, wear, and fatigue problems [93, 94]. Furthermore, a larger moment of inertia due to an inherent lack of balance would result in a greater energy cost of actuation. If these factors are not closely managed, inertial loads may exceed actuator capabilities, particularly for geared motors [60], and reduce the efficacy of trajectory control efforts [95]. Despite promise shown by the former C-shaped leg morphology applied in **Chapter 3**, there exist some limitations with the design due to these factors. To improve upon these, MRF has been applied in an improved design, the MRF-based variable stiffness actuator leg mark-II (MRVSAL-II). This leg now features a balanced COM about the torque-actuation hip joint of the bipedal robot platform it is suited to. Furthermore, the geometry of the new leg facilitates greater deflection before bottoming out, which

limited the practicality of the previous design for experiments involving, obstacles, valleys, or other impact loading. While the design utilises MRF as before, the leg-behaviour differs in morphology and mechanism.

Given the MRVSAL-II is rotationally balanced, it is reasonable to consider dynamic locomotion modelling. The SLIP model has been widely applied in original or modified form [55, 56, 58, 96-98] to characterise the behaviour of legged robots. By virtue of the SLIP geometry and dynamic equations, the touchdown velocity and respective angle of attack are pre-defined. The landing angle of the leg spring is similarly maintained between each step. Such conditions make comparison between locomotion simulations with different leg stiffnesses, i.e. variable stiffness, quite convenient. By iteratively performing simulations, locomotion stability can then be assessed through steps-to-fall analysis [55, 99, 100] or, alternatively, return-map analysis [53, 55].

To study the MRVSAL-II, it is first characterised through a series of compression tests with varied loading conditions and damper currents. The behaviour of the leg is then mathematically modelled and simulated to compare against the experimental results. Following this, on the basis of the variable stiffness provided by the leg, the SLIP model is setup for continuous running simulations with different stiffnesses corresponding to those achievable by the MRVSAL-II. Stability of the model is then evaluated through steps-to-fall analysis.

4. 2 MRVSAL-II Design

4.2.1 Leg Morphology and Design

The leg morphology of the MRVSAL-II is based on the leg linkage of [28], utilising a similar variable stiffness mechanism as in **Chapter 3**, but now being dynamically balanced and with improved deflection capability. The structure of the MRVSAL-II is illustrated in the CAD model of **Figure 4-1**. As detailed, the key parts include upper and lower leg segments which are pinned together, also connecting through the variable stiffness mechanism via a draw cable. These elements of the leg are 3D printed in low-density Nylon, with a composite structure of fiberglass, forming lightweight but rigid parts. These were fabricated using the Markforged Mark Two FDM 3D printer. The lower leg segment has a silicone rubber foot pad to help soften impacts and improve friction during leg-ground contact. The upper leg segment is

rigidly connected with a motor-coupling section which allows it to connect to a drive motor of the robot platform. Additionally, the slip ring is needed to supply electric current to the damper as the leg rotates, with graphite brushes mounted on the robot platform.

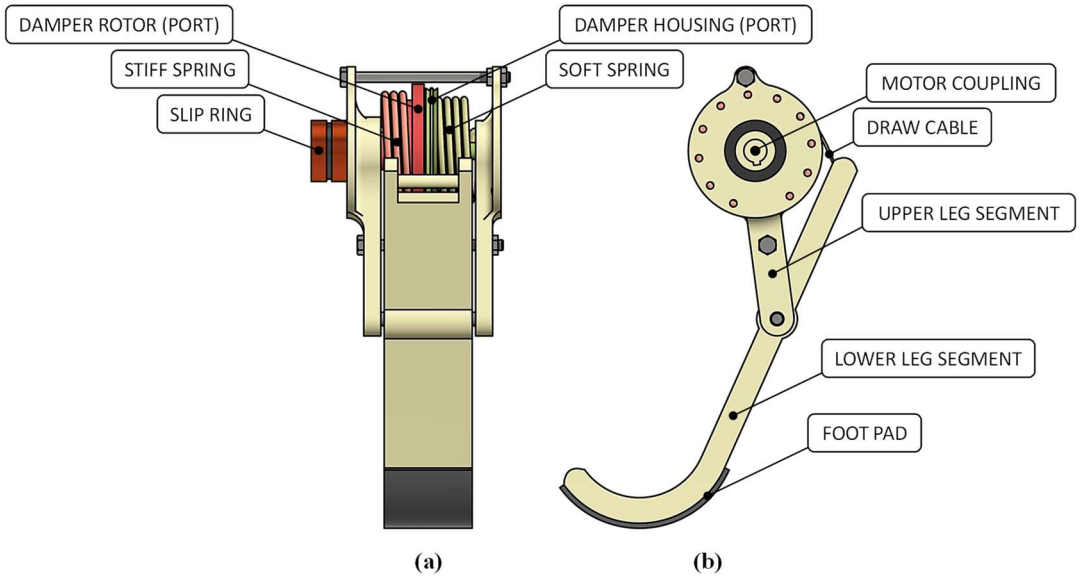

Figure 4-1 MRVSAL-II CAD model (a) rear-view, and (b) side-view.

To elaborate on the arrangement of the variable stiffness mechanism, **Figure 4-2(a)** is a cross-sectional view of the mechanism, with **Figure 4-2(b)** showing the functional diagram. This mechanism is functionally identical to that presented in **Chapter 3**, primarily differing in the arrangement and how the torsional mechanism couples to the leg linkage. The relatively stiff spring, with k_{stiff} = 10580 N·mm/rad, connects between the upper leg segment and damper rotor, labelled as a 'port' in **Figure 4-2(a)**, given the physical connection goes through the spring hub, damper shaft, and then damper rotor. The relatively soft spring, with k_{soft} = 400 N·mm/rad, also connects to the upper leg segment and, in this case, the damper housing port, i.e. the cable pulley and damper housing, with this spring also having an included preload of $\psi_{2,i} = 40°$. Referring to **Figure 4-2(b)**, when $\left(T_{VS,out} - T_{VS,in}\right) \neq 0$, i.e. if leg is compressed, the soft spring will be externally loaded and experience the relative displacement $(\psi_2 - \psi_0)$. However, if the damper is not energised, the low off-state viscosity of the contained MRF will result in effectively zero loading of the stiff spring, with $(\psi_1 - \psi_0) = 0$, and $(\psi_2 - \psi_1) \cong (\psi_2 - \psi_0)$. If the damper is energised

sufficiently, the high MRF viscosity will rigidly lock the damper rotor and damper housing together, setting $(\psi_2 - \psi_1) = 0$. For a level of damping between these two extremes, a continuous range between k_{soft} and $(k_{stiff} + k_{soft})$ will result, and be translated to a linear stiffness through the draw cable attached between the damper housing and lower leg. Also shown in **Figure 4-2(b)**, the viscous damping of the leg body, $c_{body} \cong 2600$ N·mm·s/rad, is included to describe the energy loss due to hysteresis of the leg materials. When coupled to the actuation motor, the leg functions as a VSA, with a total leg weight of 1.2 kg.

(a)

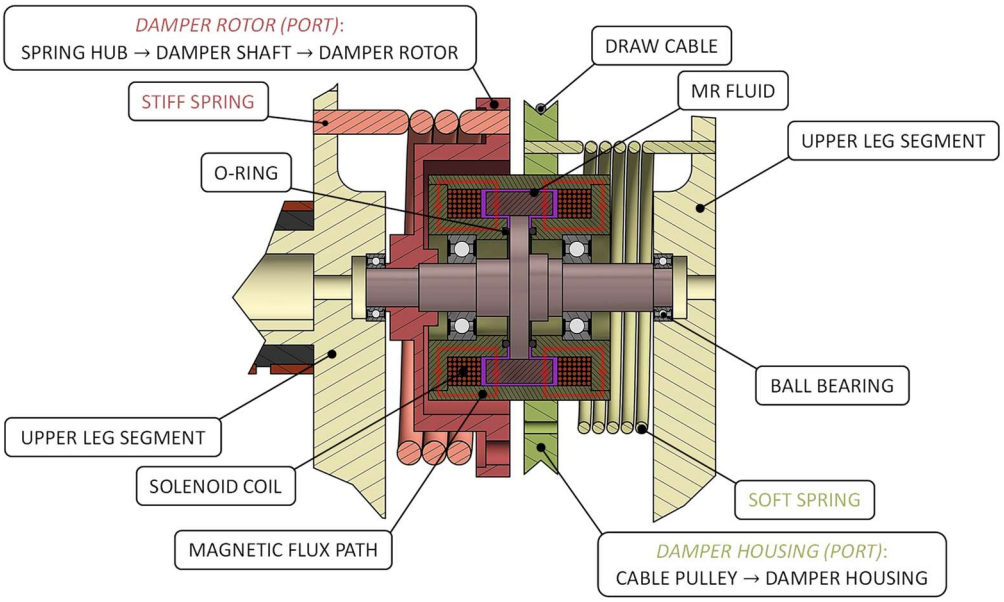

(b)

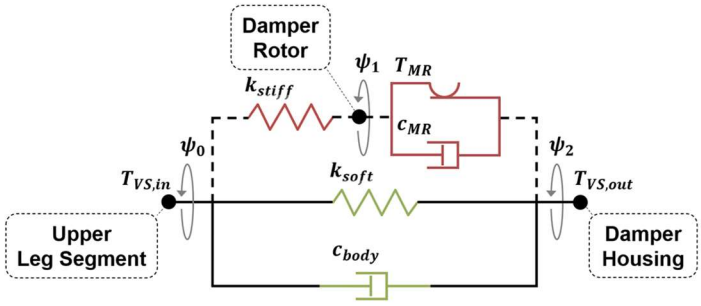

Figure 4-2 Variable stiffness mechanism (a) CAD model sectional view, and (b) functional diagram.

4.2.2 Magnetorheological Damper Modelling

The rotary MR damper employed in the MRVSAL-II is identical to that introduced in **Chapter 3**, as illustrated in the variable stiffness mechanism sectional view of **Figure 4-2(a)**. However, the housing and rotor are a different grade of steel, in this case known to be AISI 1045. The shaft is similarly non-magnetic aluminium, and the MRF is LORD MRF-140CG. The change in MRF viscosity and consequent damper torque is captured quite well by the Bingham plastic model [76], which describes the viscoplastic behaviour of the MRF as the sum of a constant viscous damping coefficient c_{MR} and a field-controllable Coulomb friction component T_{MR}, illustrated in **Figure 4-2(b)**.

To remodel damper torque, also over a greater current range, an FEM magnetic field study was conducted using COMSOL Multiphysics ver. 5.4. For the simulation, material data provided by LORD was utilised for the MRF [90], with the B-H relationship for AISI 1045 steel obtained from [101]. Given the damper design features two regions in which the MRF experiences a different magnetic flux density B, the mean flux in these areas are separately analysed, referred to as the inner-gap and outer-gap. With the coil current increased from 0 A to 2 A, these average flux values are plotted against current in **Figure 4-3** for both regions. As the current is increased up to 2 A, the saturation of this magnetic flux is apparent, with the flux density reaching 0.86 T for the inner-gap, and 0.47 T in the outer-gap. To account for the remanent flux density induced by the 2 A coil current and hysteresis of the steel, the 0 A flux is set as 0.09 T for the inner-gap, and 0.04 T for the outer-gap.

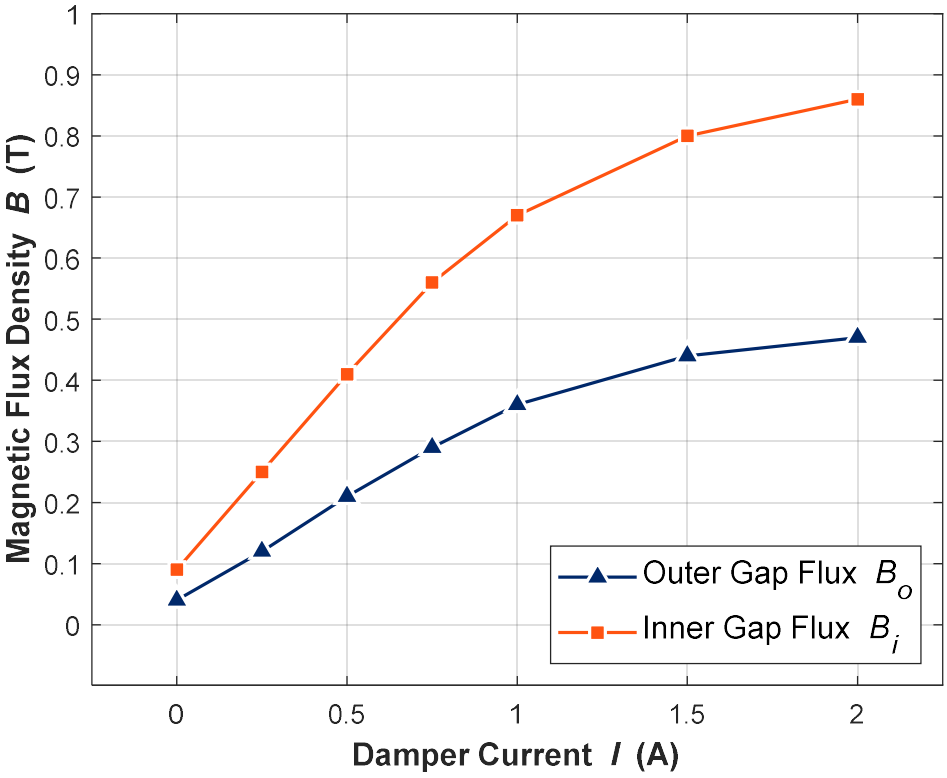

Figure 4-3 Improved rotary MR damper mean MRF magnetic flux density.

4. 3 Leg Experimental Characterisation

4.3.1 Compression Testing Experimental Setup

In order to experimentally characterise the apparent contact force F'_{Py} and effective stiffness k_e of the MRVSAL-II, the experimental setup illustrated in **Figure 3-6** was identically utilised. In this arrangement the upper leg segment is rigidly fixed to the upper clamp of an MTS Landmark hydraulic test system (Load Frame Model: 370.02, MTS Systems Corp.), with the lower leg segment, foot pad removed, free to slip on a low friction base plate affixed to the force transducer of the machine. The force measured by this sensor is taken as the apparent contact force F'_{Py} produced by the leg, experienced by the base plate in the normal direction. Through linear-displacement ramping of the actuator of the upper clamp, the system supplies uniaxial loading to the vertically oriented leg. To provide current to the coils of the rotary MR damper inside the MRVSAL-II, a DC power supply (CPX400A, Aim-TTi Ltd.) is used. The force and displacement data are logged to a computer via an integrated DAQ board.

4.3.2 Test Results and Analysis

With the MRVSAL-II affixed, the MTS was set to compress the leg under cycled loading following ramped displacement paths over a varied range from 5 mm to 15 mm amplitude between tests. In addition to amplitude levels, loading speed was varied over a range of 2.5 mm/s to 10 mm/s to obtain a variety of loading conditions for the leg. To investigate the influence of the damper, fixed current levels were set between test runs over a 0 A to 2 A current range. First, to study the behaviour of the apparent contact force F'_{Py} in response to changing damper currents, **Figure 4-4(a)** and **(b)** show the force-displacement loops generated under the cycled ramp loads ran at a 5 mm/s speed for two amplitude levels, 10 mm and 15 mm, respectively. With these loops generating in a clockwise manner, it can be seen that for the 10 mm runs, there is an apparent increase in peak force from 25.3 N to 46.0 N, an 81.8% increase, when current is varied from 0 A to 2 A. Similar behaviour can be observed for the 15 mm runs, with slightly larger forces generated, peaking at 26.8 N to 56.3 N for 0 A to 2 A, respectively, representing a 110% increase in this case. Based on the modelling included in **Section 4.4**, the compression testing analysis was simulated in MATLAB SIMULINK ver. 9.1, with the overlayed simulation result included in **Figure 4-4(a)** and **(b)**.

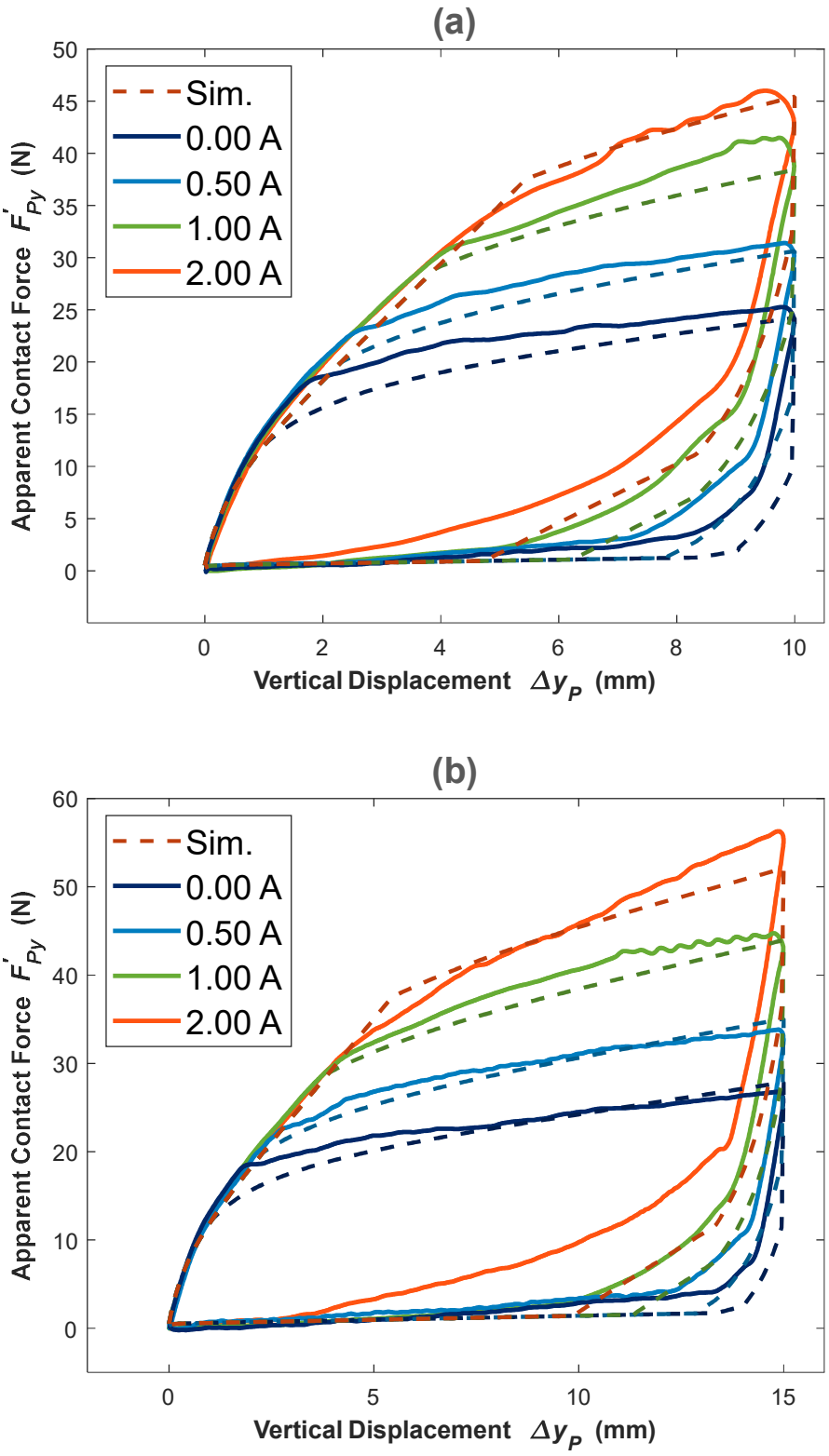

Figure 4-4 Force characterisation results (exp. and sim.) under (a) variable damper current with 10 mm displacement and 5 mm/s speed, (b) variable damper current with 15 mm displacement and 5 mm/s speed.

Presented in **Figure 4-5** is the effective stiffness k_e, calculated for these two sets of tests, following **Equation (4-1)** [29]:

$$k_e = \frac{F_{\Delta,max} - F_{\Delta,min}}{\Delta y_{P,max} - \Delta y_{P,min}} \quad [\mathrm{N/m}], \tag{4-1}$$

where $F_{\Delta,max}$ and $F_{\Delta,min}$ are the forces corresponding to the maximum and minimum displacement amplitudes of a given cycle, $\Delta y_{P,max}$ and $\Delta y_{P,min}$, respectively. With numerical values reported in **Table 4-1**, for the 10 mm runs, we observe an increase in stiffness over the 0 A to 2 A current range of 83.7% from 2.51 N/mm to 4.61 N/mm, identical to the increase in peak force. With the 50% larger amplitude of 15 mm, we find a stiffness increase of 114% from 1.77 N/mm to 3.79 N/mm over the same current range. Between the two sets of tests, it is also observed that there is an average 26.7% reduction in stiffness when loading amplitude is increased from 10 mm to 15 mm.

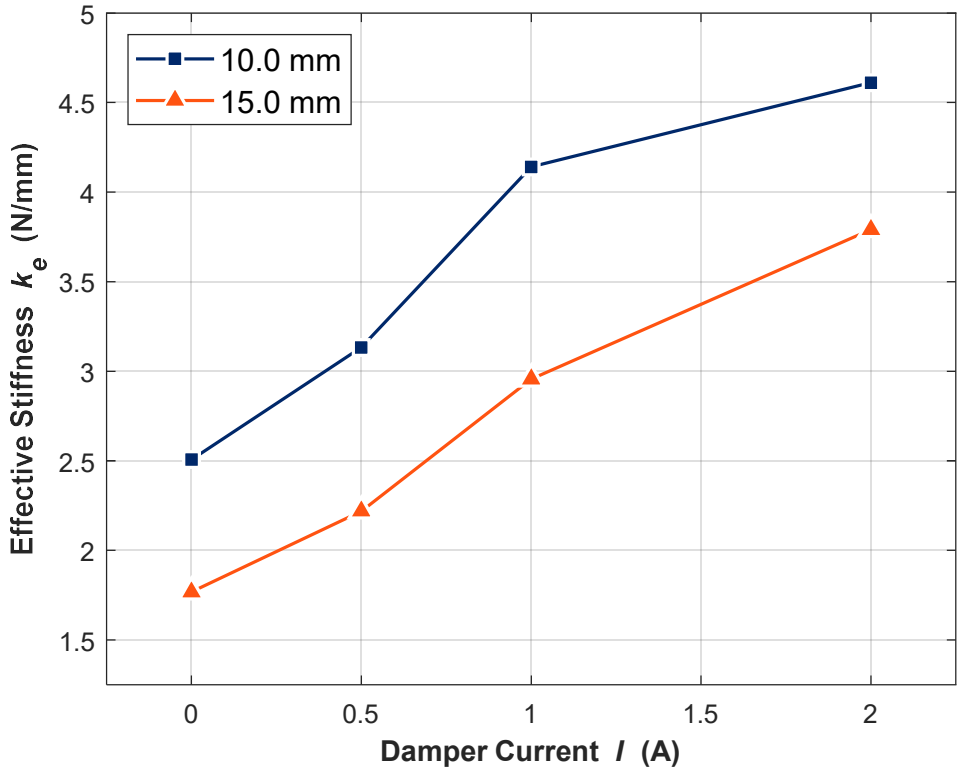

Figure 4-5 Effective leg stiffness for varied damper current.

Table 4-1 Calculated effective stiffness values of the MRVSAL-II.

Current (A)	Effective Stiffness, 10.0 mm (N/mm)	Effective Stiffness, 15.0 mm (N/mm)
0.00	2.51	1.77
0.50	3.13	2.22
1.00	4.14	2.96
2.00	4.61	3.79

To further investigate the behaviour of the leg, with a fixed loading speed set to 5 mm/s, **Figure 4-6** shows the variation in apparent contact force with increased displacement amplitude, including 5 mm, 10 mm, and 15 mm, with 0 A and 2 A of current. Under 0 A of current, from 5 mm to 15 mm, an increase in peak force of 18.2% is observed, with a more substantial increase of 58.1% in the 2 A case. Loading speeds were also varied between a minimum of 2.5 mm/s, 5 mm/s, and maximum of 10 mm/s under 0 A and 2 A current, set to the same 10 mm and 15 mm amplitudes, included in **Figure 4-7(d)** and **(e)**, respectively. Notably, minimal variation is witnessed in relation to the loading speed, with peak forces not exceeding 7.36% variation across runs of identical conditions.

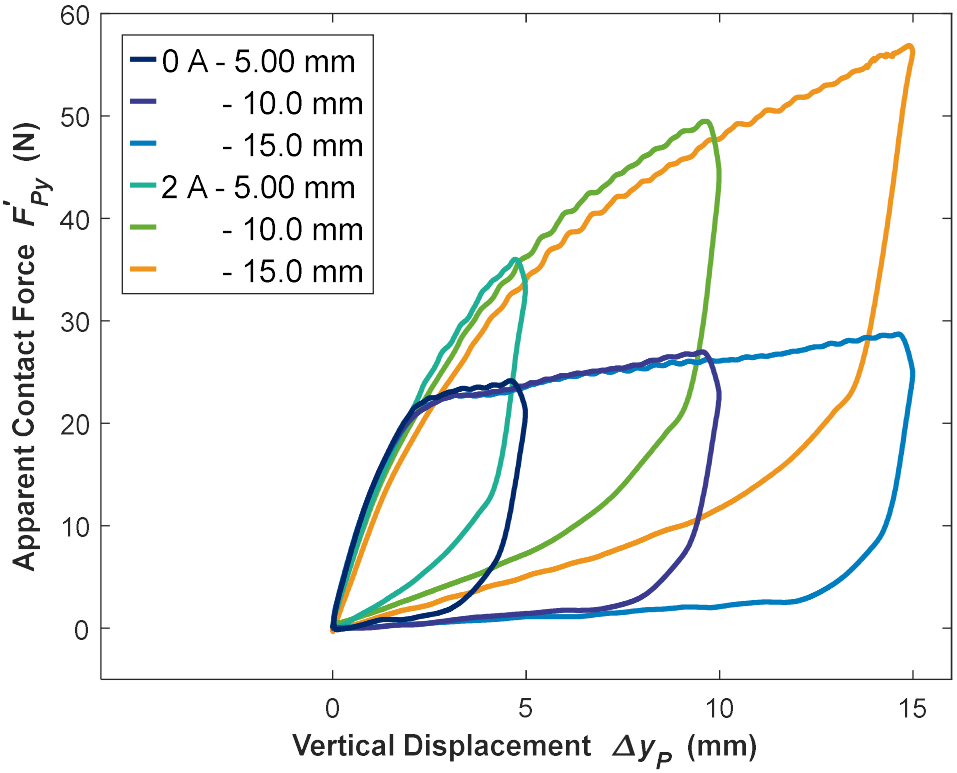

Figure 4-6 Force characterisation results under variable displacement.

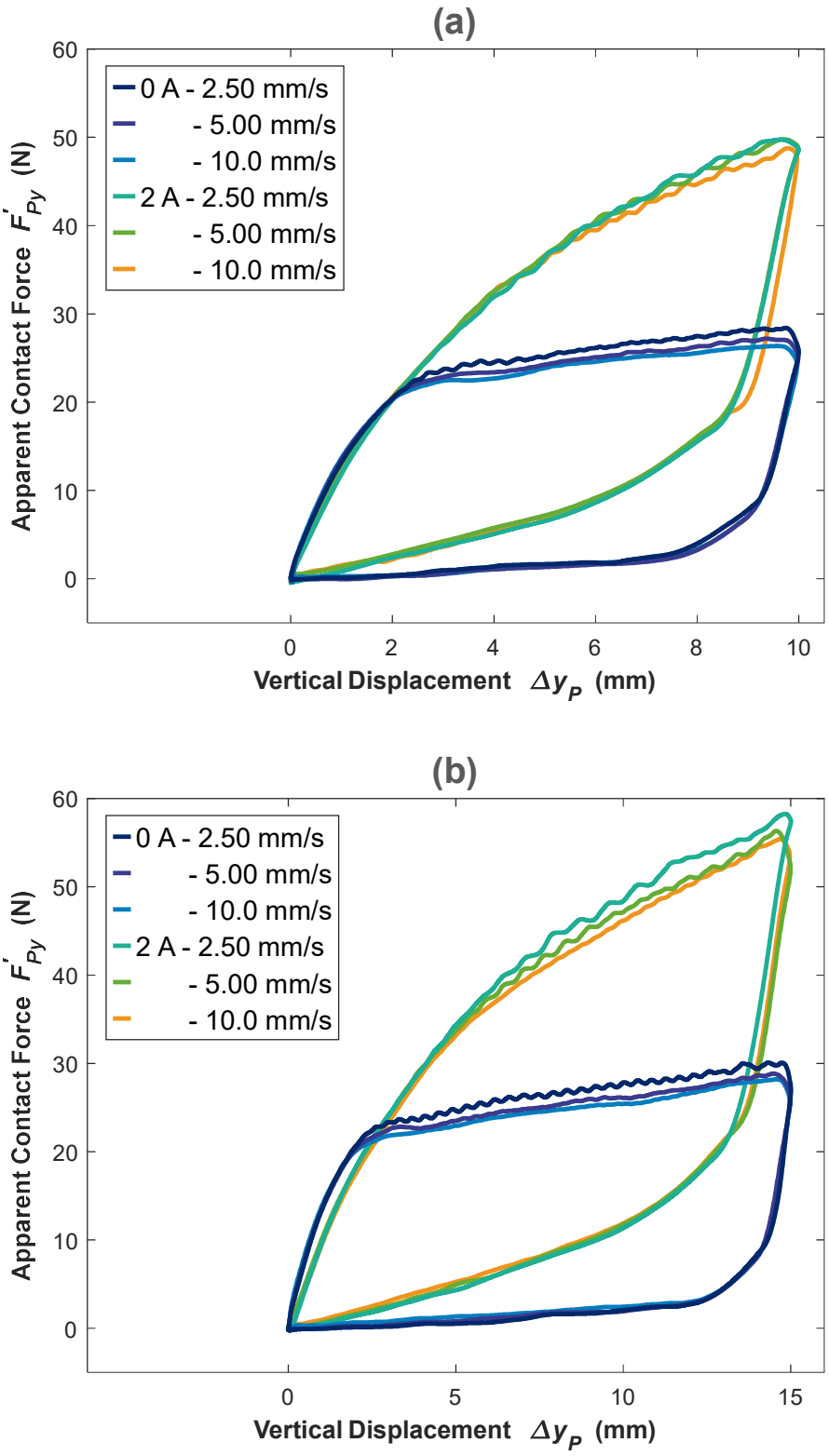

Figure 4-7 Force characterisation results under (a) variable loading speed with 10 mm displacement, (b) variable loading speed with 15 mm displacement.

4. 4 Leg Force Modelling

We may now refer to **Figure 4-8** and **Figure 4-9** to establish the geometric and force relationships of the MRVSAL-II, respectively, with the relevant dimensions and initial conditions included in **Table 4-2**. At the leg-ground contact point P, with the leg in the vertically oriented position as in the compression testing, a vertical displacement Δy_P causes the lower leg segment to rotate about the pin joint O which connects it to the upper leg segment. This, in turn, causes the draw-cable connection point C to rotate along a circular path, with a chord length equal to the cable extension Δl_{CD}. This extension acts as the input displacement which then rotates the variable stiffness mechanism to produce a torque.

Table 4-2 MRVSAL-II geometric parameters.

Fixed Dimensions		Required Initial Conditions	
Parameter	Value (mm | deg.)	Parameter	Value (mm | deg.)
l_A	104.4	$y_{A,i}$	48.3
l_C	89	$l_{CD,i}$	46.9
l_D	123.9	$\theta_{1,i}$	52.2
θ_4	144	$\theta_{2,i}$	17.2
r_A	47.5		
r_H	35		
b	20		

As a first step, we may refer to points A, O, and P in **Figure 4-8** in order to determine the angular displacement $\Delta\theta_1$ of the lower leg segment about O as a consequence of the vertical input displacement Δy_P. Since we know $l_{Px} = l_{Ax}$ and $l_{Py} = l_{Ay} + l_{AP}$, we may use trigonometry to find the corresponding change in angle $\Delta\theta_1$. Starting with l_{Px}:

$$l_{Px} = l_{Ax} = \sqrt{l_A^2 - l_{Ay}^2} = \sqrt{l_A^2 - (l_A - y_A)^2} \quad \text{[m]}, \tag{4-2}$$

where $y_A = y_{A,i} + \Delta y_P$, keeping in mind that the centre of curvature of the foot y_A always remains directly above the leg-ground contact point y_P. We then obtain l_{Py} through the summation:

$$l_{Py} = l_{Ay} + l_{AP} = (l_A - y_A) + (r_A + b/2) \quad \text{[m]}, \tag{4-3}$$

with l_{AP} being the fixed length defined by the radius of curvature of the foot r_A and the foot thickness b. Lastly, using the inverse tangent function we may determine the change in leg angle $\Delta\theta_1$:

$$\begin{aligned} \Delta\theta_1 &= \operatorname{atan}\left(\frac{l_{Py}}{l_{Px}}\right) - \theta_{1,i} \\ &= \operatorname{atan}\left(\frac{l_A - y_{A,i} - \Delta y_P + r_A + \frac{b}{2}}{\sqrt{l_A^2 - \left(l_A - y_{A,i} - \Delta y_P\right)^2}}\right) - \theta_{1,i} \quad \text{[rad]}. \end{aligned} \tag{4-4}$$

Next we may refer to points C, O, and D in **Figure 4-8** to determine the cable extension Δl_{CD} and its angle relative to the lower leg segment, based on θ_3. Starting with the cable extension Δl_{CD}, this may be found by application of the cosine rule:

$$\Delta l_{CD} = l_{CD} - l_{CD,i} = \sqrt{l_C^2 + l_D^2 - 2 l_C l_D \cos(\theta_2)} - l_{CD,i} \quad \text{[m]}, \tag{4-5}$$

where $\theta_2 = \theta_{2,i} - \Delta\theta_1$, recognising that $\Delta\theta_2 = -\Delta\theta_1$. To then determine the draw-cable's angle relative to the lower leg segment, i.e. $\theta_3 - 90°$, we may apply the sine rule as follows:

$$\theta_3 = \operatorname{asin}\left(\sin(\theta_2) \cdot \frac{l_D}{l_{CD}}\right) \quad \text{[rad]}, \tag{4-6}$$

where θ_3 can be made use of in the relationship between sine and cosine angles, i.e. $\sin(\theta_3) = \cos(90° - \theta_3)$.

Now referring to **Figure 4-9**, we can determine an expression for the contact force F_{Py} acting on the leg at point P. Summing the moments about the pin joint at O:

$$\sum M_O = 0: \qquad F_{Py} \cdot l_{Px} - F_{Px} \cdot l_{Py} - F_C \cdot \sin(\theta_3) \cdot l_C = 0. \tag{4-7}$$

Recognising F_{Px} to be the friction force between the foot and test platform, we may consider $F_{Px} = \mu_k \cdot F_{Py} \cdot \text{sgn}(\Delta\dot{x}_P)$, where $\mu_k \cong 0.25$. In practice, we may equivalently consider $\text{sgn}(\Delta\dot{x}_P) = \text{sgn}(\Delta\dot{y}_P)$ to simplify and solve **Equation (4-7)** to yield the following:

$$F_{Py} = \frac{F_C \cdot \sin(\theta_3) \cdot l_C}{l_{Px} - \mu_k \cdot \text{sgn}(\Delta\dot{y}_P) \cdot l_{Py}} \quad \text{[N]}. \tag{4-8}$$

To determine the cable force F_C of **Equation (4-8)**, produced by the variable stiffness mechanism, we must first form a description of the MR damper torque T_{MR}. Referring to **Figure 4-3**, we may use a polynomial in order to describe the apparent relationship between coil current I and damper magnetic flux density within the inner-gap B_i and outer-gap B_o:

$$B_i(I) = -0.0230 \cdot I^3 - 0.1263 \cdot I^2 + 0.7347 \cdot I + 0.0750 \quad \text{[T]}, \tag{4-9}$$

and

$$B_o(I) = -0.0292 \cdot I^3 - 0.0153 \cdot I^2 + 0.3646 \cdot I + 0.0335 \quad \text{[T]}. \tag{4-10}$$

Based on the modelling work of **Chapter 3** in **Section 3.2.3**, we may then apply **Equations (3-9)** through **(3-11)** to establish the damper yield torque T_{MR} as a function of shear stress τ_y and hence coil current I, following the Bingham plastic model. Given the viscous damping is relatively insignificant within the variable stiffness mechanism, i.e. $c_{MR} \ll c_{body}$, we may simplify the model and consider the yield torque to be the total torque produced by the damper.

Moving on, from the pulley radius of the damper housing r_H, we also know $\Delta\psi_2 = \Delta l_{CD}/r_H$ and $F_C = T_{VS,out}/r_H$, but do not yet have a complete description of the variable stiffness mechanism torque $T_{VS,out}$. Effectively, we may consider two working modes based on the yield state of the MR damper, as explained in **Section 4.2.1**. In addition, since the upper leg segment is fixed in the compression testing, we may set $\psi_0 = 0$. For the post-yield state, i.e. when the condition $k_{stiff} \cdot \psi_1 > T_{MR}$ is met, we have $\Delta\psi_1 = 0$ and hence:

$$\psi_1 = \psi_{1,y} \quad \text{[rad]}, \tag{4-11}$$

where $\psi_{1,y}$ is the yield angle of the damper, which is set at the instant the stiff spring torque surpasses the damper torque. On the other hand, while operating in the pre-yield state, i.e. when $k_{stiff} \cdot \psi_1 \leq T_{MR}$, we have $\Delta\psi_1 = \Delta\psi_2$ and find:

$$\psi_1 = \Delta\psi_2 + \psi_{1,y} \quad \text{[rad]}. \tag{4-12}$$

During either state, the resultant cable force F_C is given by:

$$F_C = \frac{T_{VS,out}}{r_H} = \frac{k_{soft} \cdot \psi_2 + c_{body} \cdot \dot{\psi}_2 + k_{stiff} \cdot \psi_1}{r_H} \quad \text{[N]}, \tag{4-13}$$

which may be used in **Equation (4-8)** to determine the contact force F_{Py}.

Lastly, since the leg structure has some compliance within it itself, this may be taken into account as a linear stiffness $k_{actual} \cong 50$ N/mm, acting in series with the overall rigid leg stiffness $k_{rigid} = F_{Py}/\Delta y_P$ to resolve to k_e. This produces an output force which softens somewhat through the displacement cycle, as observed during testing. This apparent contact force F'_{Py}, as indicated in **Figure 4-4(a)** and **(b)**, is then determined from **Equation (4-14)**:

$$F'_{Py} = \frac{k_{rigid} \cdot k_{actual}}{k_{rigid} + k_{actual}} \cdot \Delta y_P \quad \text{[N]}. \tag{4-14}$$

The simulated results show a reasonable match to the experimental data, and in particular the yield point of the MR damper where the variable stiffness mechanism switches stiffness states from $(k_{stiff} + k_{soft})$ to k_{soft}.

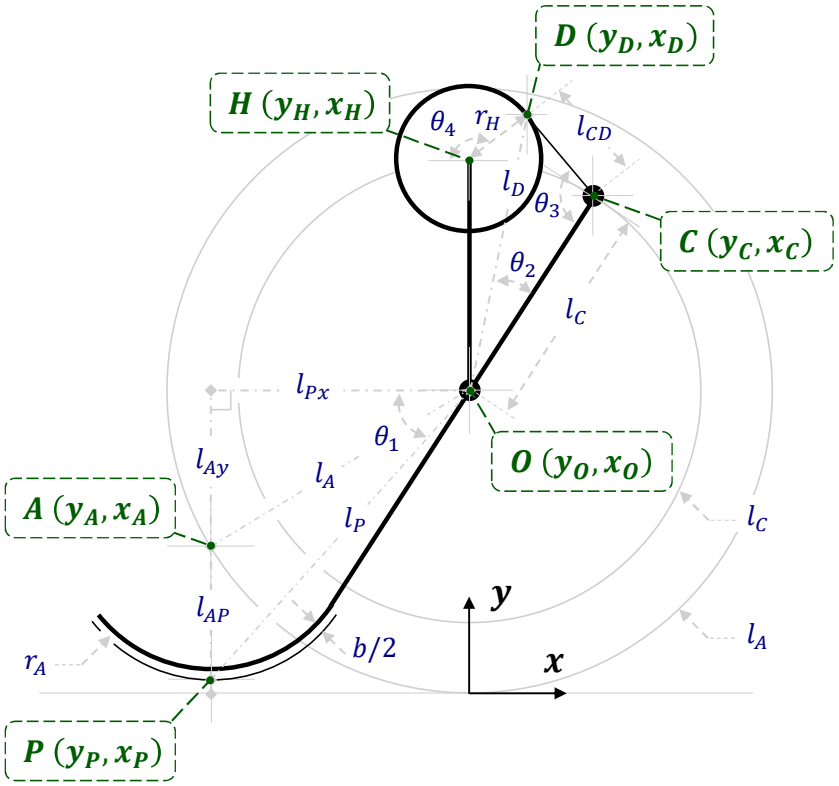

Figure 4-8 MRVSAL-II linkage geometric parameters.

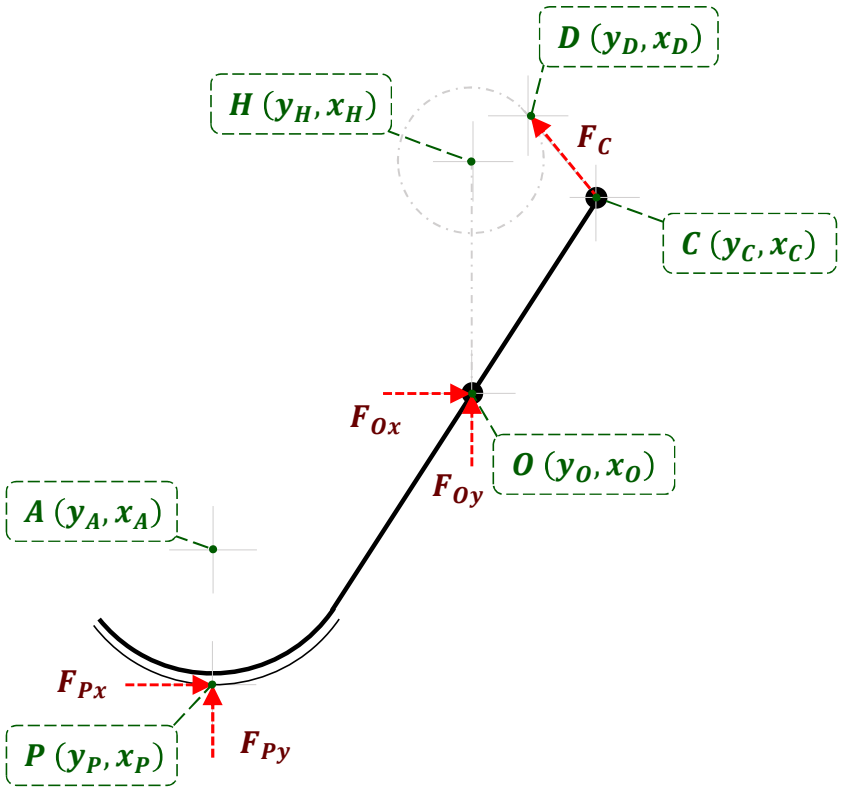

Figure 4-9 MRVSAL-II lower leg segment free body diagram.

4. 5 Steps-to-Fall Stability Analysis

4.5.1 Continuous Running SLIP Model Setup

In order to study the potential improvement to locomotion stability, the SLIP model will now be employed. The SLIP model and variants of it have been frequently used in the past to characterise compliant-legged robots [55, 56, 96-98, 102]. Where the MRVSAL-II provides an apparent level of hysteretic damping, this will be neglected, given the SLIP model is conservative [12] and does not consider leg-actuator input energy or energy dissipated. As such, this stability analysis will serve as a general guide towards the trend of locomotion stability, considering the stiffness range offered by this variable stiffness leg.

The equations of motion can be described by the discrete coupling of two states: stance phase and flight phase. During stance phase, the horizontal travel, i.e. coronal- or x-axis motion is described by the nonlinear differential equation [12]:

$$\ddot{x} = x \cdot \omega_n^2 \cdot \left(\frac{l_0}{\sqrt{x^2 + y^2}} - 1 \right), \tag{4-15}$$

and the vertical travel, i.e. transverse- or y-axis motion is described identically by:

$$\ddot{y} = y \cdot \omega_n^2 \cdot \left(\frac{l_0}{\sqrt{x^2 + y^2}} - 1 \right) - g, \tag{4-16}$$

where $\omega_n = \sqrt{k/m}$ is the natural frequency of the system, l_0 = 0.2 m is the free-length of the effective leg spring, and g is simply the acceleration due to gravity, 9.81 m/s^2. Here, we will also take the stiffness $k = k_{biped} = 2 \cdot k_e$ from **Section 4.3.2** and mass $m = m_{biped} =$ 15.2 kg, as outlined in **Chapter 5** under **Section 5.2.1**. For the flight phase dynamics, the system follows a ballistic trajectory, governed by zero horizontal acceleration:

$$\ddot{x} = 0, \tag{4-17}$$

and purely vertical acceleration due to gravity:

$$\ddot{y} = -g. \tag{4-18}$$

To then determine how to switch between these two states, switching conditions must now be established. With reference to **Figure 2-3**, we commence locomotion at the onset of touchdown (TD). At this point, the vertical position of the COM of the SLIP locomotor $y = y_{TD}$ falls below the vertical component of the uncompressed spring length, i.e.

$$y_{TD} \leq l_0 \cdot \sin(\beta), \tag{4-19}$$

where β is the pre-defined spring landing angle, and we have met the necessary condition to enter stance phase. For the next flight phase, the transition can only occur if two conditions are met [55]: (i) the horizontal velocity at lift-off (LO) must be positive, i.e. the locomotor is moving forward with:

$$\dot{x}_{LO} > 0, \tag{4-20}$$

and (ii) the apex height of the model is sufficient to facilitate the next touchdown at the prescribed landing angle β, i.e.

$$y_{LO} + \frac{\dot{y}_{LO}^2}{2 \cdot g} > l_0 \cdot \sin(\beta). \tag{4-21}$$

With the dynamic model and conditions for the transition between phases established, the model was built in MATLAB SIMULINK ver. 9.1, with locomotion experiments allowed to run until a stop condition was met. For unstable locomotion, i.e. where it was detected that either of the conditions described by **Equation (4-20)** or **Equation (4-21)** were not satisfied at lift-off, the simulation would end. The other stop condition was that a sufficiently large number of steps had been made to consider the locomotion stable. For this number, 24 successful steps is considered stable [55, 99, 100], and hence has been applied here, as illustrated in **Figure 4-10**. This establishes the premise of the steps-to-fall analysis, assessing which sets of model parameters yield a sufficient number of steps before falling to indicate long-run stability. Practically, once about 24 steps have been recorded, the locomotion should continue indefinitely, and is therefore stable.

For each set of simulations, biped spring stiffness k_{biped} was set to a fixed value, along with touchdown velocity v_{TD}. Touchdown velocity angle of attack, or simply touchdown angle, α and spring landing angle β were then varied independently

from 0° to 90° in 1° increments. Between each set of simulations, the biped spring stiffness $k_{biped} = 2 \cdot k_e$ was then varied from the 0.0 A to 2.0 A measured values of **Table 4-1** for the 10.0 mm deflection case. While the 15.0 mm case could be included, identical trends as stiffness is reduced would be observed, so it would not reveal much. Independent of spring stiffness, touchdown velocity v_{TD} was also varied from 1 m/s to 5 m/s, as a reasonable range of locomotion speeds. The completed analysis includes the number of steps for a total of 231,868 locomotion trials.

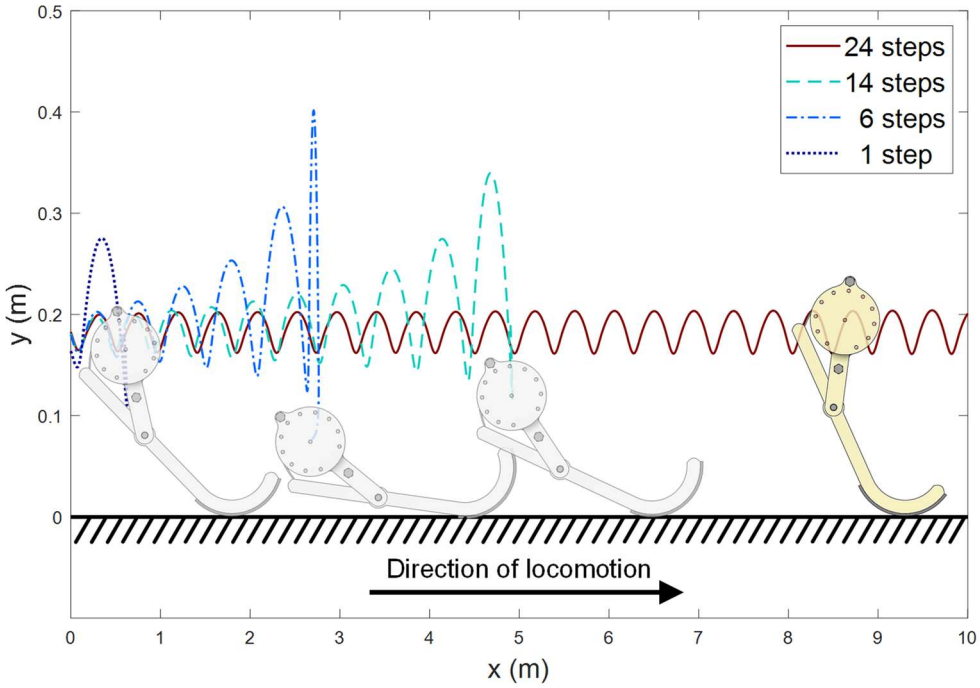

Figure 4-10 Simulated stable (steps ≥ 24) and unstable (steps < 24) SLIP locomotion.

4.5.2 Locomotion Simulation Results

Shown in **Figure 4-11** are the compiled results from the SLIP locomotion simulations. Along the columns of the subplots (1-4) are the results for the range of MRVSAL-II leg stiffness k_e achievable for 0.0 A to 2.0 A of damper current. Each row (a-g) corresponds to a fixed touchdown velocity v_{TD} over the 1 m/s to 5 m/s set range. Each subplot includes the 0° to 90° range of landing angle β and touchdown angle α as the x- and y-axes, respectively. The colour bar indicates the number of steps, i.e. strides, in each heatmap that the locomotor can make before meeting a stop condition of failure or stability. In the case where the initial conditions were unable to

satisfy the requirements to begin a single stride, 0 steps were recorded, making up the vast white regions in the heatmaps. These cases will be considered as invalid trials for the remainder of this discussion. Cases with at least 1 step will, as such, be referred to as valid trials. As stated earlier, cases with 24 steps are taken as stable trials with sustained continuous locomotion.

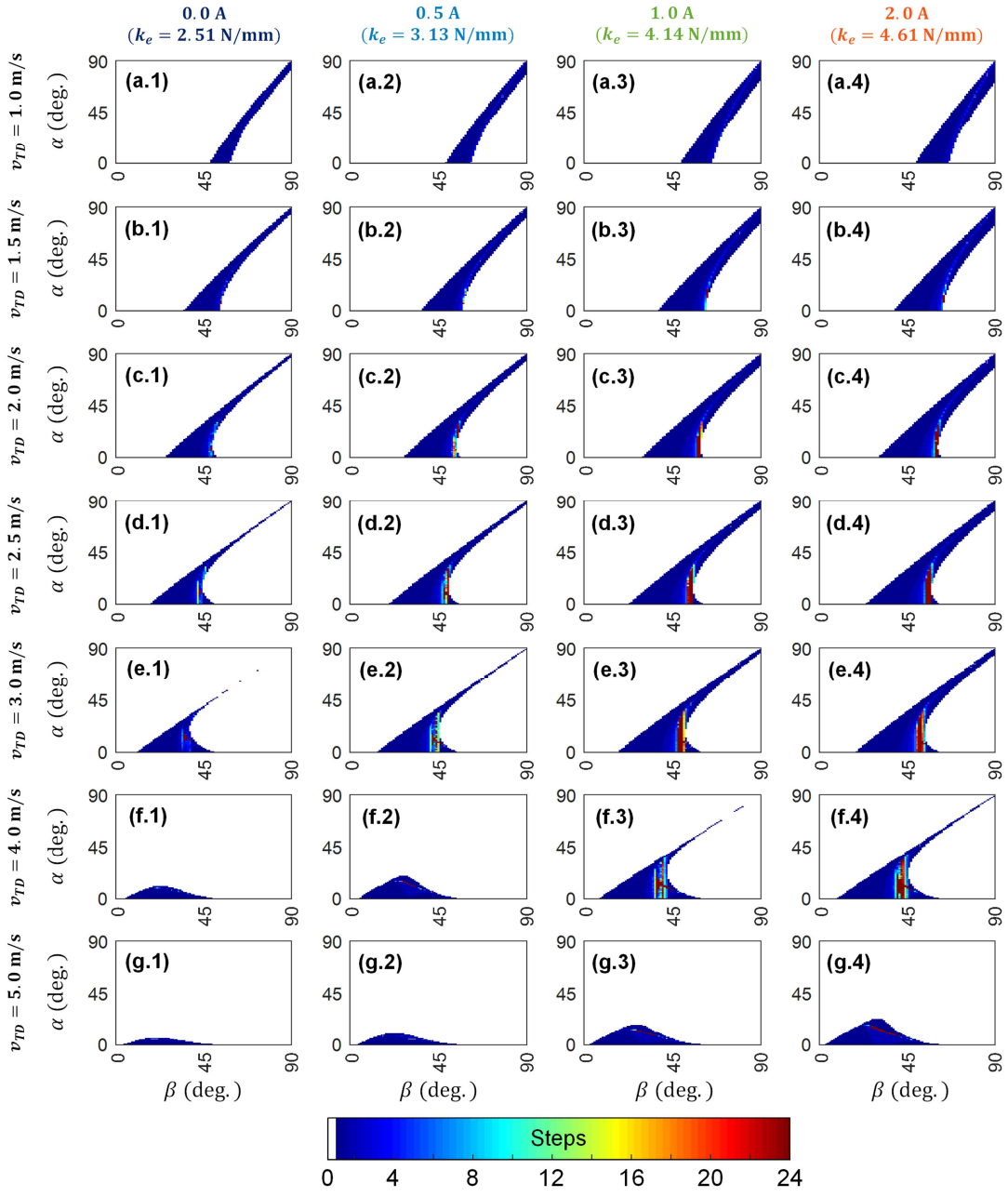

Figure 4-11 Steps-to-fall analysis of SLIP model with characteristic leg spring of stiffness (a.1)-(g.1) $k_e = 2.51$ N/mm, (a.2)-(g.2) $k_e = 3.13$ N/mm, (a.3)-(g.3) $k_e = 4.14$ N/mm, and (a.4)-(g.4) $k_e = 4.61$ N/mm.

Showing similarity to the steps-to-fall results presented in [55], the following trends are observed here. (i) For a fixed stiffness, there is a tendency to increase the area of the valid-trial region with increase in touchdown velocity to a peak of around 2.0 m/s to 2.5 m/s, before decreasing again with higher speeds. While this eventual decrease was not observed in [55], the normalised touchdown velocity was confined to less than half the selected range studied here. (ii) Following a similar trend, the stable locomotion trials tend to increase in range of both touchdown angle and landing angle up to a touchdown velocity of around 3.0 m/s, before decreasing again with high touchdown velocities. This is indicative of an optimal touchdown velocity to maximise the variation in both touchdown angle and landing angle. Interestingly, unlike the wide range of suitable touchdown angles for stability around the mid-range of touchdown velocities, e.g. as in **Figure 4-11(d.4)**, towards higher touchdown velocities, this range is reduced with the range of suitable landing angles expanding significantly, e.g. as in **Figure 4-11(g.4)**. However, this stability becomes very sensitive to the selection of touchdown angles. (iii) Generally, for a given touchdown velocity, the region of suitable landing angles tends to increase, i.e. shift to the right, with leg stiffness, simultaneously increasing in allowable range. This behaviour is apparent when observing **Figure 4-11(d.1)** to **Figure 4-11(d.4)**, for example. Beyond these three trends found in the results, it can also be seen that while the landing angle can provide the system with stability between about 30° to 60°, stable touchdown angles exist from about 0° to 30° over a similarly sized range.

To further compare the stability variation for different leg stiffnesses, **Figure 4-12** plots the percentage of valid locomotion trials for these different stiffnesses against touchdown velocity. As indicated by the trends observed in **Figure 4-11**, we find in **Figure 4-12** a peak in valid trials for the different stiffnesses around touchdown velocities of 2.0 m/s to 2.5 m/s. It becomes evident here that the softest 0.0 A case enables the fewest valid locomotion trials for the system, with at most 9.26% of the set, occurring at a 2.0 m/s touchdown velocity. The stiffest 2.0 A case conversely yields the most valid trials, reaching a peak of 16.1% at a 2.5 m/s touchdown velocity.

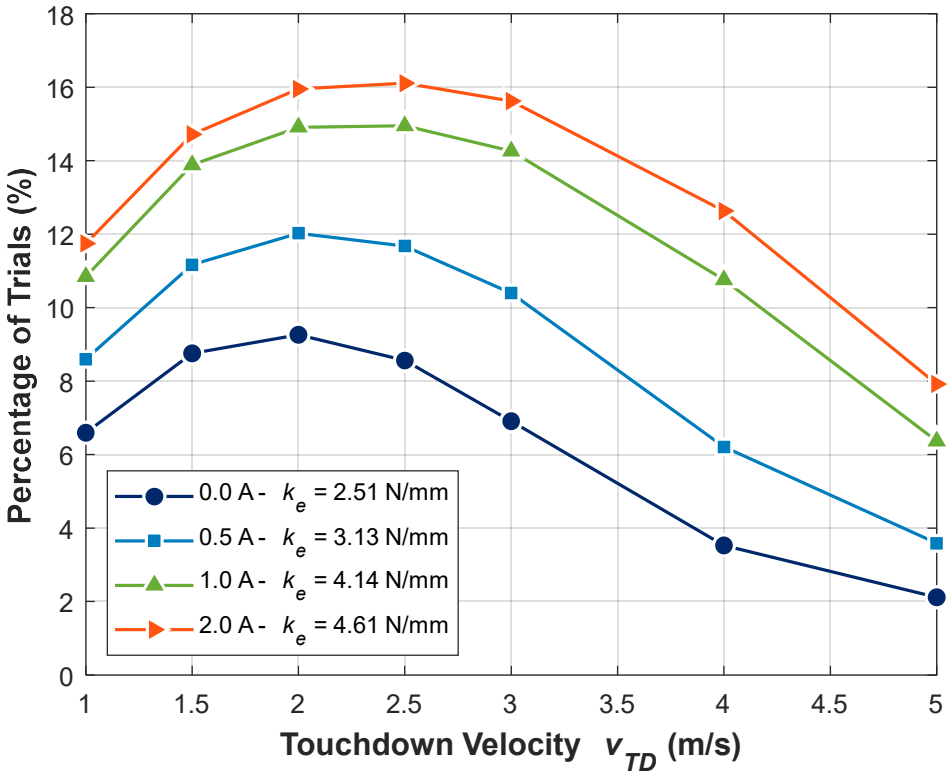

Figure 4-12 Percentage of valid SLIP locomotion trials.

The subset percentages of stable locomotion trials are plotted in **Figure 4-13**, which reveals that the peak stable trials occur over a wider range of touchdown velocities, starting from 2.5 m/s for the 0.5 A case, up to 4.0 m/s for the 2.0 A case. Where the peak percentage of stable trials is found for the 0.0 A case to be 1.75% at a 3.0 m/s touchdown velocity, the largest peak occurs at the same velocity for the 1.0 A case with 7.54%. This represents a 331% increase in the number of stable and valid trials achievable for the various combinations of touchdown angles and landing angles at this touchdown velocity. In terms of the absolute number of stable trials, i.e. considering invalid trials as well, the 1.0 A case results in a 790% increase when compared with the 0.0 A case. While the softer cases should generally be avoided here for stability over the entire touchdown velocity range, the results indicate careful attention should be paid to the selection of leg stiffness for system stability. That is, once adequately stiff, the leg stiffness should be controlled to maximise locomotion stability for the system.

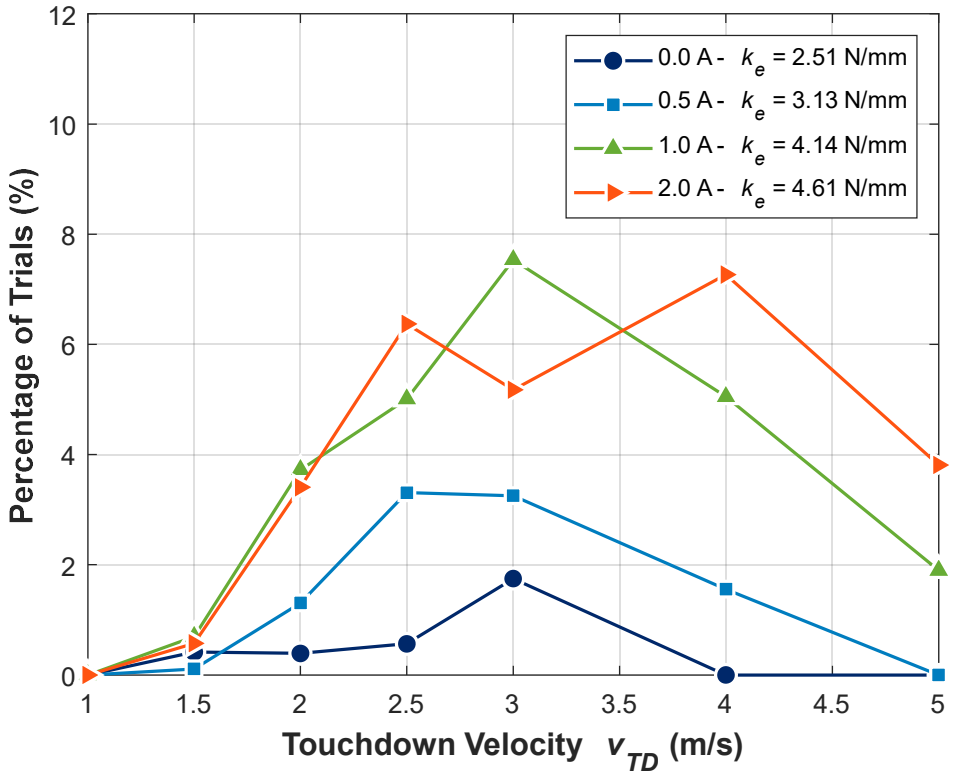

Figure 4-13 Percentage of stable SLIP locomotion trials.

4. 6 Chapter Summary

An MRF-based variable stiffness actuator leg was designed and prototyped in this study to improve over previous variable stiffness leg designs, improving leg balance during actuation to reduce energy cost. Through compression testing, later verified through mathematical modelling and simulation, the MRVSAL-II was shown to be capable of up to a 114% increase in stiffness, attributable to the rotary MR damper based variable stiffness mechanism. Employing the SLIP locomotion model, continuous running simulations were conducted to investigate the change in stability due to variable stiffness through steps-to-fall analysis. It was shown that for the stiffness range achieved by the MRVSAL-II, a bipedal legged robot would see improved stability through variable stiffness, where a peak of 7.54% of valid trials were stable, achieved with 1.0 A current at a 3 m/s touchdown velocity. While the percentage of valid trials seems quite small, this is representative of a 790% increase in the range of stable combinations of touchdown angle and landing angle, due to the appropriate adjustment of leg stiffness.

5 REAL-TIME ADAPTIVE LEG-STIFFNESS FOR ROLL COMPENSATION VIA MAGNETORHEOLOGICAL CONTROL IN A LEGGED ROBOT

5. 1 Introduction

Real-time adjustment of leg stiffness may play a key role in disturbance rejection during locomotion, with humans changing effective leg stiffness in response to known or unknown changes in terrain stiffness while running and hopping [11, 15]. Similarly, biological species may make leg stiffness adjustments when encountering an obstacle (increase in elevation) or a valley (decrease in elevation), depending on context and leg morphology [16, 17]. For this to be feasible in legged robots, the ability to rapidly adjust leg stiffness upon a step is paramount. MRF can achieve this more robustly than MRE [62], also with a response in the order of milliseconds [64]. As such, the MRVSAL-II has been applied here to investigate such scenarios.

Where monopedal [28, 48, 63] or bipedal [8] constrained locomotion platforms have been employed in robot leg studies, these have varying DOF. Particularly for linear locomotion along a fixed distance, these test systems often restrict roll, pitch,

and yaw motion, only allowing movement along the coronal-axis [8, 28]. Where these systems are beneficial is in the repeatability of experiments, with less dynamic variation to be concerned with. This has readily allowed for observation of the influence that various terrain variables have on locomotion [8], as well as the influence of different control approaches [28]. What has not been explored before due to such DOF constraints and frequent use of monopedal platforms, however, is the potential variable stiffness may have to offer when legged robots experience disturbances such as obstacles and valleys, or coronal gradients.

By removing the roll-angle constraint of the bipedal robot test platform first presented in **Chapter 3**, the MRVSAL-II is experimentally studied during locomotion with extended DOFs. Beyond passive stiffness control modes, a real-time adaptive stiffness controller is put forward to mitigate coronal disturbances. Extensive locomotion studies are then carried out to investigate performance improvements the leg may offer in these different modes through encounters with obstacles, valleys, and coronal gradients. The potential for resonant locomotion is also revisited for the MRVSAL-II.

5. 2 Locomotion Experimental Setup

5.2.1 Test-Platform Design and Control

In order to characterise the dynamic performance of the MRVSAL-II, the locomotion test rig of **Chapter 3** under **Section 3.4** was upgraded to facilitate 'extended' planar locomotion, with a bipedal torque-actuated test platform that is restrained to move only through the sagittal plane. The motion restricts COM movement through the transverse and coronal planes but is extended to allow for rotation about the coronal- or x-axis, i.e. roll ϕ. Pitch and yaw of the test platform are also constrained, vastly simplifying the analysis and control effort. The test rig, shown in **Figure 5-1**, features an easily adjustable aluminium extrusion frame. The robot platform, of total moving mass m_{biped} = 15.2 kg, follows vertical and horizontal rails, connected through a guide carriage, which constrains the platform on a central shaft, facilitating the desired motion. The system is controlled by an NI myRIO-1900, capable of real-time control and data acquisition. Regarding sensory equipment, coronal- or x-axis displacement is measured by a SICK DT60-P211B laser (5100 mm range) and a MIRAN MPS-S-200-V1 draw-wire displacement sensor is used to

measure transverse- or *y*-axis displacement (200 mm range). For simplicity, these axes are defined as horizontal and vertical, respectively. To measure the remaining DOF, i.e. roll-angle, a BI Technologies 6127-V1-A180-L.5 non-contact potentiometer (180° range) is mounted to the guide carriage assembly. To actuate the legs of the platform, two AC synchronous motors (Panasonic 1.3 N·m MSMJO42G1U, with MBDKT2510CA1 200 V driver) are coupled to 10:1 planetary reduction gearboxes, giving a maximum output torque of 13 N·m to the legs. These motors also serve to measure the leg torque and angular velocity.

To initialise the system, a computer-based user interface enables the initial leg position to be set, which in this study is -15° clockwise rotation from alignment of the upper leg segment to the *y*-axis. For each step, as illustrated in **Figure 5-2**, the legs rotate synchronously between two phases: stance phase, and flight phase. During flight, a high leg-speed of 30 rad/s is set for rapid return and the stance leg-speed is varied between test runs from 0.5 rad/s up to 5 rad/s. During locomotion, the continuous unidirectional rotation of the legs propels the robot platform forward for up to 1000 mm runs with a fixed number of steps, which is typically two or three per run. This was found to improve repeatability between trials when compared with the fixed distance locomotion of **Chapter 3** in **Section 3.4**. In each case, every test run was repeated five times to improve the reliability of the results. As shown in **Figure 5-3**, these test runs may be over obstacles, valleys, coronal gradients, or unobstructed flat terrain. While running, leg stiffness may then be passively set, or adaptively controlled in order to compensate for such conditions.

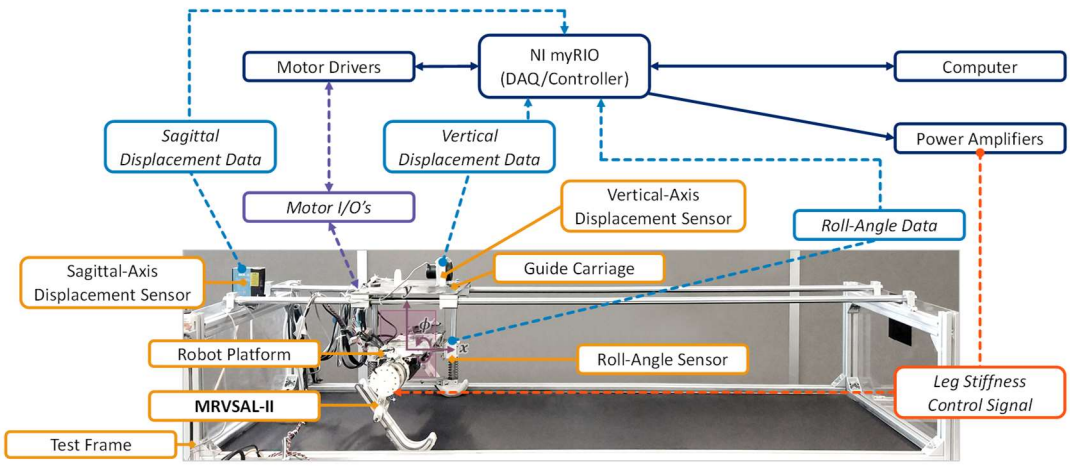

Figure 5-1 Improved limited-DOF bipedal locomotion experimental setup.

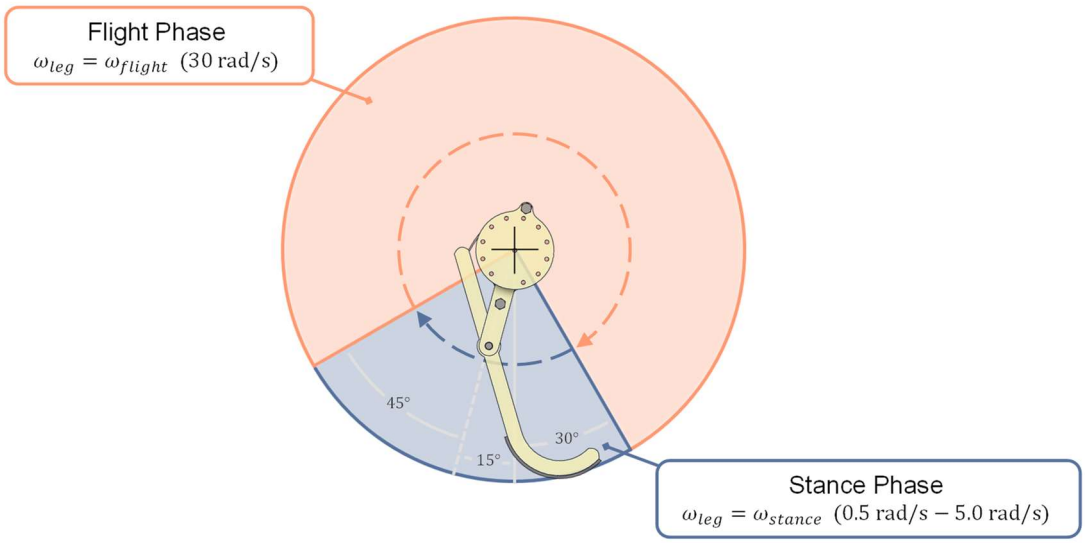

Figure 5-2 Locomotion phases during unidirectional torque actuation.

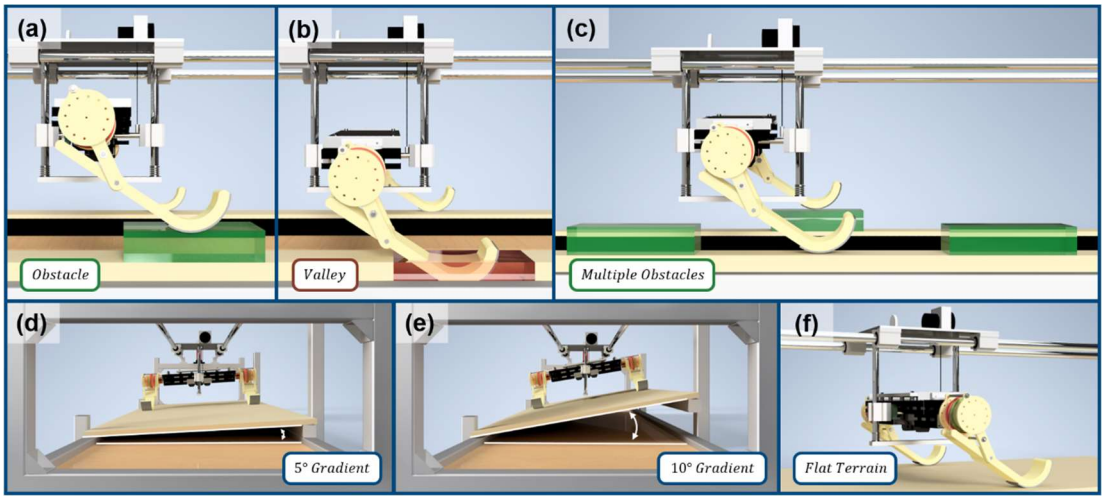

Figure 5-3 Locomotion test scenarios with (a) one asymmetric obstacle, (b) one asymmetric valley, (c) multiple asymmetric obstacles, (d) 5° coronal gradient, (e) 10° coronal gradient, and (f) unobstructed flat terrain.

5.2.2 Stiffness Control Modes

Within this study, two alternative control modes for leg stiffness were employed: adaptive-stiffness roll compensation, and passive stiffness. In either case, to conserve energy and reset the leg deflection, the MR damper current is toggled to a 0 A current during the flight phase. Why this adaptive mode should be considered is that legged locomotive robots may suffer increased energy consumption and can be pushed to unstable levels of roll if subjected to disturbances which cause the platform to rotate about the coronal-axis, e.g. if one leg of a bipedal robot encounters variations

in elevation or a change in terrain stiffness. To provide adaptive compensation for this while the robot is running and in the stance phase, MRVSAL-II stiffness can be controlled to reduce the magnitude of the roll angle ϕ of the robot platform. This is achieved by setting relatively high stiffness for the leg experiencing relatively lower elevation, which may identically be applied to lower stiffness terrain. Based on this concept, the control algorithm applied in this study follows the IF-THEN logic outlined in **Figure 5-4**, where $k_{leg,R}$ and $k_{leg,L}$ are the respective right leg and left leg effective stiffnesses.

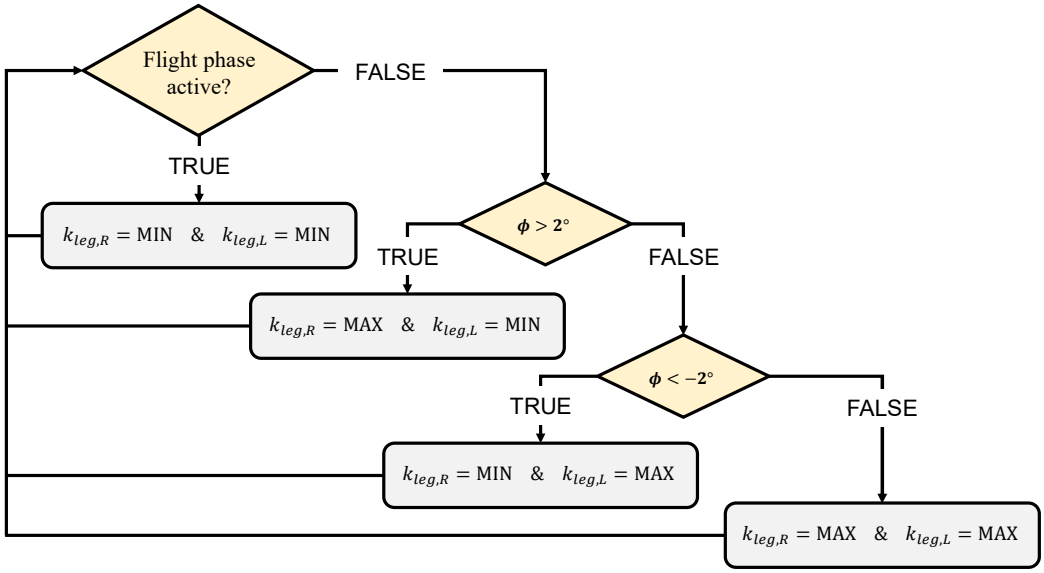

Figure 5-4 Adaptive stiffness control algorithm process flow diagram.

In terms of control current during the stance phase, MAX corresponds to 2 A stiffness, and MIN to 0 A stiffness. For general observations and comparison with the adaptive controller, leg stiffnesses may be held constant throughout runs, although still toggled to 0 A during flight phases. To illustrate this functionality, **Figure 5-5(a)** includes the roll angle, i.e. control input, for a test run in the asymmetric obstacle case with a 2 rad/s stance leg-speed. When the roll angle of the adaptive control case exceeds -2° and the platform is in the stance phase, as seen in **Figure 5-5(b)**, the right leg damper current will be set to 0 A (MIN) to soften this leg, while the left leg would remain at 2 A (MAX). Similarly, if the roll angle were to exceed 2°, the left leg damper current would be set to 0 A (MIN), with the right leg set to 2 A (MAX). It should also be noted that for clarity in the figure, the left leg damper current has been excluded,

and is simply the opposite level to the right leg damper current during stance phase when the ±2° threshold is exceeded.

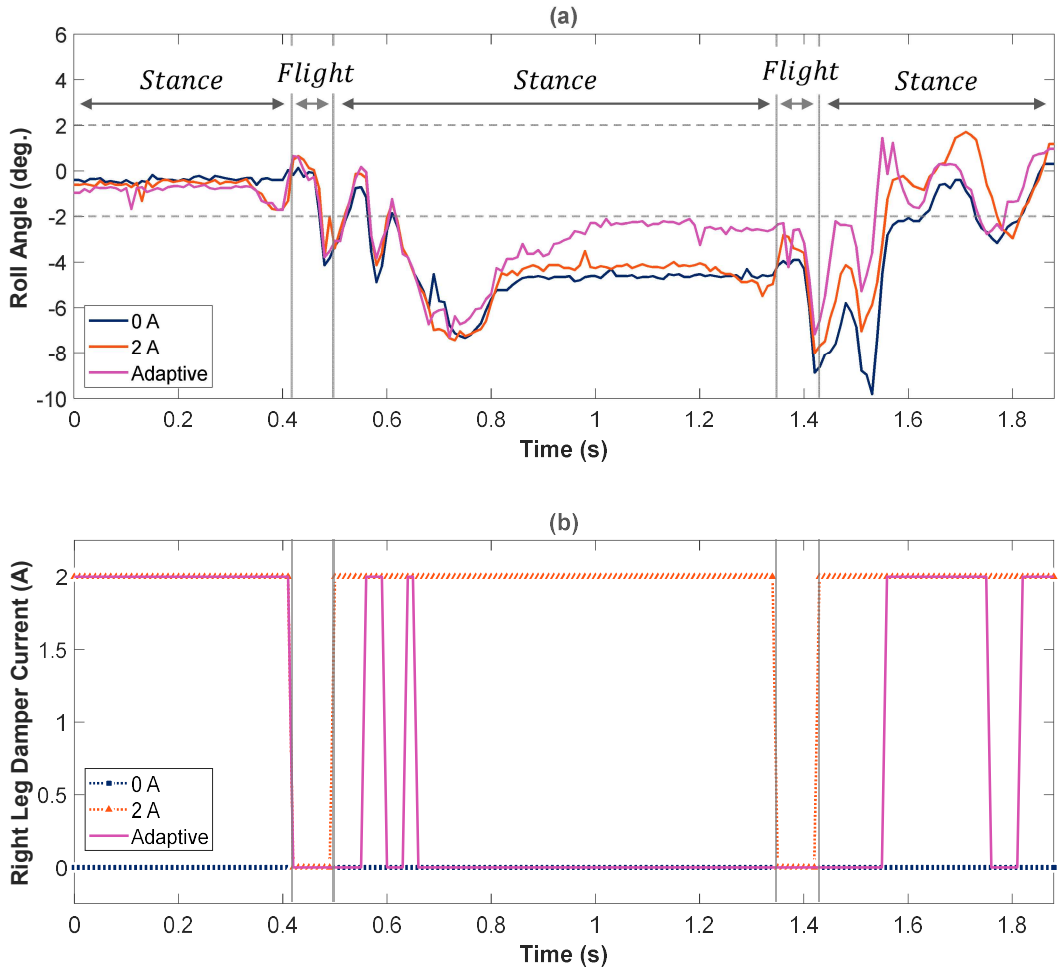

Figure 5-5 Asymmetric obstacle 2 rad/s leg speed (a) roll angle, and (b) right leg damper current.

5. 3 Obstacle and Valley Disturbance Mitigation

A common occurrence for legged locomotors is encountering a relative increase in elevation below one leg (or leg set), i.e. an obstacle. Similarly, a decrease in elevation, i.e. a valley, may be encountered. This locomotion over uneven terrain causes increased energy cost [103] and may not be an isolated occurrence, taking place several times over broken-up uneven terrain. For some biological species, upon encountering these disturbances to locomotion, immediate leg stiffness modulation is observed during compensation efforts [16]. As such, in this study three scenarios were investigated with each disturbance asymmetric about the sagittal plane: a single obstacle encountered by one leg (**Figure 5-3(a)**), a single valley encountered by one

leg (**Figure 5-3(b)**), and 3 obstacles encountered by alternating legs (**Figure 5-3(c)**). Each obstacle or valley is 45 mm in height, which represents about 20% of the leg-to-hip height of the robot platform in the initial stance position. For each stance leg-speed tested, the disturbance is repositioned along the horizontal axis to ensure appropriate interaction with the leg. This adaptive control mode was compared against both the soft 0 A and stiff 2 A passive control modes. For all tests, the MCOT was considered to purely assess the contribution of stiffness control to locomotion cost, making use of **Equation (3-18)**. As before, P_{avg} is the average power for two legs as determined from elementwise multiplication of leg torque T_{leg} and leg speed ω_{leg} time-trace data collected during test runs, m_{biped} is the total moving mass of the platform and carriage, and v_{avg} is the horizontal velocity averaged over the entire run. Some kinematic and dynamic measurements are also included for discussion where relevant, with all summarised data reported using error-bar plots.

First, for the asymmetric obstacle test scenario of **Figure 5-3(a)**, two steps were taken in each run, the first of which including a right-leg collision with the obstacle. From **Figure 5-6(a)**, we can see the adaptive control mode tracks quite close to the stiff 2 A passive mode in contrast to the soft 0 A setting. However, the adaptive mode is surpassed in performance by the 2 A passive mode at the MCOT minimum of 0.93 at 2 rad/s stance leg-speed. Here, and MCOT of 1.08 is found for the adaptive mode, representing a 16.1% greater energy cost at this speed. This, however, is less severe than the 0 A MCOT of 1.24, representing a 33.3% greater cost. These results align with the expectations from the average horizontal velocity and average leg torque of **Figure 5-6(b)** and **(c)**, respectively. Here we find the adaptive velocity approaches that of the 2 A mode, but is generally lower, while the leg torque is similar and, in some cases, higher.

As we see in **Figure 5-6(d)**, however, the adaptive control results in an improved vertical displacement range, lower than the 2 A mode at all leg speeds, with the largest difference occurring at 2 rad/s where the 91.5 mm adaptive range represents a 15.0% reduction from the 108 mm 2 A range. While the 0 A mode shows a much lower range in vertical displacement, as low as 49.8 mm at 5 rad/s leg speed, adaptive control shows its key benefit in **Figure 5-6(e)** and **Figure 5-6(f)**, wherein peak (magnitude) and root mean square (RMS) roll angle is reported, respectively. Across all test speeds, adaptive control maintains the lowest peaks here, given this should come as a direct

consequence of the adaptive mode's control target. In terms of the largest difference from a passive mode, at 5 rad/s, the adaptive peak roll angle was found to be 7.12°, a 36.7% reduction from 11.3° for the 0 A mode. Similarly, the adaptive control RMS roll angle at this leg speed showed a 33.6% reduction from 4.50° for the 0 A mode down to 2.99°.

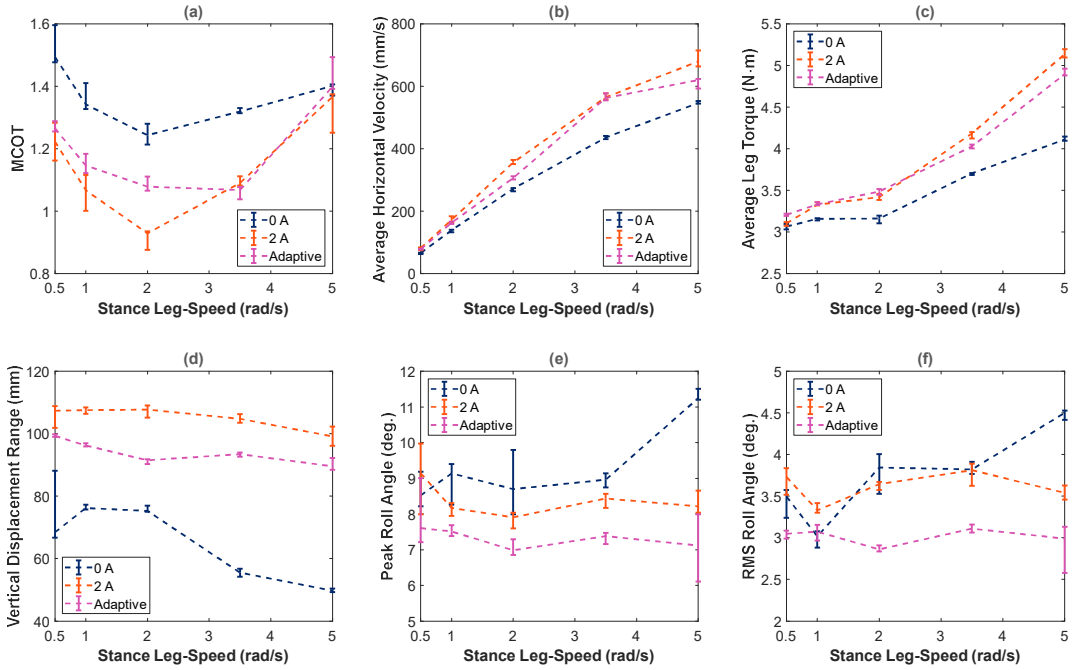

Figure 5-6 Asymmetric obstacle (a) MCOT, (b) average horizontal velocity, (c) average leg torque, (d) vertical displacement range, (e) peak roll angle, and (f) RMS roll angle.

To better visualise the influence of this roll angle, **Figure 5-7** shows the time-trace of the vertical position of the robot platform for a 2 rad/s stance leg-speed run. Shown for each control mode is the COM position, left leg position, and right leg position. During the stance phase where obstacle collision occurs, i.e. from 0.50 s to 1.35 s, we can observe that the 0 A and 2 A passive modes of **Figure 5-7(a)** and **(b)**, respectively, tend to suffer a greater range of motion between both legs when compared to the adaptive control mode of **Figure 5-7(c)**. Following the collision in the next stance phase, improved recovery from this disturbance is also observed for the adaptive control mode when compared against the two passive modes.

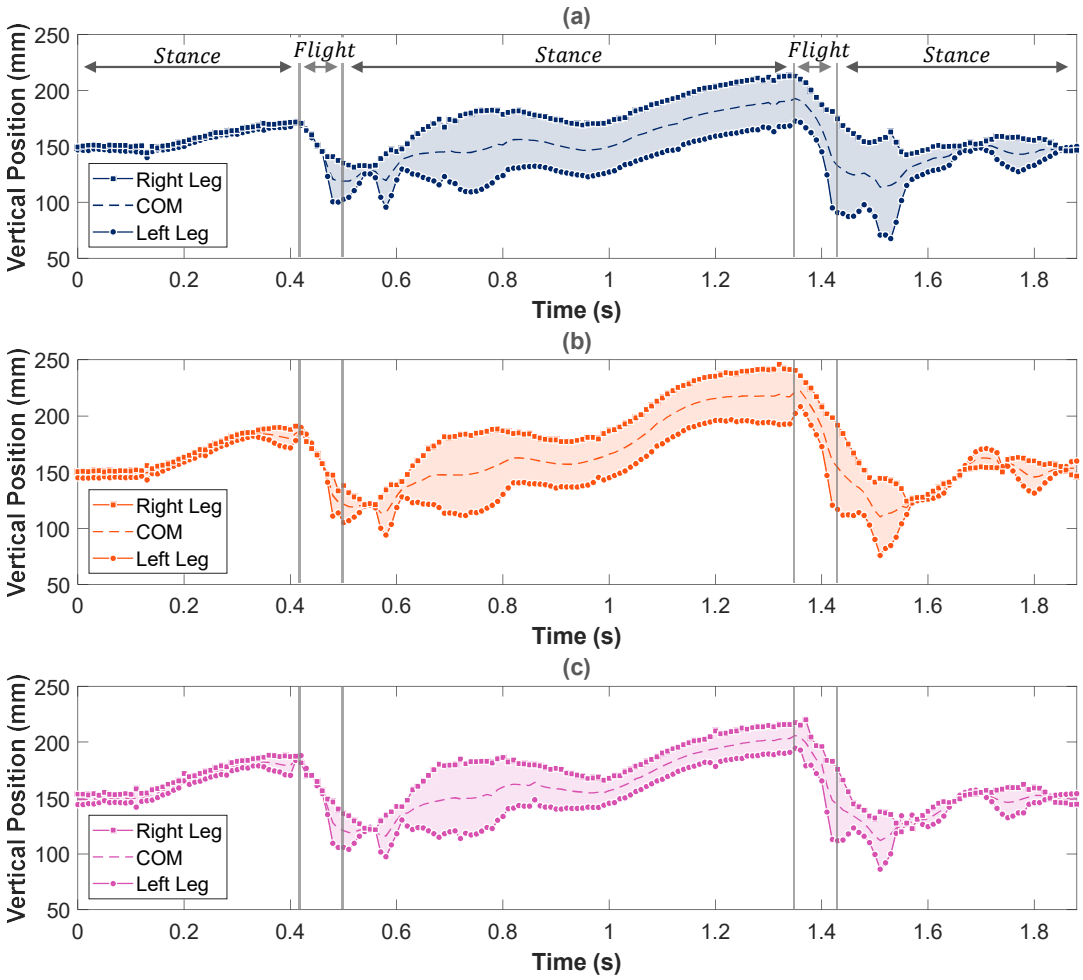

Figure 5-7 Asymmetric obstacle platform vertical position at 2 rad/s leg speed with control mode (a) 0 A passive, (b) 2 A passive, and (c) adaptive.

In the asymmetric valley test scenario of **Figure 5-3(b)**, similar to the obstacle scenario, two steps were taken, with the first step including interaction with the valley. Here, we find quite similar performance to the obstacle scenario in terms of MCOT and average horizontal velocity, seen in **Figure 5-8(a)** and **(b)**, respectively. In this case, the minimum MCOT is once again found for at 2 rad/s for the 2 A passive control mode, at a magnitude of 1.19. Although an identical minimum is found for the adaptive control mode at 3.5 rad/s of 1.23, which represents the minimum across all modes at this leg speed, and a 4.65% improvement from the 2 A MCOT of 1.29 at the same speed. This is likely due to the substantial increase in leg torque for the 2 A mode along with leg speed, as observed in **Figure 5-8(c)**. In contrast, the adaptive control mode follows similar, albeit slightly higher leg torque to the 0 A mode.

Again, we can observe generally smaller variation in vertical displacement overall for the 0 A mode, with the adaptive control, however, still showing improvement over the 2 A mode. For the peak and RMS roll angles of **Figure 5-8(e)** and **(f)**, we once again find the adaptive control mode to generally yield the best result, with the greatest reduction in peak roll angle occurring at 3.5 rad/s from the 2 A case at 6.46° by 25.2% down to 4.83° for the adaptive control mode. Unlike in the obstacle scenario, the greatest improvement in RMS roll angle occurred at a different leg speed to the peak, although again occurring at 5 rad/s, showing a 34.5% reduction from 2.29 in the 2 A mode to 1.50 in the adaptive mode.

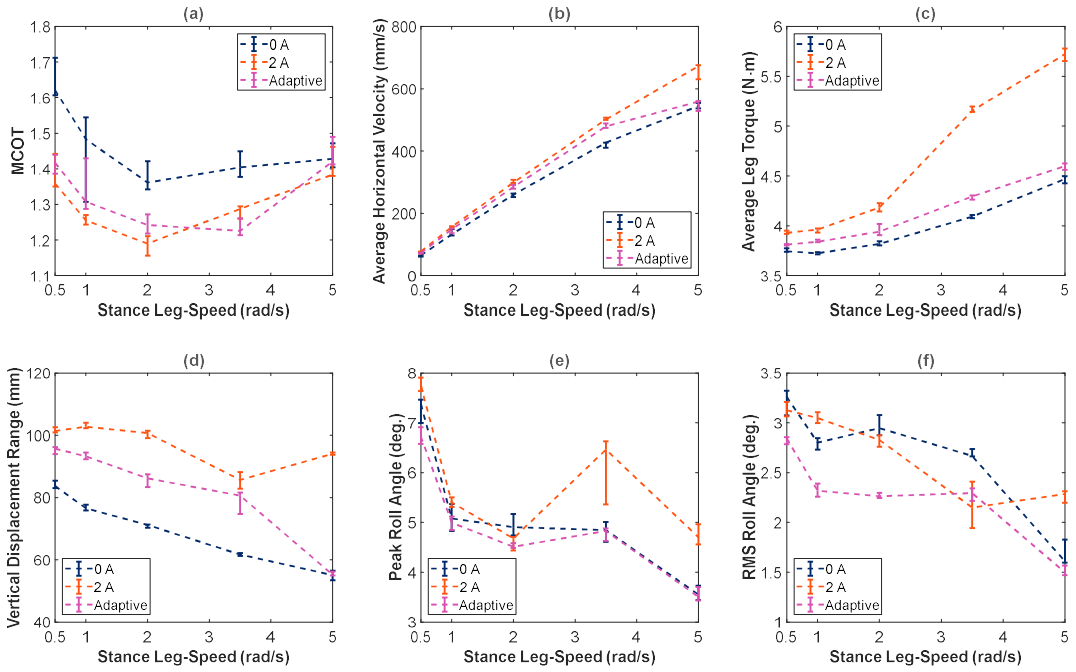

Figure 5-8 Asymmetric valley (a) MCOT, (b) average horizontal velocity, (c) average leg torque, (d) vertical displacement range, (e) peak roll angle, and (f) RMS roll angle.

The remaining test scenario of this type, three obstacles encountered by alternating legs, as in **Figure 5-3(c)**, was conducted over a smaller range of leg speeds, including only 0.5 rad/s, 1 rad/s and 2 rad/s. This was due to the length limitation of the test frame, given at higher speeds these obstacles could not be adequately repositioned to ensure leg collisions would occur. Unlike the previous scenarios, here we consider three steps during locomotion, each resulting in a collision between a leg and obstacle in an alternating fashion. As observed in **Figure 5-9(a)** to **(d)**, the trends for MCOT, velocity, leg torque, and vertical displacement range are generally similar

to the respective 0.5 rad/s to 2 rad/s results obtained from the single obstacle scenario in **Figure 5-6(a)** to **(d)**. However, the MCOT of **Figure 5-9(a)** for each control mode is larger in all cases, due to the reduced locomotion velocity in **Figure 5-9(b)** and increased leg torque of **Figure 5-9(c)**, as anticipated with more obstacle encounters. Regarding the roll angle, here we find similar improvement through adaptive control over both passive modes, seen in **Figure 5-9(e)** and **(f)**. In terms of the peak roll angle, at best, we find a 27.8% reduction from 10.4° for 2 A to 7.48° for adaptive control occurring at 1 rad/s. For the RMS roll angle, identical improvement is found for both 1 rad/s and 2 rad/s leg speeds, with that of 1 rad/s being 22.7% from 4.62° for 2 A down to 3.57° for adaptive control.

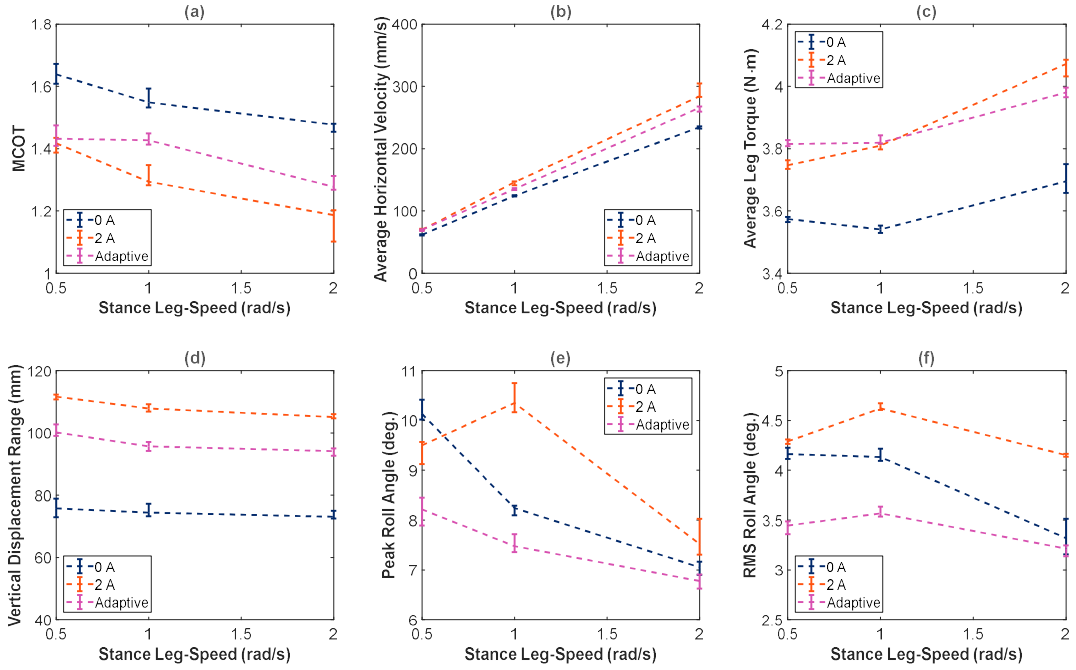

Figure 5-9 Multiple asymmetric obstacles (a) MCOT, (b) average horizontal velocity, (c) average leg torque, (d) vertical displacement range, (e) peak roll angle, and (f) RMS roll angle.

5. 4 Coronal Gradient Compensation

Another scenario which may be encountered during legged locomotion is a continuous terrain gradient along the coronal plane. While discomfort and increased effort to follow a certain trajectory may be experienced by the locomotor, a biological species in this circumstance may be inclined to reduce the length of the leg(s) on the upper slope and increase the length of those on the lower slope. Identically, legs which are desired to be shorter may be adjusted to be softer and legs to be longer, stiffer. As such, the adaptive controller for leg stiffness has also been employed here for testing

during locomotion along 5° (**Figure 5-3(d)**) and 10° (**Figure 5-3(e)**) coronal gradients over a stance leg-speed range of 0.5 rad/s to 5 rad/s, for 2 steps in each test. As before, this adaptive control mode was compared against both the soft 0 A and stiff 2 A passive control modes.

Considering first the 5° coronal gradient of **Figure 5-3(c)**, the results summary for this in **Figure 5-10** is similar to that of the single obstacle scenario in **Figure 5-6** in terms of general trends between control modes. However, we find here a higher uniformity between the results of different control modes than was observed previously. And although **Figure 5-10(a)** shows the 2 A mode to again maintain a lower MCOT, the minimum point is not as distinct. An interesting observation here is that, despite the similarities in locomotion velocity for adaptive control and 2 A passive control in **Figure 5-10(b)**, the leg torque of the two modes are dissimilar, as seen in **Figure 5-10(c)**. In previous single obstacle tests, these were found to be identical in, as seen in **Figure 5-6(c)**. A reasonable explanation is that in this test scenario, given the constant 5° coronal gradient, the robot platform roll angle maintains a set value $\phi > 2°$, which effectively means the upper leg, i.e. left leg, is constantly set to be soft at 0 A, and the lower leg, i.e. right leg, to be stiff at 2 A. With leg torque averaged over each test run, it is now reasonable to find the adaptive control leg torque to be close to the average of the 0 A and 2 A curves in **Figure 5-10(c)**.

With **Figure 5-10(d)** not revealing any new insights, the peak roll angle of **Figure 5-10(e)** surprisingly shows poorer performance of the adaptive control mode for the lower speed tests (0.5 rad/s and 1 rad/s), when compared to the passive modes, which perform similarly across all speeds. It is only toward higher speeds where the peak roll angle is reduced with adaptive control, with a minimum of 6.72° occurring at 5 rad/s leg speed and representing a 17.7% from 8.17° for the 2 A mode. With similar behaviour found in **Figure 5-10(f)** for the RMS roll angle, although with better performance here at lower leg speeds, the best performing control mode is again adaptive, with a 17.6% reduction from the 2 A RMS value of 6.71°, down to 5.53° for adaptive at 5 rad/s leg speed.

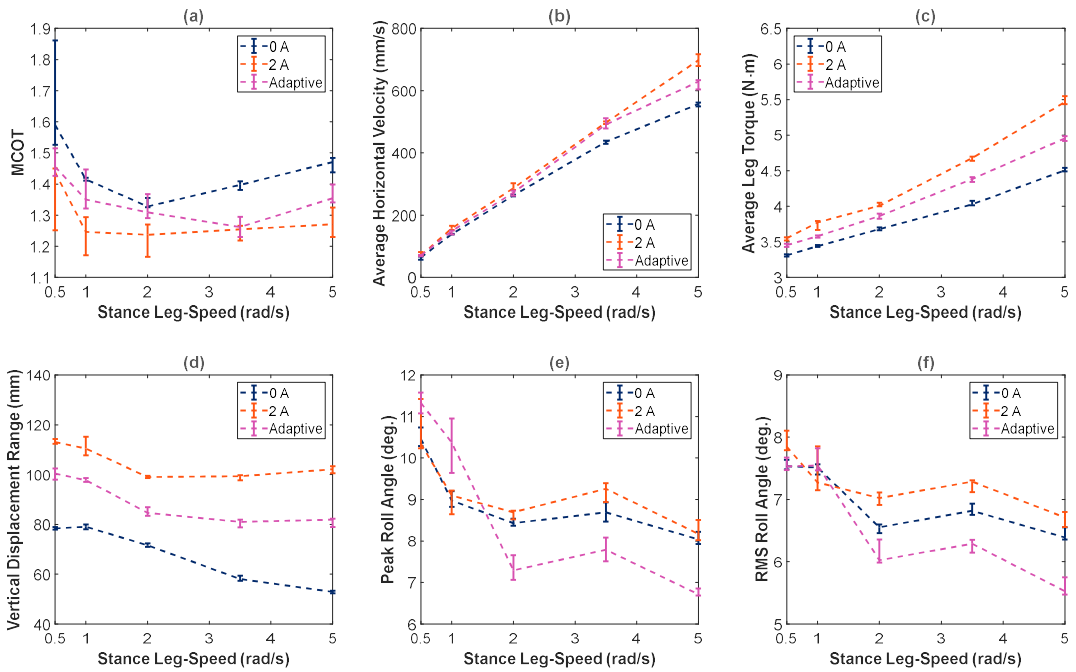

Figure 5-10 Coronal 5° gradient (a) MCOT, (b) average horizontal velocity, (c) average leg torque, (d) vertical displacement range, (e) peak roll angle, and (f) RMS roll angle.

When referring to the 10° coronal gradient of **Figure 5-3(d)**, we find we can make similar generalisations as for the 5° gradient between control modes in the results summary of **Figure 5-11**. Here, as shown in **Figure 5-11(a)**, we find once again that the 2 A mode shows the minimum MCOT amongst the other control modes. When comparing with the 5° gradient, however, we generally find greater energy cost associated with the larger 10° gradient, which, for example in the 2 rad/s leg speed adaptive control case, is 7.94% larger at 1.36 from the previous value of 1.26. And while the locomotion velocity of **Figure 5-11(b)** is similar to that of the 5° gradient in **Figure 5-10(b)**, the adaptive control torque of **Figure 5-11(c)** tends to track more closely to the 2 A mode torque at lower leg speeds, whereas it previously was found to represent more of an average between the 0 A and 2 A modes in **Figure 5-10(c)**. It is also revealed in **Figure 5-11(d)** that vertical displacement range varies less with leg speed with the greater 10° gradient, whereas in **Figure 5-10(d)** there was a clear tendency for this range to decrease at higher speeds. Interestingly, the peak roll angle of **Figure 5-11(e)** shows great variation for the 2 A passive mode, while the adaptive mode tracks quite closely to the 0 A passive mode, with the adaptive mode at best improving over the 2 A case at 5 rad/s leg speed, reducing the roll angle from 15.7° to

13.3°, representing a 15.3% improvement. Similarly, the RMS roll angle in **Figure 5-11(f)** is at best improved by adaptive control at a 5 rad/s stance leg-speed, reducing the angle of the 2 A passive mode by 15.0% from 12.7° to 10.8°. We also find generally better overall performance in terms of RMS roll angle using the adaptive control mode with this larger 10° coronal gradient when comparing with the 5° gradient.

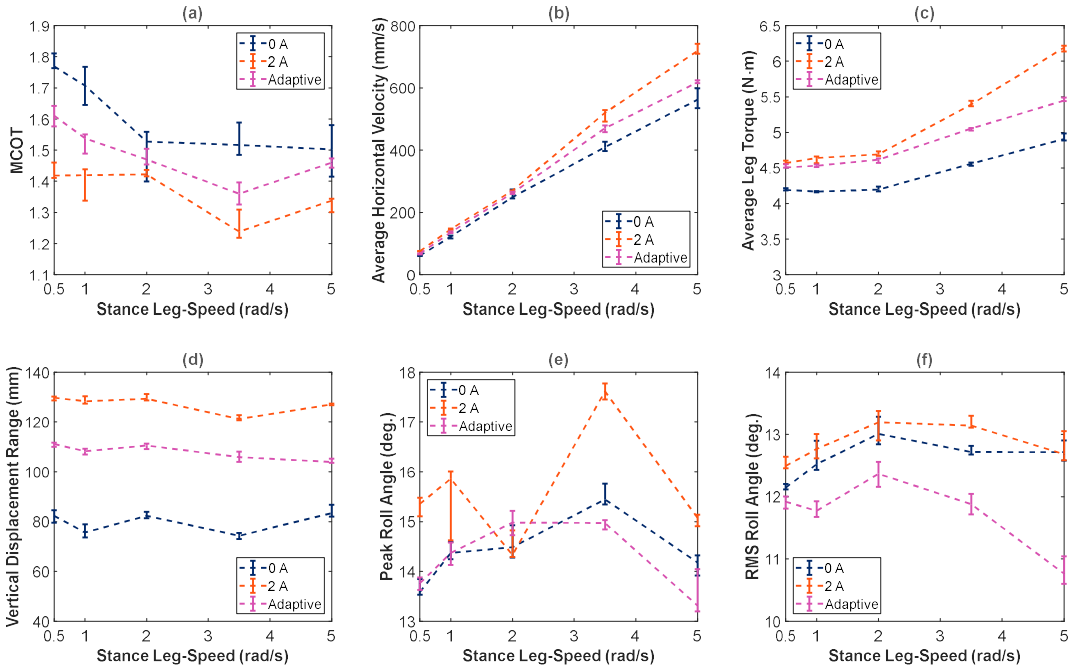

Figure 5-11 Coronal 10° gradient (a) MCOT, (b) average horizontal velocity, (c) average leg torque, (d) vertical displacement range, (e) peak roll angle, and (f) RMS roll angle.

5. 5 Resonant Locomotion

As illustrated in **Figure 5-3(f)**, another area to investigate is the capability of the MRVSAL-II to achieve resonant locomotion, i.e. energy efficient locomotion through tuning of effective leg stiffness. This test mode is also informative of rudimentary variable stiffness behaviour of a test platform equipped with these legs, which can be utilised for control during undisturbed locomotion scenarios. Similar to previous test modes, these locomotion tests were conducted over a 0.5 rad/s to 5 rad/s stance leg-speed range with two steps per run, although in this case with finer incrementation of leg speeds and limited to passive control modes of currents: 0 A, 1 A, and 2 A.

Observed in **Figure 5-12(a)**, the MCOT reaches a minimum for each current and hence stiffness level. With higher stiffness we also generally see a lower overall MCOT curve. This implies the locomotion task benefits from the stiffness increase in

terms of rising locomotion speed, as in **Figure 5-12(b)**, more so than the energy cost associated with rising motor torque of **Figure 5-12(c)**. We also find in **Figure 5-12(d)**, consequent to higher current and hence higher leg stiffness, the vertical displacement range of the COM is increased during the test runs. Interestingly, this does not vary much with leg speed, implying it is somewhat independent of stride frequency during disturbance-free locomotion over flat terrain. Then comparing current levels, although higher current generally results in a higher leg torque, this also leads to higher locomotion speed, hence why the MCOT curves tend to be lower with higher current. In **Figure 5-12(a)**, for the 0 A current, i.e. minimum stiffness, a minimum MCOT is still found and is of mean magnitude 1.10, occurring at 2.25 rad/s stance leg-speed. As anticipated, the leg speed at which this minimum is found for higher current levels or stiffnesses is also higher, being 2.75 rad/s for both 1 A and 2 A currents, with respective magnitudes of 0.95 and 0.82. For the SLIP model [12], the relationship between stride frequency f_s and effective leg stiffness k_e is defined by the equation [104]:

$$f_s = \frac{1}{2\pi}\sqrt{\frac{k_{biped}}{m_{biped}}} \quad \text{[Hz]}, \tag{5-1}$$

where $k_{biped} = 2 \cdot k_e$. Given the increase in leg stiffness over the 0 A to 2 A current range was found to be approximately 100%, depending on leg deflection, we can expect an increase in stride frequency around $\sqrt{2} = 1.41$ times over this range during locomotion. Although a shift this large was not found, i.e. $2.75/2.25 = 1.22$, this is within expectations, given the simplifications made by applying the SLIP model and as leg deflection may vary along with leg speed.

As such, control of damper current and, hence, leg stiffness for different leg speeds could aid the adaptive roll-angle compensation, improving locomotion performance. In particular, it is apparent that during undisturbed locomotion, e.g. when no obstacles, valleys, or gradients are encountered, higher leg stiffness can be employed to increase robot speed and hence reduce mechanical cost of transport. Stiffness may, however, be reduced if improved vertical stability is desired. Comparing these results to those obtained for the MRVSAL-I in **Chapter 3** under **Section 3.4**, we find the MRVSAL-II is capable of much lower MCOT values across

a similar stance leg-speed range. While it was shown there that optimal leg stiffness for reducing MCOT should be varied across different speeds, such behaviour was not observed in this case.

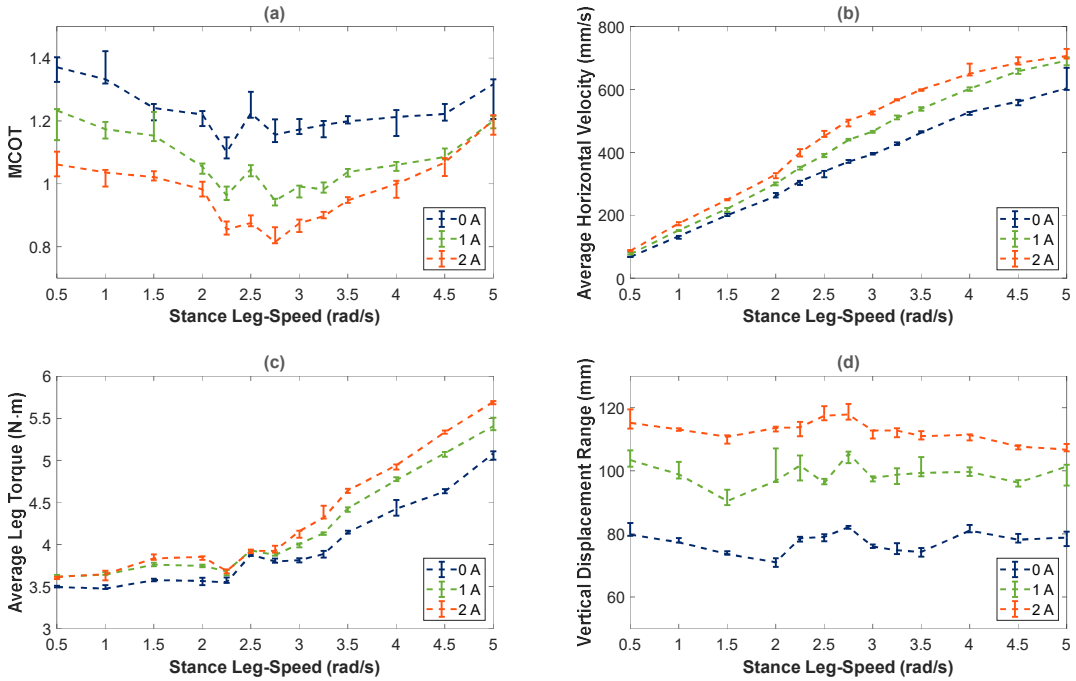

Figure 5-12 Unobstructed flat terrain (a) MCOT, (b) average horizontal velocity, (c) average leg torque, (d) and vertical displacement range.

5. 6 Chapter Summary

With two MRVSAL-II prototypes equipped to a bipedal locomotion platform, extensive locomotion experiments were performed to investigate the benefits of adaptive control of the variable stiffness mechanism with the control target being to reduce roll angle. While passive stiff control of the legs generally showed lower mechanical cost of transport, adaptive control of the legs tended to reduce roll angle, by as much as 36.7%-peak and 33.6%-RMS in asymmetric obstacle tests. Hence this adaptive variable stiffness control contributes to stable locomotion when encountering asymmetric disturbances or coronal gradients. Through resonant locomotion testing, it also was established that the legs generally achieved lower energy cost when stiffer, implying locomotion with the MRVSAL-II could benefit from adaptive control for roll angle compensation, but should otherwise generally stay in a stiff state.

6 SHOCK ABSORPTION FOR LEGGED LOCOMOTION THROUGH MAGNETORHEOLOGICAL LEG-STIFFNESS CONTROL

6. 1 Introduction

Humans and animals make use of so-called ‘preflexes’ and reflexes that modulate effective leg stiffness to manage impacts [1, 11, 105-107]. Despite this, stiffness control in robot legs has not been directly investigated in drop landings within literature. From a biological perspective, modulation of leg stiffness generally precedes disturbances to terrain elevation [16, 102, 108, 109] in order to mitigate injuries to the musculoskeletal system. Other circumstances, such as a variation in terrain stiffness, may also be compensated for through similar modulation [10, 15, 110, 111]. Focussing on the mechanism for impact compensation during drops or jumping in place, studies on humans have been reported for several decades [105, 112-119], with experimental drop heights of up to 1.93 m [112]. While different mechanisms have been attributed to impact-force attenuation during drop jumps or drop landings [115], decreasing effective leg stiffness during an impact has been shown to reduce peak forces [113, 114].

For mechanical shock absorption systems in applications such as motor vehicles or helicopter landing gear, MR materials have been explored widely as potential solutions to shock-induced vibration and impact loads [120-124]. In various real-world scenarios, stiffness control using MR materials could help mitigate costly damages to sensory equipment or prevent complete robot failure. Successful recovery from trivial missteps or more-substantial drops within rugged terrain could be the difference between a successful mission and a failed task for a robot. Although it is clear that the actuators of a robot should be protected from impacts [125], impact loading of robot legs with variable stiffness has not been reported. Hence, it is studied here the extent to which MRF-based leg stiffness control can benefit legged robot shock absorption.

The MRVSAL-II is evaluated through impact loading scenarios, focusing on the potential for variable stiffness in a robot leg to improve shock absorption. First, a drop-test impact loading system is constructed to conduct impact loading experiments. Employing this system, passive performance evaluation is conducted by comparing the MRVSAL-II performance with a comparable rigid leg with high stiffness and damping and a soft leg with low stiffness and damping. Based on experimental performance, an adaptive impact-buffering controller is developed for the MRVSAL-II, which is investigated for its impact mitigation capability.

6. 2 Experimental Setup

To conduct the impact loading experiments of the MRVSAL-II, the drop test system illustrated in **Figure 6-1** was developed. This system makes use of a rigid frame with four parallel 20 mm rails of 1.2 m length. Given the dimensions of the system and leg, a maximum drop height d_{drop} of 600 mm can be set between the foot pad of the leg and impact platform. Two of these rails guide the falling platform to which the leg is rigidly affixed. The platform includes a removable 1.95 kg payload mass, which combines with the platform mass and leg mass to provide adjustable total falling masses m_{total} of 3.05 kg and 5.00 kg for the single leg. To set the drop height of the leg, an electric winch (XBULL3000LBS, X-Bull) is controlled to reach a desired vertical displacement using a laser displacement sensor with 800 mm range (IL-600/IL-1000, Keyence). This laser also serves to measure the displacement d_{COMy} of the falling platform through the impact, which has an initial value of 220 mm at the moment of impact, as illustrated in **Figure 6-2(a)**. A servomotor-controlled release mechanism then allows the falling platform to be dropped upon command. To facilitate leg deflection in the sagittal plane, a low-inertia linear rail platform is located directly below the foot pad of the leg. This rail is supported by two S-type load cells (MT501-100kg, Millennium Mechatronics), from which the measurements can be summed to provide the resulting impact force. This is illustrated between **Figure 6-2(a)** and **(b)**, where it is shown that irrespective of the position of the leg through the deflection, the impact force is always $F_{Ry} = F_{LC} + F_{LC2}$. The included rotary MR damper within the MRVSAL-II is powered with an amplified control signal from the system controller (myRIO-1900, National Instruments), which additionally acts as the DAQ for data logging.

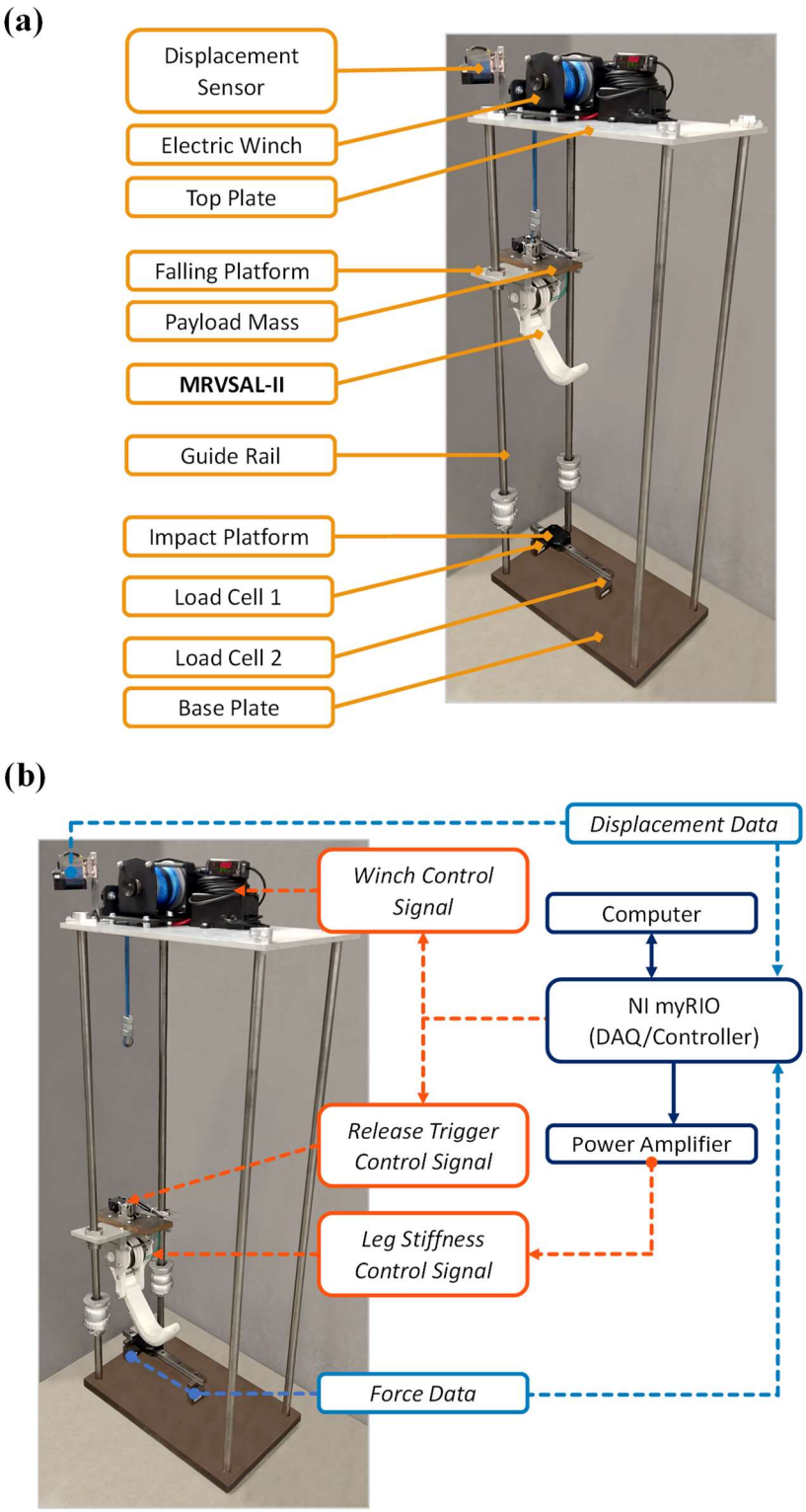

Figure 6-1 Impact loading experimental setup (a) layout, and (b) control system.

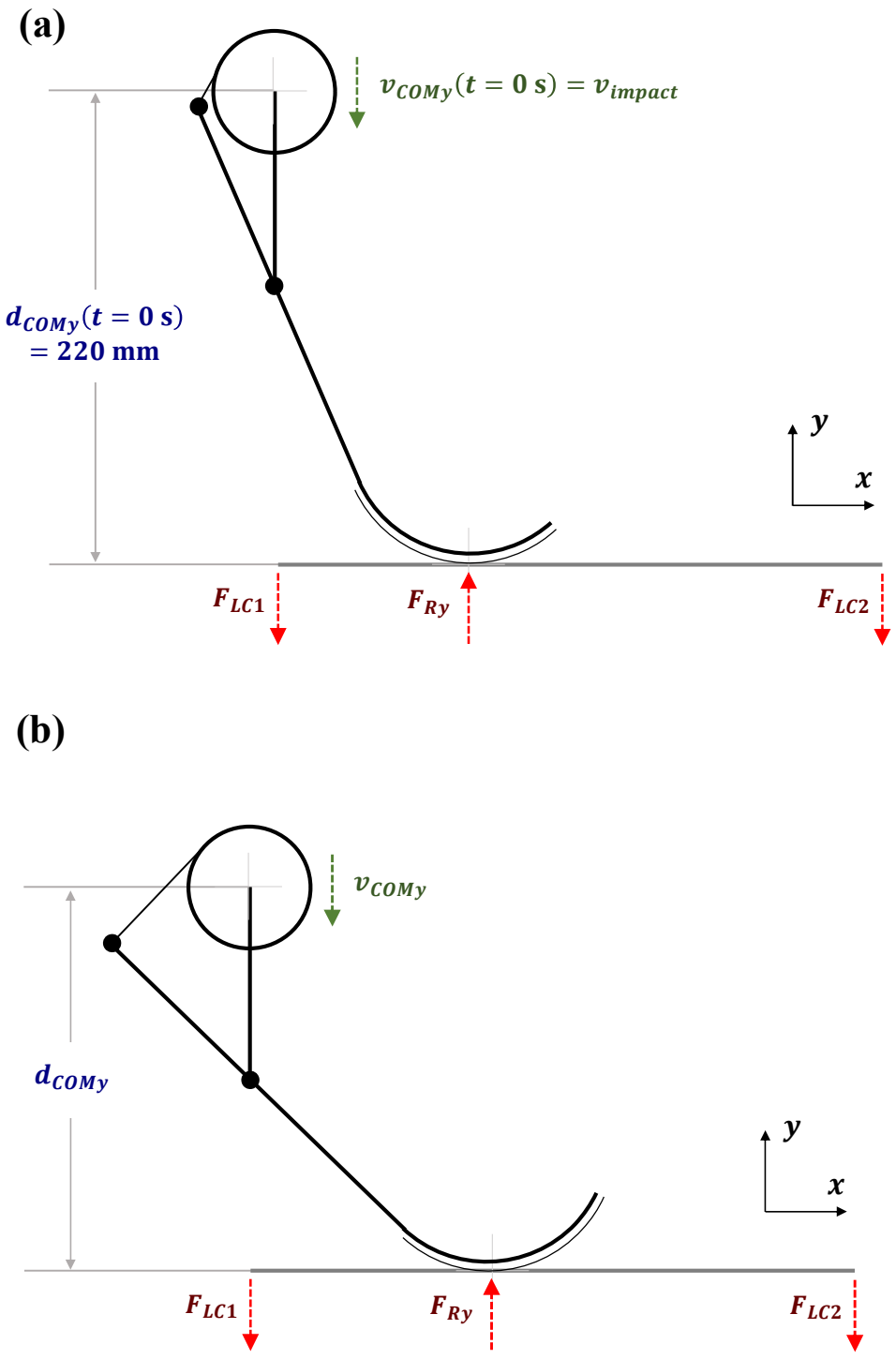

Figure 6-2 Impact loading free body diagram at (a) moment of impact, and (b) during impact.

6. 3 Experimental Procedure

To investigate the performance of the MRVSAL-II during impact loading, the leg was controlled to be dropped at a series of drop heights d_{drop} from 100 mm to a maximum of 600 mm in 100 mm increments. These drop heights correspond to a range of impact velocities v_{impact}, respectively, from 1.40 m/s to 3.43 m/s. Both the falling platform with and without the payload mass was tested, providing two scenarios for the total falling masses of 3.05 kg and 5.00 kg. For the passive performance of the leg, damper current was varied from 0 A to 3 A in 1 A increments, referred hereafter as the 'passive control modes'. In contrast to previous chapters, the maximum current here was increased from 2 A to 3 A, given marginal improvement was found during these experiments. Where impact-force control is applied, constant current is maintained during the impact. As well as the normal operating modes for the MRVSAL-II, two additional scenarios were arranged for these tests, one where the damper was effectively removed, the 'no damper' case, and one where the leg was made 'rigid' by fixing the upper and lower leg segments. Together, these represent two extremes, where the leg is very soft with low damping and very stiff with high damping, respectively. In either case, total falling mass was maintained to be identical to the other test scenarios. Each impact was conducted over a 5 s period, later cropped down to a 1 s period starting from the moment of impact when the load cells registered a non-zero value. This point in time corresponds to the initial COM height of the leg, i.e. $d_{COMy}(t = 0\text{ s}) = 220$ mm, and impact velocity $v_{COMy}(t = 0\text{ s}) = v_{impact}$, as illustrated in **Figure 6-2(a)**.

6. 4 Passive Control

6.4.1 Experimental Results

Included in **Figure 6-3(a)** to **(f)** are the COM vertical displacements d_{COMy} of the MRVSAL-II during the passive impact tests with the 3.05 kg total mass as drop height d_{drop} is increased from 100 mm to 600 mm. Also indicated in each plot is the COM displacement which corresponds to the leg bottoming out, which is approximately 97 mm. This practically reflects displacement at which the pivot point between the upper and lower leg segments collides with the ground. This is characterised by the deflection limit of the leg which is about 123 mm on a flat surface.

When the COM displacement reaches this threshold, collision occurs, influencing the dynamic behaviour of the leg during the impact.

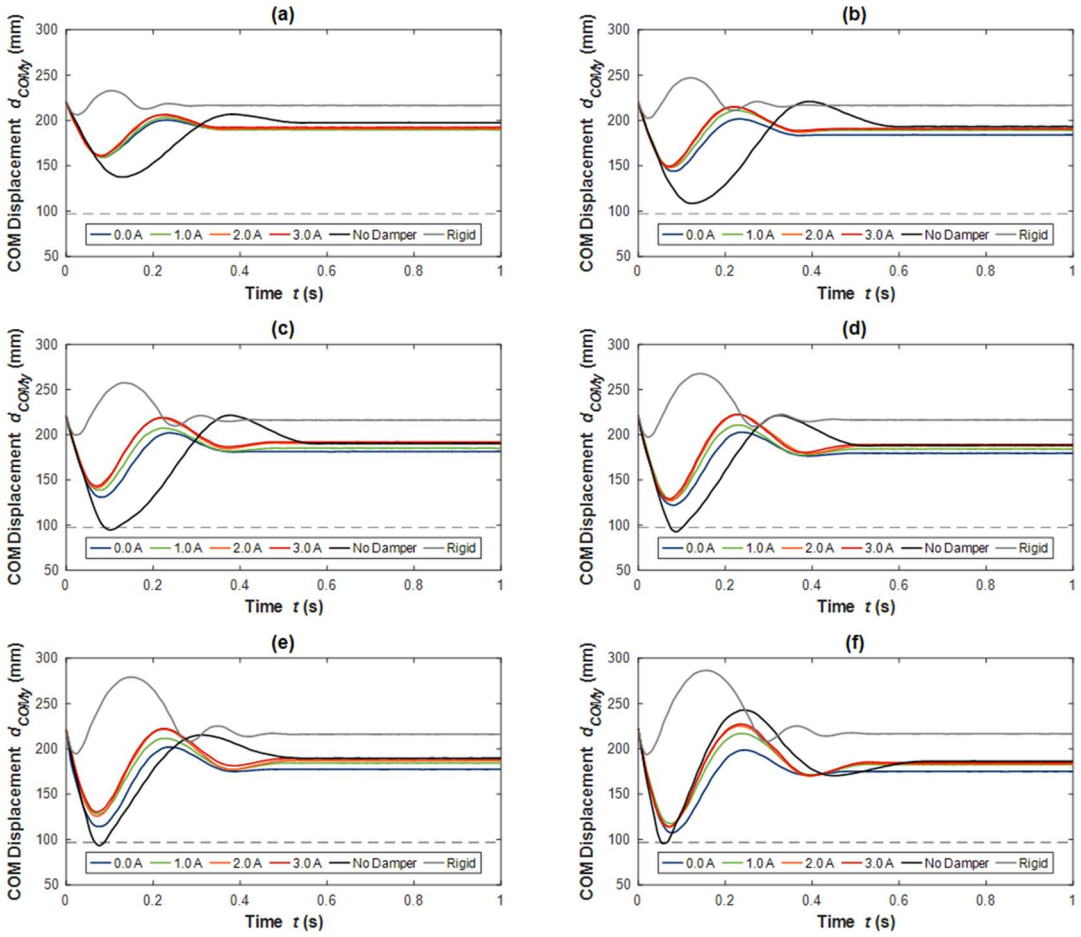

Figure 6-3 COM displacement for impact tests with a 3.05 kg total mass for drop heights of (a) 100 mm, (b) 200 mm, (c) 300 mm, (d) 400 mm, (e) 500 mm, and (f) 600 mm.

From **Figure 6-3(a)**, what is initially apparent is that for the no damper case, the deflection range for the leg is the largest, accompanied by the greatest settling time of 0.47 s. On the other hand, the rigid leg behaves quite differently, even entering ballistic flight as the leg bounces upon impact. Despite this, the rigid leg settles very quickly, within 0.15 s. In between these two extreme scenarios is where we find the passive damper control modes. On a scale comparable to the extreme scenarios, not much variation between currents is observable, however, it is noticeable that at 0 A the leg deflects more and has a lower rebound than that of the 3 A case, which rises 5.90% higher. As drop height is increased, these trends become more apparent, as observed in **Figure 6-3(b)**. For greater drop heights, i.e. **Figure 6-3(c)** to **(f)**, it appears

that the no damper case results in collision with the ground due to what appears to be a combined effect of low stiffness and low damping ratio. This is quite reasonable, given the removed rotary MR damper which governs the stiffness adjustment contributes quite high damping to the system. Despite the high impact energy for the 600 mm drop height, as seen in **Figure 6-3(f)**, no passive control mode results in collision, although, the 0 A case is not far from it.

When the total falling mass is increased to 5.00 kg, the COM displacement for all tests becomes more violent, indicated in **Figure 6-4**, given the impact energy has nearly doubled for these cases. It is seen in **Figure 6-4(a)** that even for a 100 mm drop height, the no damper case results in collision. There is also more substantial variation between the passive control modes, where it is seen that the 3 A case results in a rebound that is 40.1% greater than that of the 0 A case. At the 200 mm drop height of **Figure 6-4(b)**, the passive control modes approach the collision threshold, here with the 0 A case very narrowly avoiding collision. At this stage, it becomes challenging to distinguish the collision scenarios, however, so this will be discussed shortly with respect to the measured impact forces. Although, what does occur here is a transition during the 300 mm impact of **Figure 6-4(c)**, where some of the passive control modes experience collision, but others avoid it by a small margin. In all tests following this, i.e. from **Figure 6-4(d)** to **(f)**, all modes except for the rigid leg result in collision as the leg deflects to its maximum range.

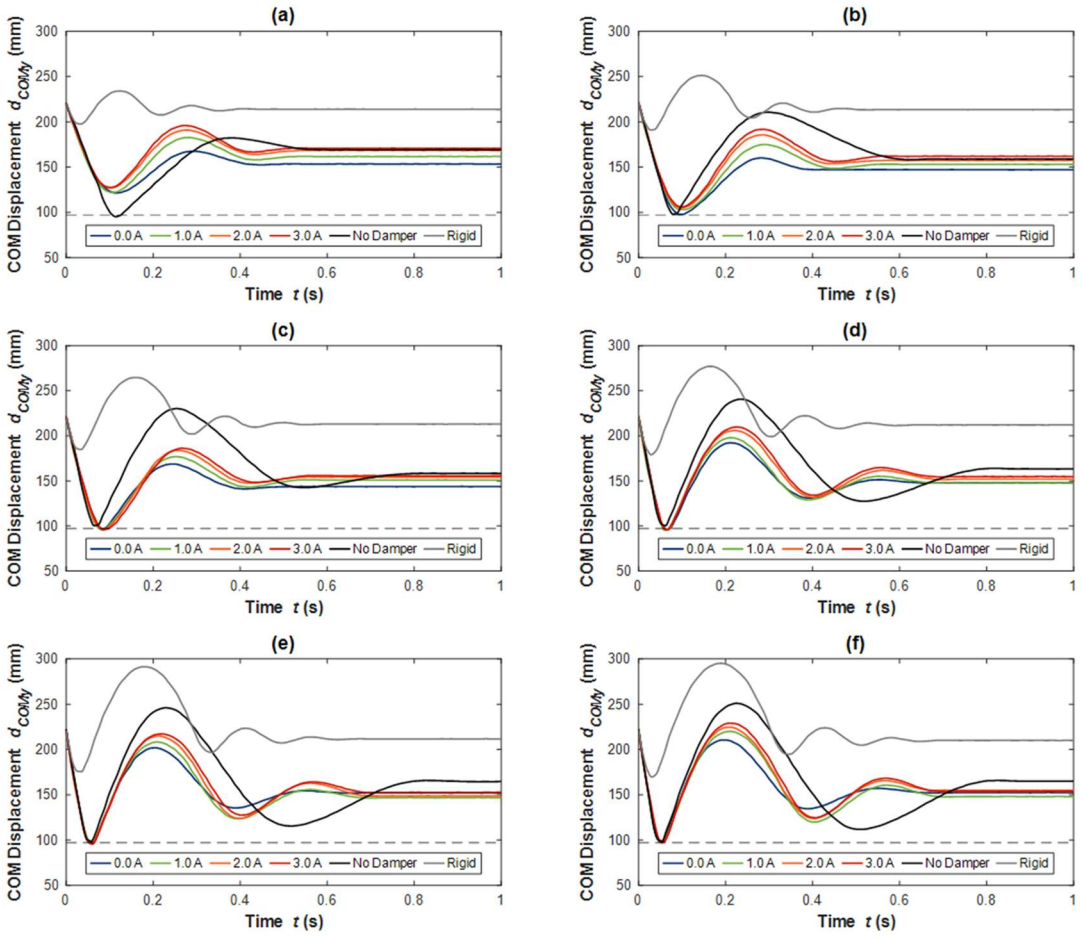

Figure 6-4 COM displacement for impact tests with a 5.00 kg total mass for drop heights of (a) 100 mm, (b) 200 mm, (c) 300 mm, (d) 400 mm, (e) 500 mm, and (f) 600 mm.

In terms of the rate at which the impact energy is dissipated, the settling time t_s for the COM displacement was investigated, as plotted in **Figure 6-5**. This is indicative of the rate of energy dissipation, with the vertical kinetic energy E_{Ky} being a function of the COM vertical velocity v_{COMy}. Starting with the fastest settling times, these were generally found for the rigid leg case, indicating this scenario resulted in the greatest effective damping coefficient during impacts for a given mass. This can be explained by a few contributing mechanisms which were specific to the tests with the rigid leg. First, for every single test, the leg COM later exceeded the impact initial height of 220 mm. This is consistent with the bouncing behaviour observed during tests. As a consequence, more work was done by the rubber foot pad attached to the leg in dissipating energy. This was further exaggerated by the high stiffness of the leg, leading to greater compression of the foot pad than in other tests. It is also likely that

there was greater flexure in the 3D-printed leg structure, causing greater internal energy dissipation.

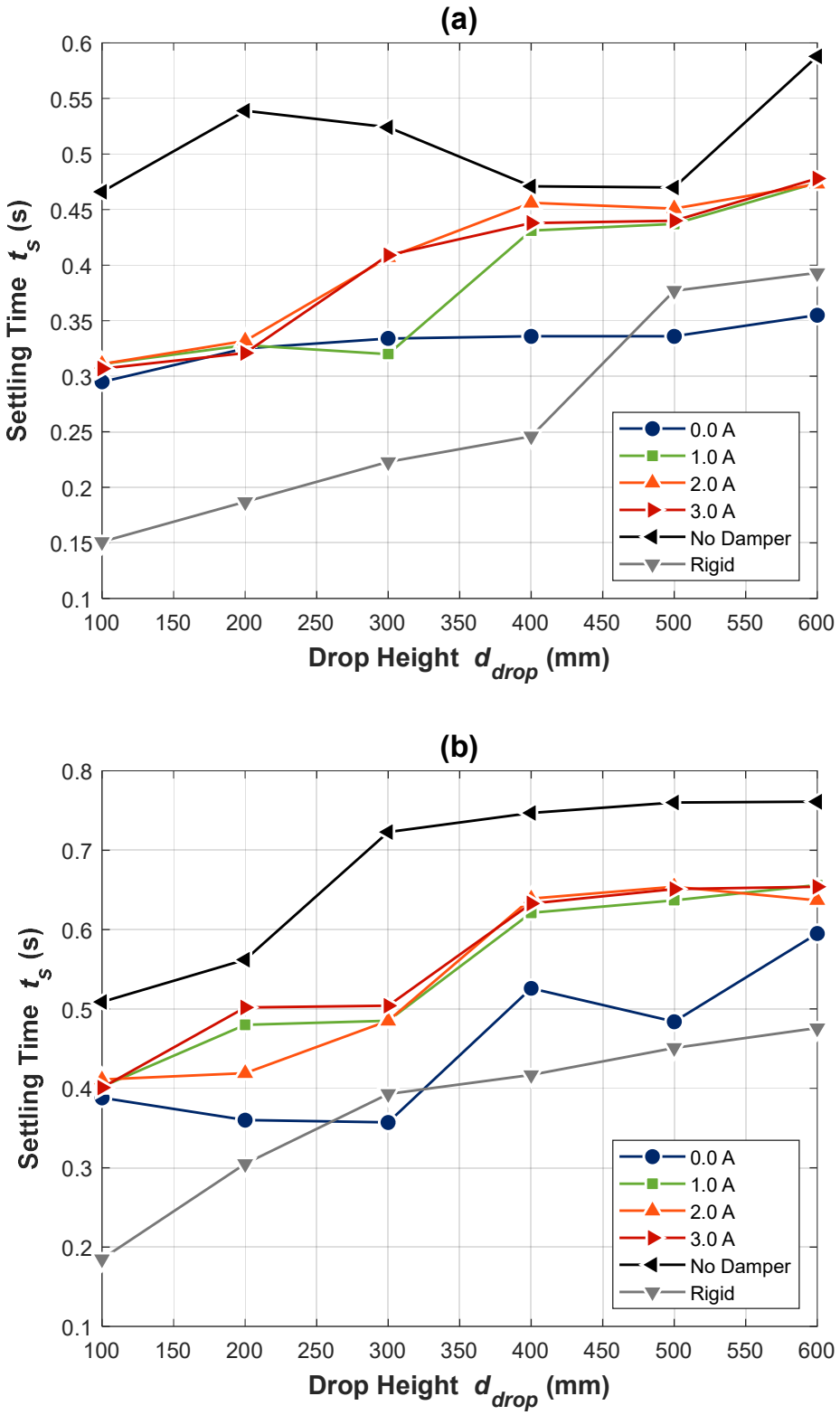

Figure 6-5 Settling time for impact tests with total masses of (a) 3.05 kg, and (b) 5.00 kg.

In great contrast, the no damper case led to the anticipated lowest effective damping coefficient, as indicated by the high settling times for these tests. For a legged robot, this would result in high vibration of the platform, which could lead to more collisions and erratic behaviour. As a reasonable middle ground, the settling times and hence energy dissipation rate of the passive controlled cases generally exist between the no damper and rigid cases. The tendency is for the 0 A cases to result in lower settling times, but as current increases towards 3 A, settling time increases. What this shows is that the effective damping coefficient for the leg during impacts is inversely related to damper current. Noting the difference in y-axis scales between **Figure 6-5(a)** and **(b)**, with greater mass comes greater settling time, which is anticipated as the decay constant $\zeta\omega_n$ for a typical dynamic system decreases with increased mass.

Of greater concern to us than the displacement of the leg is the impact force, given this can directly result in failure of robot parts or components, also gradually causing damage through fatigue. For the 3.05 kg total mass, the measured leg impact force F_{Ry} is reported in **Figure 6-6**. Starting with the 100 mm drop height, **Figure 6-6(a)** reflects the displacement behaviour observed in **Figure 6-3(a)**. In particular, the ballistic flight of the rigid leg as it bounces can be observed here too where the force reduces to zero. As expected, this rigid leg and the bouncing behaviour also results in the greatest impact force, reaching 123 N in this case. Secondary to this are the passive control modes, reducing in force from 3 A to 0 A, followed by the no damper case with a peak impact force of 59.9 N. The other notable behaviour, present in all tests other than those of the rigid leg, is the initial peak in the force prior to the subsequent and usually largest peak. Based on observations made during testing, it seems the angle of the draw cable between the lower leg segment and variable stiffness mechanism is close to 0° from the y-axis. This makes the leg relatively stiffer for the few millimetres of deflection, explaining the short rise in force which subsides until the maximum deflection of the leg is reached. This was not encountered in the initial testing of the MRVSAL-II within **Chapter 4** as the leg was pre-compressed for force characterisation experiments.

Although impact force increases between **Figure 6-6(a)** and **(c)**, it isn't until **Figure 6-6(d)** where the first collision with the ground occurs for the no damper case. While the displacement of the leg in **Figure 6-3(c)** indicate collision has occurred, it is a marginal case here, given no substantial secondary peak in impact force is

observed. From **Figure 6-6(d)** to **(f)**, however, this peak becomes very obvious, even surpassing the peak force of the rigid case for the 600 mm drop height where a value of 242 N is reached. While the peak force of the rigid cases is always exceptionally high, for these greater drop heights with this mass, it is evident the no damper case also provides unsatisfactory performance. When the leg makes use of the designed passive control modes, a more reasonable range of peak force between about 75 N to 140 N is maintained. Here it is found that the 0 A case consistently provides the optimal performance over other passive currents, always resulting in the minimum peak force for the MRVSAL-II. For the 600 mm drop height, this represents a reduction in peak force of 20.1% from the 3 A force of 135 N to 0 A force of 108 N.

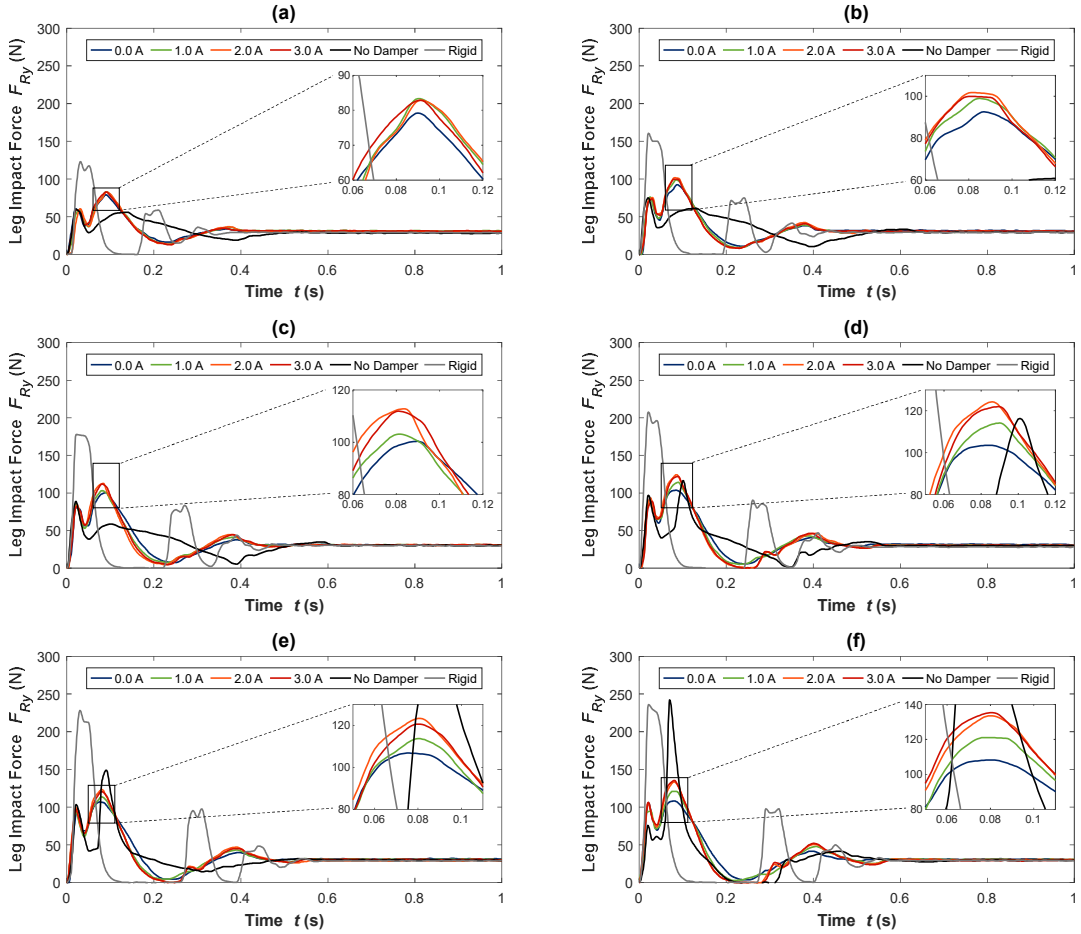

Figure 6-6 Leg impact force for impact tests with a 3.05 kg total mass for drop heights of (a) 100 mm, (b) 200 mm, (c) 300 mm, (d) 400 mm, (e) 500 mm, and (f) 600 mm.

In contrast to the impacts with the lower mass, the tests conducted with the 5.00 kg total mass, included in **Figure 6-7**, indicate collision occurs for the no damper case in all tests. Where no such collision occurs, compared to the 3.05 kg total mass tests, peak impact force for all tests is increased here by a factor of roughly 1.5, somewhat lower than the 1.74 factor by which the mass was increased. Of more relevance to managing these impacts, however, it is observed that no collision occurs for any passive control mode for the 100 mm and 200 mm drop heights, included in **Figure 6-7(a)** and **(b)**, respectively. Where it was challenging to distinguish from displacement data alone in **Figure 6-4(c)**, here in **Figure 6-7(c)**, the corresponding 300 mm tests show that the passive control modes start to also result in collisions. Where impacts with lower mass or drop heights previously indicated the 0 A passive control mode was always optimal, it is evident here that it is the worst-performing current setting. In contrast to the recorded 241 N peak force of the 0 A case, a reduction of 37.3% to 151 N is obtained through the 3 A case. While some variation between other passive control modes is found for greater drop heights, it can be seen from **Figure 6-7(d)** to **(f)** that the minimum peak impact force is consistently obtained for the MRVSAL-II by the 3 A current setting. It can also be observed that when significant collisions do occur, i.e. those seen here beyond 300 mm drop heights, the no damper case actually results in a lower impact force. Although, coupled with a lower effective damping coefficient, as indicated by the longer settling times of **Figure 6-5(b)**, impact energy is dissipated over a longer period for the no damper case.

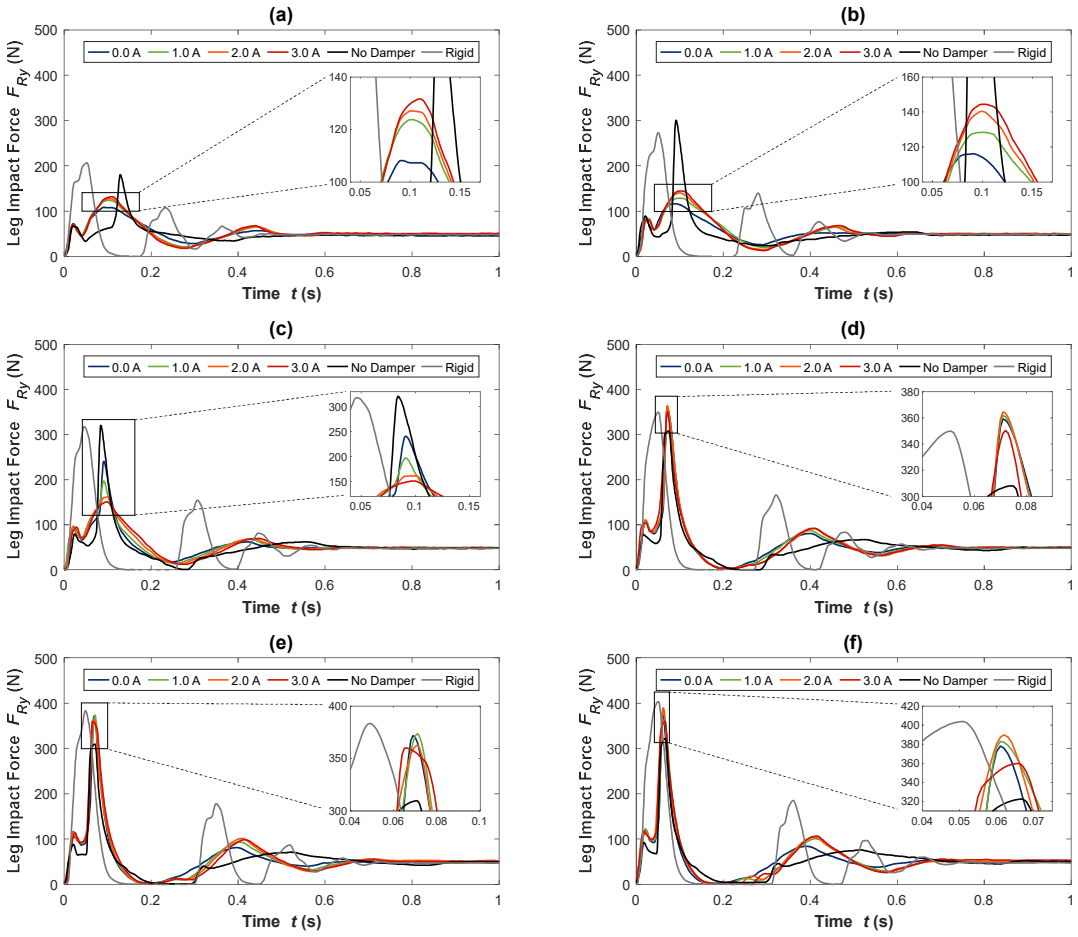

Figure 6-7 Leg impact force for impact tests with a 5.00 kg total mass for drop heights of (a) 100 mm, (b) 200 mm, (c) 300 mm, (d) 400 mm, (e) 500 mm, and (f) 600 mm.

To provide a good indication of impact protection performance for the passive control modes, **Figure 6-8** includes the peak impact force $F_{Ry,max}$ for all tests. Considering the low mass tests, **Figure 6-8(a)** shows that with the exception of the 100 mm to 400 mm drop height range, the passive control modes, particularly 0 A, result in lower peak impact forces than the very soft no damper mode and very stiff rigid mode. Summarised in **Figure 6-8(b)**, being mindful of the y-axis scale, the impact forces recorded here readily surpass that of the lower mass tests. It is also clear that a transition occurs for the passive control modes around 200 mm to 400 mm drop heights, corresponding to where ground-collisions start to occur in these tests.

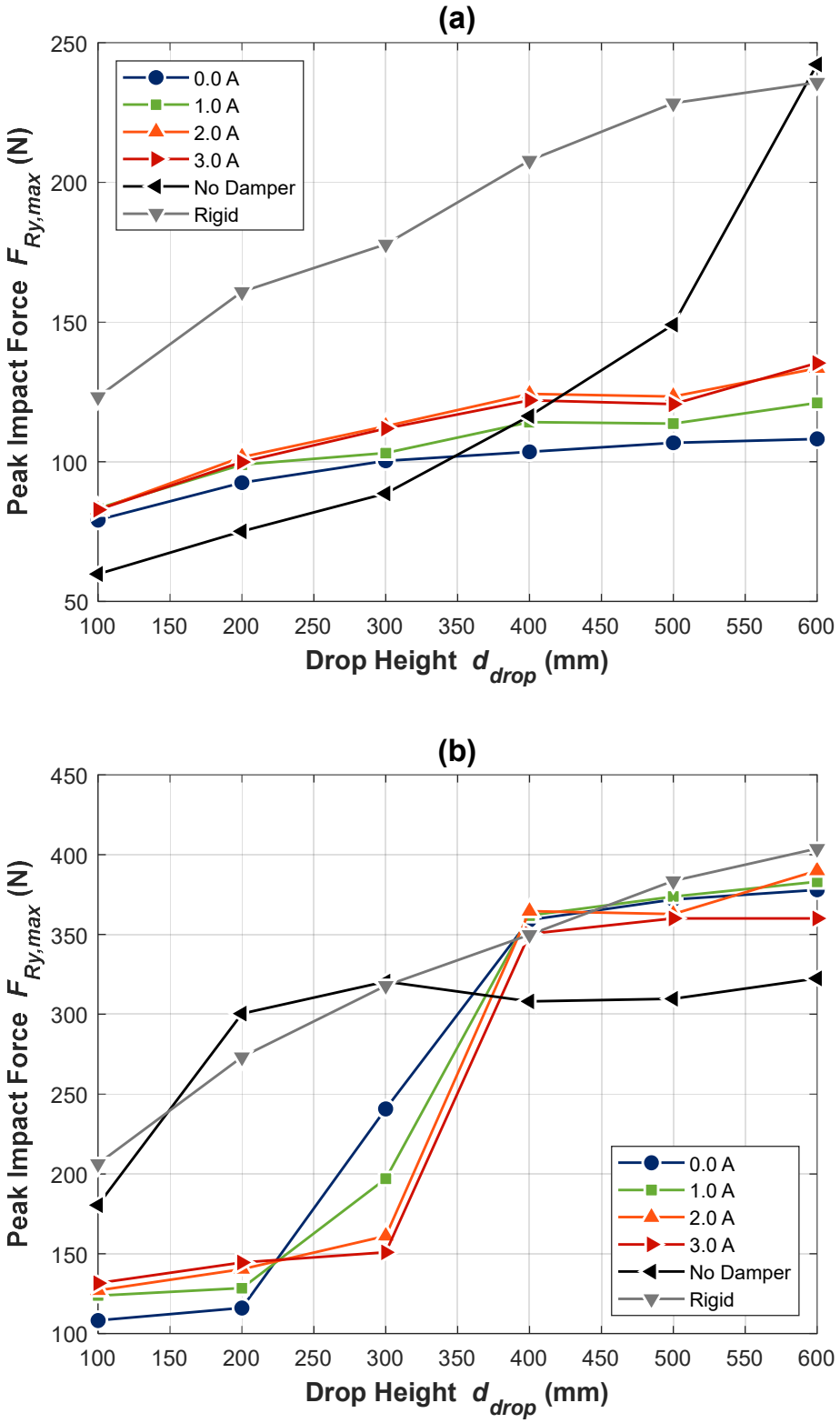

Figure 6-8 Peak impact force for impact tests with masses of (a) 3.05 kg, and (b) 5.00 kg.

6. 5 Impact-Force Control

6.5.1 Controller Development

With high impact loads potentially putting legged robots and adjacent hardware at risk, a reasonable goal for the control of the MRVSAL-II during impact loading is to minimise peak impact force. Based on observations during the passive control tests, it was found that for many cases, 0 A or other low currents outperformed the 3 A current, indicating lower stiffness and higher damping were beneficial. This is quite reasonable, given a softer leg would require more travel and a greater period to reach its maximum deflection. Coupled with a larger, yet moderate level of damping, this would allow for dissipation of impact energy at a high rate without causing excessive loading. In stark contrast, when leg deflection exceeded the range the leg was designed to be capable of, collision of the upper leg segment with the ground caused substantially higher forces for the leg when softer. Thus, there is a trade-off: a lower stiffness leg will reduce impact force, but only for a certain level of deflection; a higher stiffness is required to protect the leg from deflecting beyond its functional range, but otherwise will result in greater impact forces. The key parameter which dictates how far the leg will travel, assuming a constant level of damping with leg deflection, is the vertical kinetic energy E_{Ky} of the leg during impact. Making the reasonable assumption that energy is conserved while the leg and platform falls, the gravitational potential energy E_P of the leg becomes the kinetic energy, i.e.:

$$E_{Ky}(t = 0\ \mathrm{s}) = E_P(t = 0\ \mathrm{s}) = m_{total} \cdot g \cdot d_{drop} \quad [\mathrm{J}], \tag{6-1}$$

with a corresponding impact velocity v_{impact} of:

$$v_{impact} = v_{COMy}(t = 0\ \mathrm{s}) = \sqrt{2 \cdot g \cdot d_{drop}} \quad [\mathrm{m/s}]. \tag{6-2}$$

Based on the passive control tests, **Equation (6-1)** was applied to convert the drop heights and platform masses into their corresponding kinetic energies at the moment of impact. Following the peak impact forces, the corresponding current which obtained the minimum force was then plotted in **Figure 6-9(a)**. With the assumptions made, one data point conflicts as the leg did not collide during the low mass 600 mm drop for 0 A current. With this one exception, a clear transition was observed at about 15 J of vertical kinetic energy, below which the leg current should be 0 A and above

which the leg current should 3 A. Given the near immediate transition within the recorded data, there are essentially binary states the leg should operate in to minimise impact force. This is illustrated in the figure by the solid line through the data, representing the damper current control signal that should correspond to measured kinetic energy at the moment of impact. Based on this concept, **Figure 6-9(b)** shows the process flow diagram for the adopted control algorithm, assuming sensory data has indicated an impact is imminent.

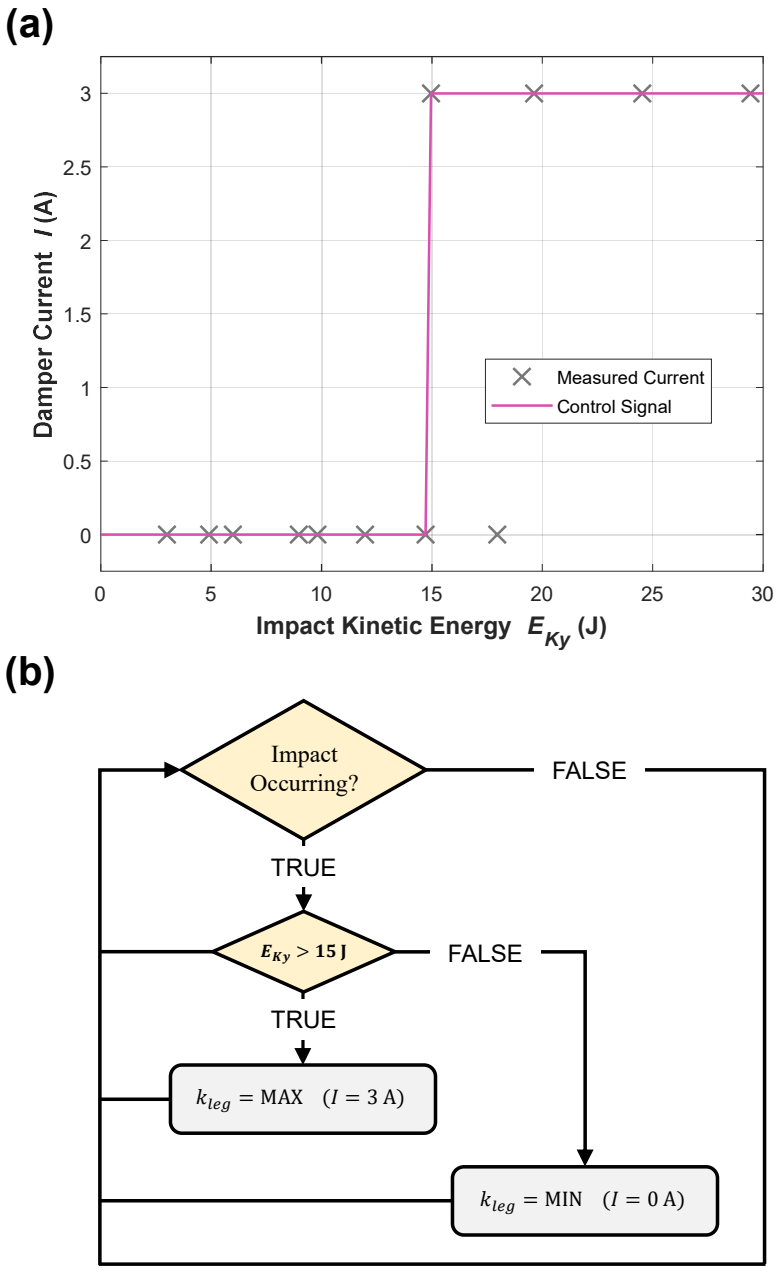

Figure 6-9 Impact force controller (a) damper control signal, and (b) process flow diagram.

6.5.2 Experimental Results

Based on the adopted control algorithm, additional impact tests were conducted for both 3.05 kg and 5.00 kg total falling masses. The impact forces recorded during these tests at all drop heights from 100 mm to 600 mm are presented in **Figure 6-10**, along with those from the no damper and rigid cases. This visually captures the behaviour quite well, showing that for a lower fall mass, as in **Figure 6-10(a)**, the controlled MRVSAL-II is able to operate within a tight range of impact forces from 79.2 N to 135 N. In contrast, the rigid leg always results in excessive impact forces, ranging from 123 N to 236 N. While the no damper case initially leads to smaller impact forces, there is substantial variation due to frequent ground collisions, with a range of 59.9 N to 242 N. For the larger mass scenario, included in **Figure 6-10(b)**, the rigid leg scenario has a range of 206 N to 404 N, with the no damper case varying between 180 N and 322 N. Initially resulting in the lowest impact force for these tests, the controlled mode has a range of 108 N to 360 N. While this does eventually exceed the no damper case, as anticipated from passive tests, the overall improvement in performance here is still evident. This is better understood through the percentage reduction in impact force when comparing the controlled mode to both the no damper and rigid modes, as in **Figure 6-11**. Despite some cases where the absence of the damper shows lower impact force, for the 3.05 kg mass in **Figure 6-11(a)**, we find general improvement through control of the MRVSAL-II. When compared, this results in up to 53.2% improvement over the rigid leg, and up to 44.1% improvement over the leg with no damper. For the 5.00 kg mass in **Figure 6-11(b)**, in most cases, the controller offers improvement, with up to 61.4% reduction in peak impact force over the no damper case, and up to 57.5% reduction over the rigid case.

Although not the direct intent of the controller, it is also of interest to compare the displacement of the leg against the rigid and no damper cases, with the corresponding displacement of **Figure 6-10** included in **Figure 6-12**. Here we can see that similar to the impact force, the COM displacement of the controlled mode falls within a reasonably tight band when compared to the other modes. The controlled mode also most seldomly experiences bouncing following a collision. Comparing the settling time between the modes, as included in **Figure 6-13**, somewhat of a compromise is found, given the rigid leg experiences shorter settling times and higher impact forces, where the no damper leg experiences high settling times and sometimes

lower impact forces. For the 3.05 kg mass, included in **Figure 6-13(a)**, the controller results in a maximum improvement in settling time over the no damper leg of 50.6%, and 9.16% over the rigid leg. For the 5.00 kg mass, shown in **Figure 6-13(b)**, we find improvement by up to 35.9% over the no damper case and at best a 18.0% increase in settling time when compared to the rigid leg, as indicated by the negative percentage here.

6. 6 Chapter Summary

As it is an important requirement for legged robots, like biological legged locomotors, to protect themselves against high impact forces, the MRVSAL-II was put through a series of impact loading experiments within this chapter. Drop testing experiments were conducted with the leg for drop heights ranging from 100 mm to 600 mm, with different payload masses. It was established that while lower stiffness and higher damping could lead to lower impact forces and greater rates of energy dissipation, respectively, optimal control would also protect the leg from deflecting beyond its functional range. Compared with an identical rigid leg with higher damping, up 57.5% reduction in impact force was achieved and 61.4% reduction was achieved over a softer leg with lower damping.

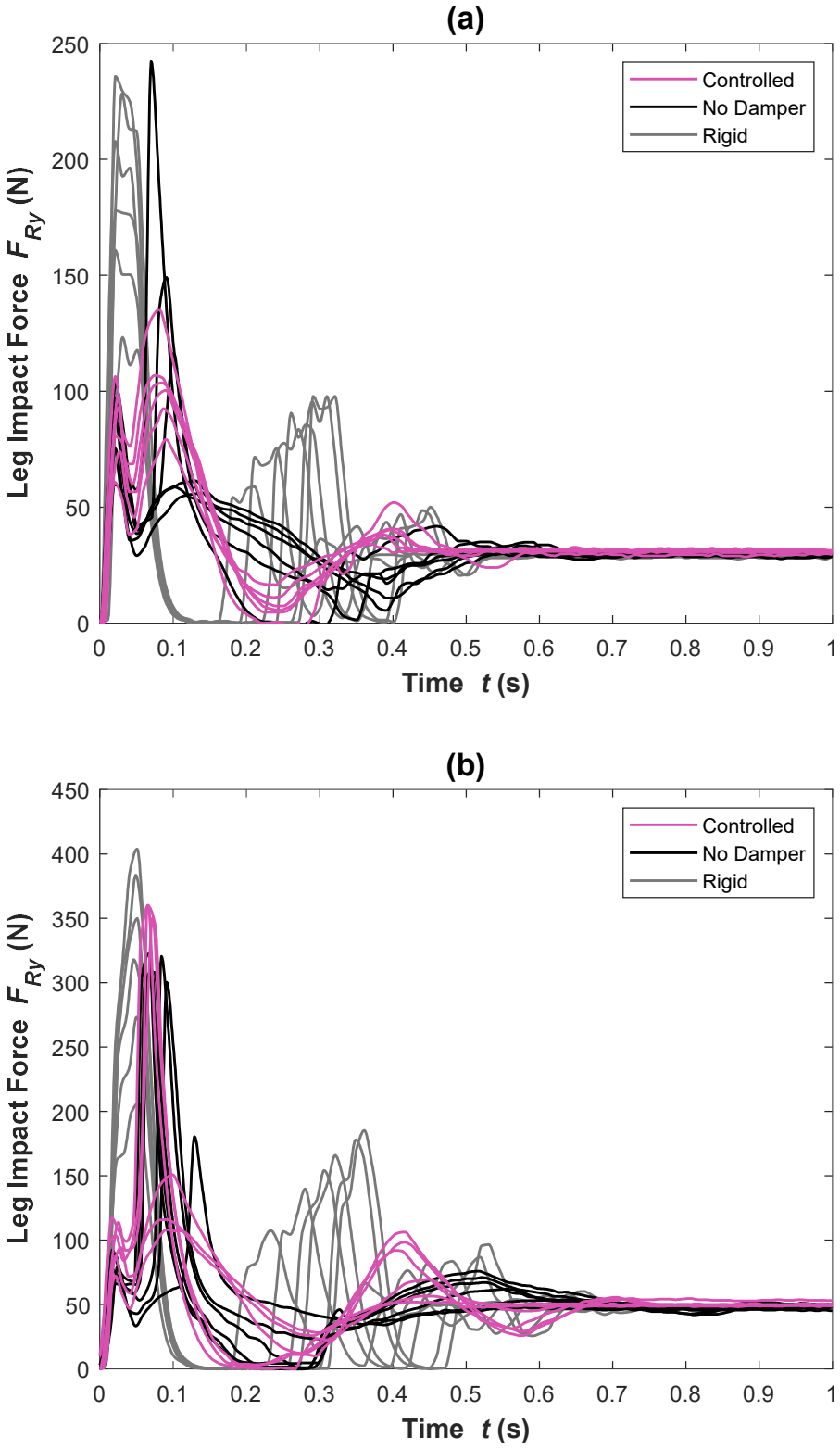

Figure 6-10 Controlled impact force for impact tests at all drop heights with total masses of (a) 3.05 kg, and (b) 5.00 kg.

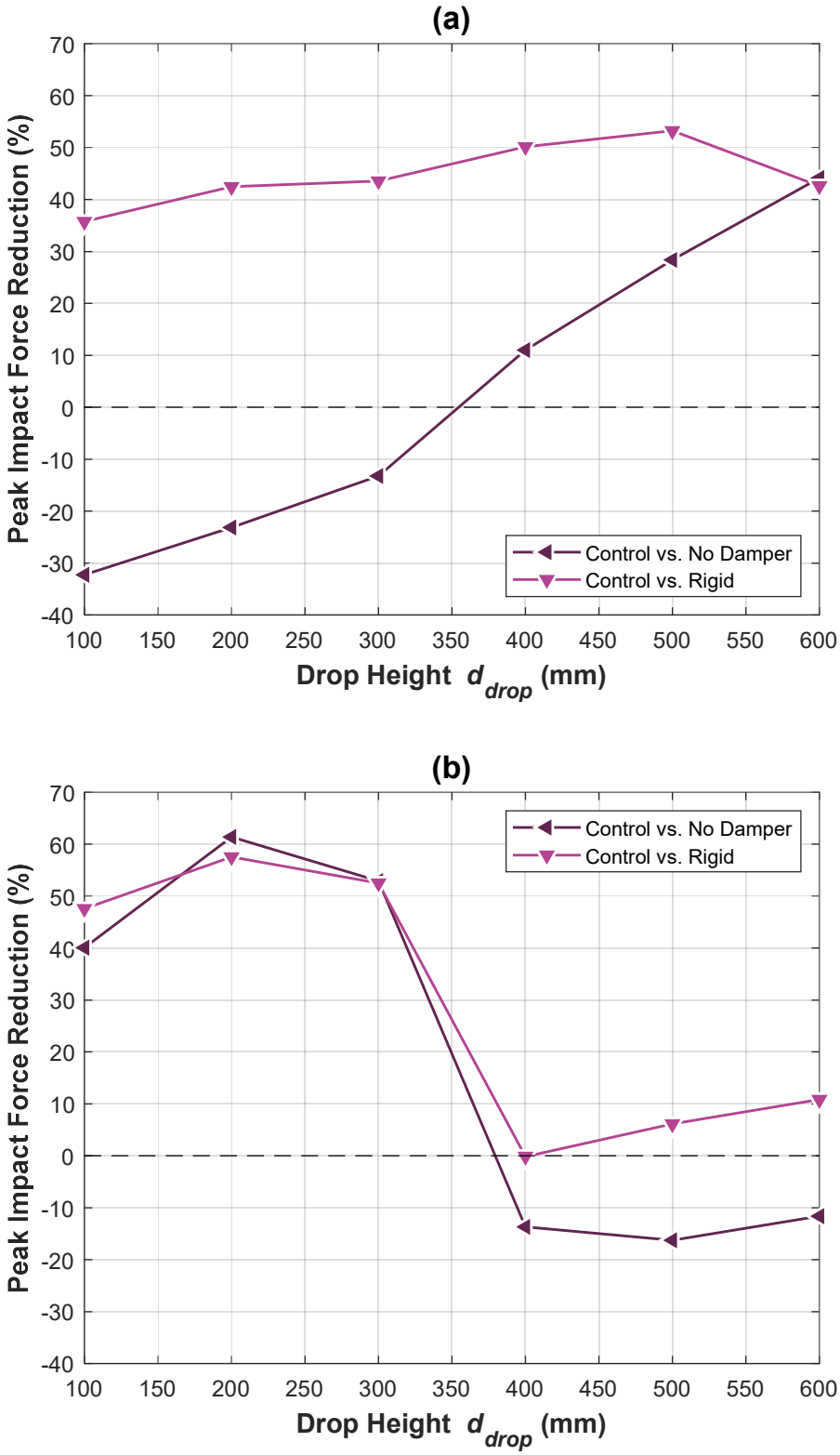

Figure 6-11 Controller improvement in peak impact force for impact tests with total masses of (a) 3.05 kg, and (b) 5.00 kg.

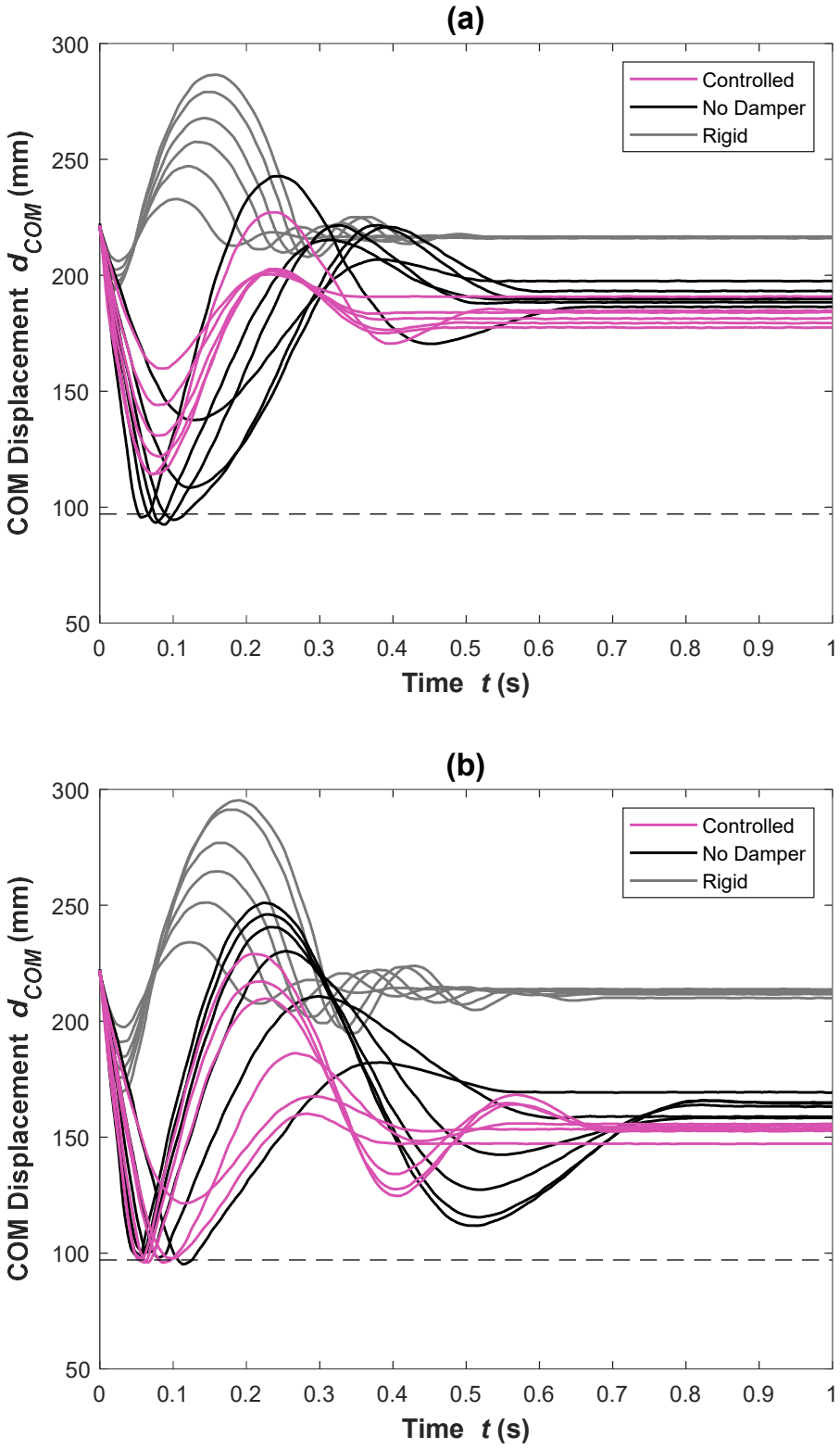

Figure 6-12 Controlled COM displacement for impact tests at all drop heights with total masses of (a) 3.05 kg, and (b) 5.00 kg.

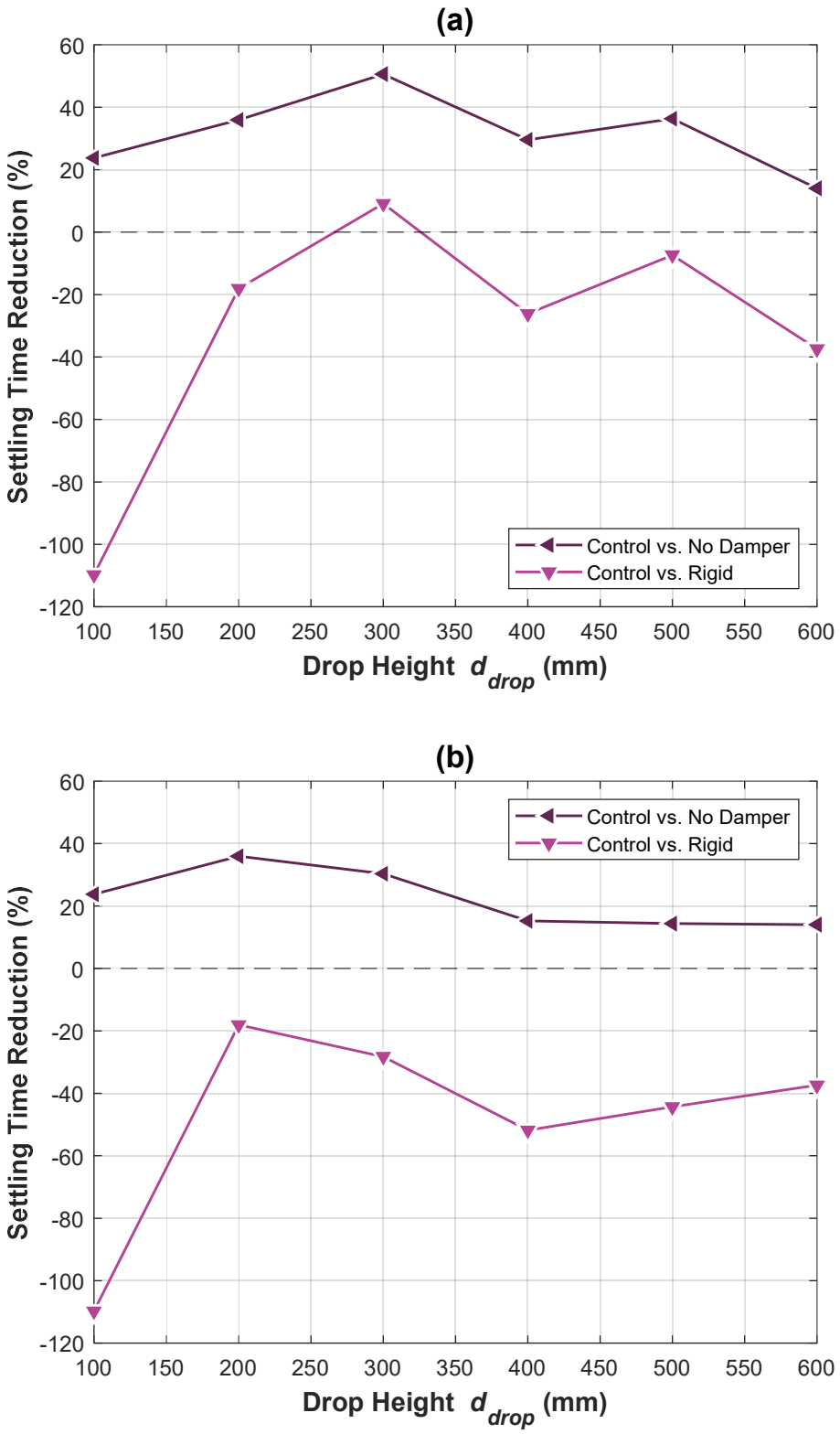

Figure 6-13 Controller improvement in settling time for impact tests with total masses of (a) 3.05 kg, and (b) 5.00 kg.

7 CONCLUSIONS AND FUTURE WORK

7. 1 Achieving Variable Stiffness with a Rotary MR Damper

7.1.1 Variable Stiffness Behaviour in Robot Legs

To facilitate MRF-based variable stiffness within robot legs, existing linear damper solutions were not practical due to geometric and dynamic impracticalities. To overcome these challenges, a rotary MR damper was developed to produce a rotary variable stiffness mechanism. Early tests conducted within this thesis showed that a leg fitted with such a mechanism could see stiffness variation between the two extremes of the included parallel spring stiffnesses, i.e. soft spring only or the sum of the soft and stiff spring stiffnesses. With a measured stiffness increase of up to 257%, this approach to achieving variable stiffness within robot legs was shown to be highly effective. Furthermore, in contrast to existing use of MRE to enable variable stiffness in a robot leg, MRF has been shown to be significantly more robust, given yielding of the material does not result in direct failure of the leg.

Contrary to the intent of achieving variable stiffness to, in part, reduce locomotion cost, it was also found through the experiments conducted in this thesis that the variable stiffness achieved by the rotary MR damper mechanism was always accompanied by a level of hysteretic damping. This is a fundamental limitation of employing MR dampers to achieve variable stiffness. The historic use of mechanical springs or other such compliance in robot legs has been to aid the store and return of

energy during locomotion. With a percentage of this energy being dissipated due to the variable stiffness mechanism itself, locomotion performance is also most certainly influenced. Although, the extent to which the variable stiffness or the energy dissipation contribute to the behaviour is not quantified in this research. This can be beneficial in managing disturbances, however, as well as reducing shocks and excessive vibration during impact loading.

7.1.2 Robot Leg Design

Presented in this thesis were two MRF-based variable stiffness leg designs, featuring different leg morphologies. While the first design was capable of achieving a higher stiffness range due to the selection of spring stiffnesses, the variable stiffness mechanism was offset from the point of torque actuation. Consequently, greater inertia was felt by the motor, causing increased energy consumption. Combined with the inherent rotary imbalance of the design, this induced vibration within the bipedal locomotion platform when fitted with these legs. These issues were resolved in the improved design, shifting the COM of the leg to the point of torque actuation, which is of practical importance to robot leg designs featuring MR technology. In regard to powering the included rotary MR dampers, it also became evident during the design stages that sliding electrical contacts are needed to enable continuous leg rotation while powering the dampers.

7. 2 Locomotion of Legged Robots with MRF-Based Variable Stiffness

7.2.1 Resonant Running and Cost of Transport

For many decades, the question of what role compliance plays in the legs of biological locomotion has been studied. Very recently, the findings of this fundamental question have led researchers to attempt to recreate such behaviour in legged robots. One of the key assertions of biological studies is that locomotors will adjust effective leg stiffness when locomoting at different stride frequencies in order to reduce the energy cost of locomotion, i.e. COT. To investigate this question and simultaneously evaluate the performance of MRF-based variable stiffness, legged locomotion studies were conducted in this thesis. Between the two leg designs presented, varying results were found. For the earlier design, it was shown to be quite clear that optimal leg stiffness tuning could in fact provide reduced MCOT, neglecting the damper power consumption which would factor into the wholistic COT. For the revised leg design,

while similar behaviour was not observed, MCOT was reduced across the entire stiffness range of the leg when compared with the former.

7.2.2 Manoeuvring Disturbances Using Variable Stiffness

Another way in which biological locomotors provide superior performance when compared with legged robots with passively compliant legs is in mitigation of terrain-based disturbances. That is, numerous studies have given indication that modulation of leg stiffness also plays a vital role in dealing with changes in terrain elevation, whether there is an increase, i.e. obstacle, or decrease, i.e. valley. Through investigation of such disturbances and also coronal gradients, it was shown in this thesis that legged robots can too achieve similar benefits through adaptive control of leg stiffness. While some benefit to MCOT was achieved for a few scenarios, the primary improvement to locomotion performance was found in the improve roll angle stability of the robot platform, allowing the desired gait to be maintained. For unconstrained locomotion, it is expected that this could further improve MCOT as reduced control effort would be required to adjust locomotion gait and trajectory. Such experimentation was not conducted within the scope of this thesis, however.

7.2.3 Impact Protection Through Leg Stiffness Control

Evident from a substantial amount of research on humans during drop landings, there are various mechanisms employed to brace for impacts in an effort of self-preservation. Through such adjustments within the musculoskeletal system, decreasing effective leg stiffness has been reported to reduce impact forces. Similarly, this behaviour should translate to legged robots, which rather than tearing muscles and breaking bones can experience hardware failure directly or through fatigue. Through experimentation of drop landings of a robot leg with MRF-based variable stiffness, it was established that improvement over passive stiffness could readily be achieved. In comparison to high passive stiffness, the increased deflection of the leg evidently reduced impact loads. When compared with low passive stiffness, impact loads were mitigated through limiting the deflection of the leg, given excessive deflection would lead to ground collisions and high impact forces. The hysteretic damping of the MRF-based variable stiffness leg also appeared to improve performance, given the faster rate of energy dissipation causing greater decay of body vibrations.

7. 3 Recommendations for Future Work

7.3.1 Reduction in Energy Cost of MRF-Based Variable Stiffness

Something that was omitted from the scope of this thesis is the analysis of power consumption resulting from the electromagnet used to stimulate the MRF included in the rotary MR dampers of the legs. This is why MCOT was adopted as a performance metric here rather than COT, omitting electrical power requirements other than that for the actuating leg motors. In literature, the assumption of convenient access to power for MR dampers is ubiquitous. Despite this, numerous existing or emerging applications for MR technology, such as legged robots, are in need of careful consideration of damper energy cost to become more practical than passive or other low-power solutions. While energy loss through hysteretic damping appears to be unavoidable for MRF-based variable stiffness, reduction in energy cost could be achieved through employing permanent magnets in a hybrid electromagnet design, or perhaps through active or deflection-dependent position adjustment of permanent magnets. Such alternatives should be investigated to progress research within this field for MRF-based variable stiffness.

7.3.2 Investigation of Variable Stiffness Combined with Variable Damping in Robot Legs

Based on the level of hysteretic damping observed for the MRF-based variable stiffness robot legs, this also raises the question of how legged locomotion could benefit from variable stiffness in combination with independently variable damping. Where combined variable stiffness and variable damping devices utilising MRF have been presented in literature for other applications, no experimental studies have focused on employing this for legged robots. This would also provide useful information to help distinguish the relative contribution of variable stiffness and variable damping to locomotion, which were concurrent within this thesis.

7.3.3 Use of Alternative Smart Materials to Achieve Variable Stiffness in Robot Legs

Alternative to MRF, shear thickening fluid (STF) can provide identical rheological behaviour to the magnetorheological effect, albeit in response to increased shear rate rather than magnetic flux. While not applicable to all locomotion scenarios,

resonant running may be achievable. This is given optimality is found when high stiffness is paired with high stride frequency and low stiffness with low stride frequency. This proportional relationship could be established in a smart-passive way, given STF will increase in viscosity with an increase in shear rate. This increase in shear rate should be a passive consequence of increased stride frequency. This is identical to the desirable increase in MRF viscosity to increase leg stiffness within the presented variable stiffness mechanism in this thesis. Hence, through careful design, a rotary STF damper could be employed to produce a smart-passive STF-based variable stiffness mechanism and robot leg with no energy cost associated with control. Furthermore, material requirements of the damper are less stringent, with no metal parts fundamentally required, which could significantly reduce leg weight as well. The use of STF in this way is worth investigation, with very few published works exploiting this concept to date.

7.3.4 Experimental Investigation of Unconstrained Locomotion with MRF-Based Variable Stiffness Robot Legs

While it did not make it within the scope of this thesis, the next logical step for this research is to employ MRF-based variable stiffness robot legs in a full-scale unconstrained legged robot platform. In contrast to the constrained locomotion studies and focus on specific scenarios for the robot legs, a locomotion platform suited to these would reveal much more information about the dynamic behaviour and overall performance that can be attributed to the legs. This could further serve to couple advanced sensory feedback with leg stiffness control for experimentation in urban areas and rugged undeveloped terrain. In addition, another question is still left open in literature today, that being how leg stiffness control should couple with gait control. Within this thesis, locomotion studies did not include investigation into different gaits, given the limitations of the constrained locomotion test rigs that were built.

PUBLICATIONS INCLUDED IN THIS WORK

Journal Articles

[1] **M. D. Christie**, S. Sun, D. H. Ning, H. Du, S. W. Zhang, and W. H. Li, "A highly stiffness-adjustable robot leg for enhancing locomotive performance," *Mechanical Systems and Signal Processing,* vol. 126, pp. 458-468, 2019.

[2] **M. D. Christie**, S. Sun, L. Deng, H. Du, S. W. Zhang, and W. H. Li, "Real-Time Adaptive Leg-Stiffness for Roll Compensation via Magnetorheological Control in a Legged Robot", *IEEE/ASME Transactions on Mechatronics* [Under Review]

[3] **M. D. Christie**, S. Sun, L. Deng, H. Du, S. W. Zhang, and W. H. Li, "Shock Absorption for Legged Locomotion Through Magnetorheological Leg-Stiffness Control", *Mechanical Systems and Signal Processing* [Under Review]

ADDITIONAL PUBLICATIONS DURING CANDIDATURE

Journal Articles

[4] **M. D. Christie**, S. Sun, J. Quenzer-Hohmuth, L. Deng, H. Du, and W. H. Li, "A magnetorheological fluid based planetary gear transmission for mechanical power-flow control," *Smart Materials and Structures,* vol. 30, no. 4, p. 045013, 2021.

[5] J. Yang, **M. D. Christie**, S. Sun, D. Ning, M. Nakano, Z. Li, H. Du, and W. H. Li, "Integration of an omnidirectional self-powering component to an MRE isolator towards a smart passive isolation system," *Mechanical Systems and Signal Processing,* Article vol. 144, 2020, Art. no. 106853.

[6] Y. Guo, B. Li, **M. D. Christie**, Z. Li, M. A. Sotelo, Y. Ma, D. Liu, and Z. Li, "Hybrid dynamic traffic model for freeway flow analysis using a switched reduced-order unknown-input state observer," *Sensors (Switzerland),* Article vol. 20, no. 6, 2020, Art. no. 1609.

[7] **M. D. Christie**, S. Sun, L. Deng, D. Ning, H. Du, S. Zhang, and W. Li, "The variable resonance magnetorheological pendulum tuned mass damper: Mathematical modelling and seismic experimental studies," *Journal of Intelligent Material Systems and Structures,* Article vol. 31, no. 2, pp. 263-276, 2020.

[8] T. Jin, Z. Liu, S. Sun, Z. Ren, L. Deng, B. Yang, **M. D. Christie**, and W. Li, "Development and evaluation of a versatile semi-active suspension system for high-speed railway vehicles," *Mechanical Systems and Signal Processing,* Article vol. 135, 2020, Art. no. 106338.

[9] D. Ning & **M. D. Christie**, S. Sun, H. Du, W. Li, and Y. Wang, "A controllable mechanical motion rectifier-based semi-active magnetorheological inerter for vibration control," *Smart Materials and Structures,* vol. 29, no. 11, p. 114005, 2020.

[10] **M. D. Christie**, S. Sun, L. Deng, D. H. Ning, H. Du, S. W. Zhang, and W. H. Li, "A variable resonance magnetorheological-fluid-based pendulum tuned mass damper for seismic vibration suppression," *Mechanical Systems and Signal Processing,* Article vol. 116, pp. 530-544, 2019.

[11] L. Deng, S. Sun, **M. D. Christie**, J. Yang, D. Ning, X. Zhu, H. Du, S. Zhang, and W. Li, "Experimental testing and modelling of a rotary variable stiffness and damping shock absorber using magnetorheological technology," *Journal of Intelligent Material Systems and Structures,* vol. 30, no. 10, pp. 1453-1465, 2019.

[12] J. Yang, S. S. Sun, D. Ning, Z. Li, L. Deng, **M. D. Christie**, H. Du, S. W. Zhang, and W. H. Li, "Development and evaluation of a highly adaptive MRF-based absorber with a large effective frequency range," *Smart Materials and Structures,* Article vol. 28, no. 10, 2019, Art. no. 105003.

Conference proceedings

[13] **M. D. Christie**, S. Sun, and W. Li, "Building Vibration Suppression Through a Magnetorheological Variable Resonance Pendulum Tuned Mass Damper," in *Vibration Engineering for a Sustainable Future*, Cham, 2021, pp. 281-287: Springer International Publishing.

REFERENCES

[1] M. H. Dickinson, C. T. Farley, R. J. Full, M. A. R. Koehl, R. Kram, and S. Lehman, "How animals move: An integrative view," *Science,* Review vol. 288, no. 5463, pp. 100-106, 2000.

[2] M. H. Raibert, *Legged robots that balance*. Massachusetts Institute of Technology, 1986, p. 233.

[3] M. Buehler, R. Battaglia, A. Cocosco, G. Hawker, J. Sarkis, and K. Yamazaki, "SCOUT: a simple quadruped that walks, climbs, and runs," in *Proceedings - IEEE International Conference on Robotics and Automation*, 1998, vol. 2, pp. 1707-1712.

[4] U. Saranli, M. Buehler, and D. E. Koditschek, "RHex: A simple and highly mobile hexapod robot," *International Journal of Robotics Research,* Article vol. 20, no. 7, pp. 616-631, 2001.

[5] R. D. Quinn, J. T. Offi, D. A. Kingsley, and R. E. Ritzmann, "Improved mobility through abstracted biological principles," in *IEEE International Conference on Intelligent Robots and Systems*, 2002, vol. 3, pp. 2652-2657.

[6] Y. Fukuoka, "Dynamic locomotion of a biomorphic quadruped 'Tekken' robot using various gaits: walk, trot, free-gait and bound," *Applied bionics and biomechanics,* vol. 6, no. 1, pp. 63-71, 2009.

[7] E. Z. Moore, D. Campbell, F. Grimminger, and M. Buehler, "Reliable stair climbing in the simple hexapod 'RHex'," in *Proceedings - IEEE International Conference on Robotics and Automation*, 2002, vol. 3, pp. 2222-2227.

[8] X. Liang, M. Xu, L. Xu, P. Liu, X. Ren, Z. Kong, J. Yang, and S. Zhang, "The AmphiHex: A novel amphibious robot with transformable leg-flipper composite propulsion mechanism," in *IEEE International Conference on Intelligent Robots and Systems*, 2012, pp. 3667-3672.

[9] B. D. Clark, *Mechanics and Control on the Hind Limb of Bobwhite Quail Running and Landing on Substrates of Unpredictable Mechanical Stiffness*. PhD Thesis, University of Chicago, Department of Anatomy, 1988.

[10] D. P. Ferris, M. Louie, and C. T. Farley, "Running in the real world: Adjusting leg stiffness for different surfaces," *Proceedings of the Royal Society B: Biological Sciences,* Article vol. 265, no. 1400, pp. 989-994, 1998.

[11] C. T. Farley, H. H. P. Houdijk, C. Van Strien, and M. Louie, "Mechanism of leg stiffness adjustment for hopping on surfaces of different stiffnesses," *Journal of Applied Physiology,* Article vol. 85, no. 3, pp. 1044-1055, 1998.

[12] R. Blickhan, "The spring-mass model for running and hopping," *Journal of biomechanics,* vol. 22, no. 11-12, pp. 1217-1227, 1989.

[13] N. C. Heglund, C. R. Taylor, and T. A. McMahon, "Scaling stride frequency and gait to animal size: mice to horses," *Science,* Article vol. 186, no. 4169, pp. 1112-1113, 1974.

[14] R. M. Alexander, "Three uses for springs in legged locomotion," *International Journal of Robotics Research,* Article vol. 9, no. 2, pp. 53-61, 1990.

[15] C. T. Moritz and C. T. Farley, "Passive dynamics change leg mechanics for an unexpected surface during human hopping," *Journal of Applied Physiology,* vol. 97, no. 4, pp. 1313-1322, 2004.

[16] R. Müller, A. V. Birn-Jeffery, and Y. Blum, "Human and avian running on uneven ground: a model-based comparison," *Journal of The Royal Society Interface,* vol. 13, no. 122, p. 20160529, 2016.

[17] M. A. Daley, "Understanding the Agility of Running Birds: Sensorimotor and Mechanical Factors in Avian Bipedal Locomotion," *Integrative and Comparative Biology,* vol. 58, no. 5, pp. 884-893, 2018.

[18] R. Ham, T. Sugar, B. Vanderborght, K. Hollander, and D. Lefeber, "Compliant actuator designs," *IEEE Robotics & Automation Magazine,* vol. 16, no. 3, pp. 81-94, 2009.

[19] B. Vanderborght, A. Albu-Schaeffer, A. Bicchi, E. Burdet, D. G. Caldwell, R. Carloni, M. Catalano, O. Eiberger, W. Friedl, G. Ganesh, M. Garabini, M. Grebenstein, G. Grioli, S. Haddadin, H. Hoppner, A. Jafari, M. Laffranchi, D. Lefeber, F. Petit, S. Stramigioli, N. Tsagarakis, M. Van Damme, R. Van Ham, L. C. Visser, and S. Wolf, "Variable impedance actuators: A review," *Robotics and Autonomous Systems,* vol. 61, no. 12, pp. 1601-1614, 2013.

[20] B. Vanderborght, R. Van Ham, D. Lefeber, T. G. Sugar, and K. W. Hollander, "Comparison of Mechanical Design and Energy Consumption of Adaptable, Passive-compliant Actuators," *The International Journal of Robotics Research,* vol. 28, no. 1, pp. 90-103, 2009.

[21] K. C. Galloway, J. E. Clark, and D. E. Koditschek, "Variable Stiffness Legs for Robust, Efficient, and Stable Dynamic Running," *Journal of Mechanisms and Robotics,* vol. 5, no. 1, p. 011009, 2013.

[22] H. Q. Vu, H. Hauser, D. Leach, and R. Pfeifer, "A variable stiffness mechanism for improving energy efficiency of a planar single-legged hopping robot," in *2013 16th International Conference on Advanced Robotics*, 2013, pp. 1-7.

[23] J. W. Hurst, J. E. Chestnutt, and A. A. Rizzi, "An actuator with physically variable stiffness for highly dynamic legged locomotion," in *Proceedings - IEEE International Conference on Robotics and Automation*, 2004, vol. 2004, pp. 4662-4667.

[24] X. Tang, H. Du, S. Sun, D. Ning, Z. Xing, and W. Li, "Takagi–Sugeno Fuzzy Control for Semi-Active Vehicle Suspension With a Magnetorheological Damper and Experimental Validation," *IEEE/ASME Transactions on Mechatronics,* vol. 22, no. 1, pp. 291-300, 2017.

[25] F. Weber and M. Maślanka, "Frequency and damping adaptation of a TMD with controlled MR damper," *Smart Materials and Structures,* vol. 21, no. 5, p. 055011, 2012.

[26] S. J. Dyke, B. F. Spencer Jr, M. K. Sain, and J. D. Carlson, "Modeling and control of magnetorheological dampers for seismic response reduction," *Smart Materials and Structures,* Article vol. 5, no. 5, pp. 565-575, 1996.

[27] B. F. Spencer Jr, S. J. Dyke, M. K. Sain, and J. D. Carlson, "Phenomenological model for magnetorheological dampers," *Journal of Engineering Mechanics,* Article vol. 123, no. 3, pp. 230-238, 1997.

[28] N. Jiang, S. Sun, Y. Ouyang, M. Xu, W. Li, and S. Zhang, "A highly adaptive magnetorheological fluid robotic leg for efficient terrestrial locomotion," *Smart Materials and Structures,* Article vol. 25, no. 9, 2016, Art. no. 095019.

[29] S. Sun, J. Yang, W. Li, H. Deng, H. Du, and G. Alici, "Development of a novel variable stiffness and damping magnetorheological fluid damper," *Smart Materials and Structures,* vol. 24, no. 8, p. 085021, 2015.

[30] C. Greiner-Petter, "A semi-active magnetorheological fluid mechanism with variable stiffness and damping," *Smart materials and structures,* vol. 23, no. 11, p. 115008, 2014.

[31] S. Sun, H. Deng, and W. Li, "Variable stiffness and damping suspension system for train," in *Proceedings of SPIE - The International Society for Optical Engineering*, 2014, vol. 9057.

[32] S. Sun, H. Deng, H. Du, W. Li, J. Yang, G. Liu, G. Alici, and T. Yan, "A Compact Variable Stiffness and Damping Shock Absorber for Vehicle Suspension," *IEEE/ASME Transactions on Mechatronics,* Article vol. 20, no. 5, pp. 2621-2629, 2015, Art. no. 7086317.

[33] J. Seipel and P. Holmes, "A simple model for clock-actuated legged locomotion," *Regular and Chaotic Dynamics,* vol. 12, no. 5, pp. 502-520, 2007.

[34] N. C. Heglund and C. R. Taylor, "Speed, stride frequency and energy cost per stride: how do they change with body size and gait?," *Journal of Experimental Biology,* Article vol. 138, pp. 301-318, 1988.

[35] D. F. Hoyt and C. R. Taylor, "Gait and the energetics of locomotion in horses," *Nature,* Article vol. 292, no. 5820, pp. 239-240, 1981.

[36] R. Kram and C. R. Taylor, "Energetics of running: A new perspective," *Nature,* Article vol. 346, no. 6281, pp. 265-267, 1990.

[37] C. T. Farley and O. González, "Leg stiffness and stride frequency in human running," *J Biomech,* vol. 29, no. 2, pp. 181-6, 1996.

[38] D. P. Ferris, K. Liang, and C. T. Farley, "Runners adjust leg stiffness for their first step on a new running surface," *Journal of Biomechanics,* Article vol. 32, no. 8, pp. 787-794, 1999.

[39] M. Raibert, "BigDog, the rough-terrain quadruped robot," in *IFAC Proceedings Volumes (IFAC-PapersOnline)*, 2008, vol. 17.

[40] Boston Dynamics. (2021). *Spot*. Available: https://www.bostondynamics.com/spot/resources

[41] Y. Sakagami, R. Watanabe, C. Aoyama, S. Matsunaga, N. Higaki, and K. Fujimura, "The intelligent ASIMO: System overview and integration," in *IEEE International Conference on Intelligent Robots and Systems*, 2002, vol. 3, pp. 2478-2483.

[42] G.-H. Liu, H.-Y. Lin, H.-Y. Lin, S.-T. Chen, and P.-C. Lin, "A Bio-Inspired Hopping Kangaroo Robot with an Active Tail," *Journal of Bionic Engineering,* vol. 11, no. 4, pp. 541-555, 2014.

[43] B. G. A. Lambrecht, A. D. Horchler, and R. D. Quinn, "A small, insect-inspired robot that runs and jumps," in *Proceedings - IEEE International Conference on Robotics and Automation*, 2005, vol. 2005, pp. 1240-1245.

[44] J. E. Clark, J. G. Cham, S. A. Bailey, E. M. Froehlich, P. K. Nahata, R. J. Full, and M. R. Cutkosky, "Biomimetic design and fabrication of a hexapedal running robot," *Proceedings - IEEE International Conference on Robotics and Automation,* Article vol. 4, pp. 3643-3649, 2001.

[45] Boston Dynamics. (2019). *Spot: User Guide (Release 2.0, Version A ed.)*. Available: https://www.bostondynamics.com/sites/default/files/inline-files/spot-user-guide-r2.0-va.pdf

[46] R. Altendorfer, N. Moore, H. Komsuoglu, M. Buehler, H. B. Brown, D. McMordie, U. Saranli, R. Full, and D. E. Koditschek, "RHex: A Biologically Inspired Hexapod Runner," *Autonomous Robots,* vol. 11, no. 3, pp. 207-213, 2001.

[47] C. Li, P. B. Umbanhowar, H. Komsuoglu, D. E. Koditschek, and D. I. Goldman, "Sensitive dependence of the motion of a legged robot on granular media," *Proceedings of the National Academy of Sciences of the United States of America,* Article vol. 106, no. 9, pp. 3029-3034, 2009.

[48] H. Vu, R. Pfeifer, F. Iida, and X. Yu, "Improving energy efficiency of hopping locomotion by using a variable stiffness actuator," *IEEE/ASME Transactions on Mechatronics,* pp. 472-486, 2015.

[49] K. C. Galloway, J. E. Clark, M. Yim, and D. E. Koditschek, "Experimental investigations into the role of passive variable compliant legs for dynamic robotic locomotion," in *Proceedings - IEEE International Conference on Robotics and Automation*, 2011, pp. 1243-1249.

[50] X. Zhou and S. Bi, "A survey of bio-inspired compliant legged robot designs," *Bioinspiration and Biomimetics,* Article vol. 7, no. 4, 2012, Art. no. 041001.

[51] Z. Jing, S. Sun, Y. Ouyang, S. Zhang, W. Li, and J. Zheng, "Design and modeling analysis of a changeable stiffness robotic leg working with magnetorheological technology," *Journal of Intelligent Material Systems and Structures,* vol. 29, no. 19, pp. 3725-3736, 2018.

[52] R. Blickhan and R. J. Full, "Similarity in multilegged locomotion: Bouncing like a monopode," *Journal of Comparative Physiology A,* Review vol. 173, no. 5, pp. 509-517, 1993.

[53] C. K. Huang and P. C. Lin, "Asymmetric stability property of a sagittal-plane model with a compliant leg and Rolling contact," in *Proceedings of the 17th International Conference on Advanced Robotics*, 2015, pp. 111-116.

[54] G. Piovan and K. Byl, "Two-element control for the active SLIP model," in *Proceedings - IEEE International Conference on Robotics and Automation*, 2013, pp. 5656-5662.

[55] K. J. Huang, C. K. Huang, and P. C. Lin, "A simple running model with rolling contact and its role as a template for dynamic locomotion on a hexapod robot," *Bioinspir Biomim,* vol. 9, no. 4, p. 046004, 2014.

[56] C. J. Hu, C. K. Huang, and P. C. Lin, "A torque-actuated dissipative spring loaded inverted pendulum model with rolling contact and its use as the template for design and dynamic behavior generation on a hexapod robot," in *Proceedings - IEEE International Conference on Robotics and Automation*, 2015, pp. 5177-5183.

[57] R. J. Full and D. E. Koditschek, "Templates and anchors: Neuromechanical hypotheses of legged locomotion on land," *Journal of Experimental Biology,* Article vol. 202, no. 23, pp. 3325-3332, 1999.

[58] F. Peuker, A. Seyfarth, and S. Grimmer, "Inheritance of SLIP running stability to a single-legged and bipedal model with leg mass and damping," in *Proceedings of the IEEE RAS and EMBS International Conference on Biomedical Robotics and Biomechatronics*, 2012, pp. 395-400.

[59] J. Rummel and A. Seyfarth, "Stable running with segmented legs," *International Journal of Robotics Research,* Article vol. 27, no. 8, pp. 919-934, 2008.

[60] G. A. Pratt and M. M. Williamson, "Series elastic actuators," in *IEEE International Conference on Intelligent Robots and Systems*, 1995, vol. 1, pp. 399-406.

[61] S. Wolf, G. Grioli, O. Eiberger, W. Friedl, M. Grebenstein, H. Hoppner, E. Burdet, D. G. Caldwell, R. Carloni, M. G. Catalano, D. Lefeber, S. Stramigioli, N. Tsagarakis, M. Van Damme, R. Van Ham, B. Vanderborght, L. C. Visser, A. Bicchi, and A. Albu-Schaffer, "Variable Stiffness Actuators: Review on Design and Components," *IEEE/ASME Transactions on Mechatronics,* vol. 21, no. 5, pp. 2418-2430, 2016.

[62] M. D. Christie, S. S. Sun, D. H. Ning, H. Du, S. W. Zhang, and W. H. Li, "A torsional MRE joint for a C-shaped robotic leg," *Smart Materials and Structures,* Article vol. 26, no. 1, 2017, Art. no. 015002.

[63] A. Mutka, E. Koco, and Z. Kovacic, "Adaptive Control of Quadruped Locomotion Through Variable Compliance of Revolute Spiral Feet," *International Journal of Advanced Robotic Systems,* p. 1, 2014.

[64] J. de Vicente, D. J. Klingenberg, and R. Hidalgo-Alvarez, "Magnetorheological fluids: a review," *Soft Matter,* vol. 7, no. 8, pp. 3701-3710, 2011.

[65] J. Rabinow, "The Magnetic Fluid Clutch," *Transactions of the American Institute of Electrical Engineers,* Article vol. 67, pp. 1308-1315, 1948.

[66] W. H. Li, H. Du, G. Chen, S. H. Yeo, and N. Guo, "Nonlinear viscoelastic properties of MR fluids under large-amplitude-oscillatory-shear," *Rheologica Acta,* Article vol. 42, no. 3, pp. 280-286, 2003.

[67] W. H. Li, Y. Zhou, and T. F. Tian, "Viscoelastic properties of MR elastomers under harmonic loading," *Rheologica Acta,* Article vol. 49, no. 7, pp. 733-740, 2010.

[68] M. R. Jolly, J. D. Carlson, and B. C. Muñoz, "A model of the behaviour of magnetorheological materials," *Smart Materials and Structures,* Article vol. 5, no. 5, pp. 607-614, 1996.

[69] T. F. Tian, W. H. Li, and G. Alici, "Study of magnetorheology and sensing capabilities of MR elastomers," *Journal of Physics: Conference Series,* vol. 412, p. 012037, 2013.

[70] W. H. Li, X. Z. Zhang, and H. Du, "Magnetorheological Elastomers and Their Applications," in *Advances in Elastomers I: Blends and Interpenetrating Networks*, M. P. Visakh, S. Thomas, K. A. Chandra, and P. A. Mathew, Eds. Berlin, Heidelberg: Springer Berlin Heidelberg, 2013, pp. 357-374.

[71] L. C. Davis, "Model of magnetorheological elastomers," *Journal of applied physics,* vol. 85, no. 6, pp. 3348-3351, 1999.

[72] M. R. Jolly, J. W. Bender, and J. D. Carlson, "Properties and applications of commercial magnetorheological fluids," *Journal of Intelligent Material Systems and Structures,* Article vol. 10, no. 1, pp. 5-13, 1999.

[73] R. Stanway, "Smart fluids: Current and future developments," *Materials Science and Technology,* Review vol. 20, no. 8, pp. 931-939, 2004.

[74] Y. Li, J. Li, W. Li, and H. Du, "A state-of-the-art review on magnetorheological elastomer devices," *Smart Materials and Structures,* Review vol. 23, no. 12, 2014, Art. no. 123001.

[75] J. M. Ginder, M. E. Nichols, L. D. Elie, and J. L. Tardiff, "Magnetorheological elastomers: Properties and applications," *Proceedings of SPIE - The International Society for Optical Engineering,* Article vol. 3675, pp. 131-138, 1999.

[76] F. Imaduddin, S. A. Mazlan, and H. Zamzuri, "A design and modelling review of rotary magnetorheological damper," *Materials & Design,* vol. 51, pp. 575-591, 2013.

[77] D. W. Felt, M. Hagenbuchle, J. Liu, and J. Richard, "Rheology of a Magnetorheological Fluid," *Journal of Intelligent Material Systems and Structures,* vol. 7, no. 5, pp. 589-593, 1996.

[78] N. M. Wereley, J. U. Cho, Y. T. Choi, and S. B. Choi, "Magnetorheological dampers in shear mode," *Smart Materials and Structures,* vol. 17, no. 1, p. 015022, 2007.

[79] I. Bica, Y. D. Liu, and H. J. Choi, "Physical characteristics of magnetorheological suspensions and their applications," *Journal of Industrial and Engineering Chemistry,* vol. 19, no. 2, pp. 394-406, 2013.

[80] M. D. Christie, S. Sun, L. Deng, D. H. Ning, H. Du, S. W. Zhang, and W. H. Li, "A variable resonance magnetorheological-fluid-based pendulum tuned mass damper for seismic vibration suppression," *Mechanical Systems and Signal Processing,* Article vol. 116, pp. 530-544, 2019.

[81] L. Deng, S. Sun, M. D. Christie, J. Yang, D. Ning, X. Zhu, H. Du, S. Zhang, and W. Li, "Experimental testing and modelling of a rotary variable stiffness and damping shock absorber using magnetorheological technology," *Journal of Intelligent Material Systems and Structures,* vol. 30, no. 10, pp. 1453-1465, 2019.

[82] X. Dong, W. Liu, G. An, Y. Zhou, J. Yu, and Q. Lin, "A novel rotary magnetorheological flexible joint with variable stiffness and damping," *Smart Materials and Structures,* vol. 27, no. 10, p. 105045, 2018.

[83] S. Sun, J. Yang, P. Wang, M. Nakano, L. Shen, S. Zhang, and W. Li, "Experimental Study of a Variable Stiffness Seat Suspension Installed With a Compact Rotary MR Damper," *Frontiers in Materials,* vol. 8, no. 38, 2021.

[84] E. Kostamo, M. Focchi, E. Guglielmino, J. Kostamo, C. Semini, J. Buchli, M. Pietola, and D. Caldwell, "Magnetorheologically Damped Compliant Foot for Legged Robotic Application," *Journal of Mechanical Design,* vol. 136, no. 2, 2013.

[85] Z. Li, Y. Gong, S. Li, and W. Wang, "Magnetic Hysteresis Compensation Control of a Magnetorheological Damper," *Frontiers in Materials,* vol. 6, no. 299, 2019.

[86] J. Yang, S. S. Sun, H. Du, W. H. Li, G. Alici, and H. X. Deng, "A novel magnetorheological elastomer isolator with negative changing stiffness for vibration reduction," *Smart Materials and Structures,* Article vol. 23, no. 10, 2014, Art. no. 105023.

[87] X. Zhu, X. Jing, and L. Cheng, "Magnetorheological fluid dampers: A review on structure design and analysis," *Journal of Intelligent Material Systems and Structures,* Review vol. 23, no. 8, pp. 839-873, 2012.

[88] Q. Sun, J. X. Zhou, and L. Zhang, "An adaptive beam model and dynamic characteristics of magnetorheological materials," *Journal of Sound and Vibration,* Article vol. 261, no. 3, pp. 465-481, 2003.

[89] M. Eshaghi, R. Sedaghati, and S. Rakheja, "The effect of magneto-rheological fluid on vibration suppression capability of adaptive sandwich plates: Experimental and finite element analysis," *Journal of Intelligent Material Systems and Structures,* vol. 26, no. 14, pp. 1920-1935, 2015.

[90] LORD Co. (2008). *LORD TECHNICAL DATA: MRF-140CG Magneto-Rheological Fluid*. Available: https://lordfulfillment.com/pdf/44/DS7012_MRF-140CGMRFluid.pdf

[91] J. Y. Jun and J. E. Clark, "Dynamic stability of variable stiffness running," in *2009 IEEE International Conference on Robotics and Automation*, 2009, pp. 1756-1761.

[92] N. Baron, A. Philippides, and N. Rojas, "A Dynamically Balanced Kinematically Redundant Planar Parallel Robot," *Journal of Mechanical Design,* vol. 143, no. 8, 2021.

[93] R. S. Berkof and G. G. Lowen, "Theory of Shaking Moment Optimization of Force-Balanced Four-Bar Linkages," *Journal of Engineering for Industry,* vol. 93, no. 1, pp. 53-60, 1971.

[94] R. S. Berkof and G. G. Lowen, "A New Method for Completely Force Balancing Simple Linkages," *Journal of Engineering for Industry,* vol. 91, no. 1, pp. 21-26, 1969.

[95] J. J. de Jong, J. van Dijk, and J. L. Herder, "A screw based methodology for instantaneous dynamic balance," *Mechanism and Machine Theory,* vol. 141, pp. 267-282, 2019.

[96] R. Altendorfer, U. Saranli, H. Komsuoglu, D. Koditschek, H. B. Brown, M. Buehler, N. Moore, D. McMordie, and R. Full, "Evidence for Spring Loaded Inverted Pendulum Running in a Hexapod Robot," in *Experimental Robotics VII*, Berlin, Heidelberg, 2001, pp. 291-302: Springer Berlin Heidelberg.

[97] J. Y. Jun and J. E. Clark, "Effect of rolling on running performance," in *Proceedings - IEEE International Conference on Robotics and Automation*, 2011, pp. 2009-2014.

[98] M. M. AnkaralI and U. SaranlI, "Control of underactuated planar pronking through an embedded spring-mass Hopper template," *Autonomous Robots,* Article vol. 30, no. 2, pp. 217-231, 2011.

[99] H. Geyer, A. Seyfarth, and R. Blickhan, "Spring-mass running: simple approximate solution and application to gait stability," *J Theor Biol,* vol. 232, no. 3, pp. 315-28, 2005.

[100] A. Seyfarth, H. Geyer, M. Günther, and R. Blickhan, "A movement criterion for running," *J Biomech,* vol. 35, no. 5, pp. 649-55, 2002.

[101] F. Rumiche, J. E. Indacochea, and M. L. Wang, "Assessment of the Effect of Microstructure on the Magnetic Behavior of Structural Carbon Steels Using an Electromagnetic Sensor," *Journal of Materials Engineering and Performance,* vol. 17, no. 4, pp. 586-593, 2008.

[102] S. Grimmer, M. Ernst, M. Günther, and R. Blickhan, "Running on uneven ground: leg adjustment to vertical steps and self-stability," *Journal of Experimental Biology,* vol. 211, no. 18, p. 2989, 2008.

[103] A. S. Voloshina, A. D. Kuo, M. A. Daley, and D. P. Ferris, "Biomechanics and energetics of walking on uneven terrain," *The Journal of Experimental Biology,* vol. 216, no. 21, p. 3963, 2013.

[104] K.-J. Huang, S.-C. Chen, H. Komsuoglu, G. Lopes, J. Clark, and P.-C. Lin, "Design and Performance Evaluation of a Bio-Inspired and Single-Motor-Driven Hexapod Robot With Dynamical Gaits," *Journal of Mechanisms and Robotics,* vol. 7, no. 3, p. 031017, 2015.

[105] P. Devita and W. A. Skelly, "Effect of landing stiffness on joint kinetics and energetics in the lower extremity," *Med Sci Sports Exerc,* vol. 24, no. 1, pp. 108-15, 1992.

[106] M. Roy, S. Tobias, and B. Reinhard, "Muscle Preactivation Control: Simulation of Ankle Joint Adjustments at Touchdown During Running on Uneven Ground," *Journal of Applied Biomechanics,* vol. 28, no. 6, pp. 718-725, 2012.

[107] P. Dyhre-Poulsen, E. B. Simonsen, and M. Voigt, "Dynamic control of muscle stiffness and H reflex modulation during hopping and jumping in man," *J Physiol,* vol. 437, pp. 287-304, 1991.

[108] R. Müller, M. Ernst, and R. Blickhan, "Leg adjustments during running across visible and camouflaged incidental changes in ground level," *The Journal of Experimental Biology,* vol. 215, no. 17, p. 3072, 2012.

[109] R. Müller and R. Blickhan, "Running on uneven ground: Leg adjustments to altered ground level," *Human Movement Science,* vol. 29, no. 4, pp. 578-589, 2010.

[110] T. R. Clites, A. S. Arnold, N. M. Singh, E. Kline, H. Chen, C. Tugman, B. Billadeau, A. A. Biewener, and H. M. Herr, "Goats decrease hindlimb stiffness when walking over compliant surfaces," *The Journal of Experimental Biology,* vol. 222, no. 10, p. jeb198325, 2019.

[111] C. T. Moritz, S. M. Greene, and C. T. Farley, "Neuromuscular changes for hopping on a range of damped surfaces," *J Appl Physiol (1985),* vol. 96, no. 5, pp. 1996-2004, 2004.

[112] L. M.-G. Jill, "Kinematics and Impulse Characteristics of Drop Landings from Three Heights," *International Journal of Sport Biomechanics,* vol. 7, no. 2, pp. 201-224, 1991.

[113] H. N. Ozgüven and N. Berme, "An experimental and analytical study of impact forces during human jumping," *J Biomech,* vol. 21, no. 12, pp. 1061-6, 1988.

[114] J. Mizrahi and Z. Susak, "Analysis of parameters affecting impact force attenuation during landing in human vertical free fall," *Eng Med,* vol. 11, no. 3, pp. 141-7, 1982.

[115] J. M. Hackney, R. L. Clay, and M. James, "Force-displacement differences in the lower extremities of young healthy adults between drop jumps and drop landings," *Hum Mov Sci,* vol. 49, pp. 79-86, 2016.

[116] M. J. Decker, M. R. Torry, D. J. Wyland, W. I. Sterett, and J. Richard Steadman, "Gender differences in lower extremity kinematics, kinetics and energy absorption during landing," *Clin Biomech (Bristol, Avon),* vol. 18, no. 7, pp. 662-9, 2003.

[117] S. N. Zhang, B. T. Bates, and J. S. Dufek, "Contributions of lower extremity joints to energy dissipation during landings," *Med Sci Sports Exerc,* vol. 32, no. 4, pp. 812-9, 2000.

[118] J. T. Podraza and S. C. White, "Effect of knee flexion angle on ground reaction forces, knee moments and muscle co-contraction during an impact-like deceleration landing: Implications for the non-contact mechanism of ACL injury," *The Knee,* vol. 17, no. 4, pp. 291-295, 2010.

[119] J. W. Whitting, J. R. Steele, D. E. McGhee, and B. J. Munro, "Effects of passive ankle dorsiflexion stiffness on ankle mechanics during drop landings," *J Sci Med Sport,* vol. 15, no. 5, pp. 468-73, 2012.

[120] D. C. Batterbee, N. D. Sims, R. Stanway, and Z. Wolejsza, "Magnetorheological landing gear: 1. A design methodology," *Smart Materials and Structures,* vol. 16, no. 6, pp. 2429-2440, 2007.

[121] Y.-T. Choi and N. M. Wereley, "Shock Isolation Systems Using Magnetorheological Dampers," *Journal of Vibration and Acoustics,* vol. 130, no. 2, 2008.

[122] Y.-T. Choi and N. M. Wereley, "Biodynamic Response Mitigation to Shock Loads Using Magnetorheological Helicopter Crew Seat Suspensions," *Journal of Aircraft,* vol. 42, no. 5, pp. 1288-1295, 2005.

[123] Y. T. Choi and N. M. Wereley, "Mitigation of biodynamic response to vibratory and blast-induced shock loads using magnetorheological seat suspensions," *Proceedings of the Institution of Mechanical Engineers, Part D: Journal of Automobile Engineering,* vol. 219, no. 6, pp. 741-753, 2005.

[124] Y.-T. Choi and N. M. Wereley, "Vibration Control of a Landing Gear System Featuring Electrorheological/Magnetorheological Fluids," *Journal of Aircraft,* vol. 40, no. 3, pp. 432-439, 2003.

[125] D. W. Robinson, J. E. Pratt, D. J. Paluska, and G. A. Pratt, "Series elastic actuator development for a biomimetic walking robot," in Proceedings - *IEEE/ASME International Conference on Advanced Intelligent Mechatronics*, 1999, pp. 561-568.